EUROPEAN COMMISSION

nuclear science and technology

Heater Experiment: Rock and bentonite Thermo-Hydro-Mechanical (THM) processes in the near-field of a thermal source for development of deep underground high level radioactive waste repositories

(HE)

Authors
Ingeborg Göbel, BGR (DE), Hans-Joachim Alheid, BGR (DE), Norbert Jockwer, GRS (DE), Juan Carlos Mayor, ENRESA (ES), José Luis García-Siñeriz, AITEMIN (ES), Eduardo Alonso, CIMNE (ES), Hanspeter Weber, NAGRA (CH), Michael Ploetze, ETH (CH), Georg Klubertanz, COLENCO (CH), Christian Ammon Rothpletz, Lienhard + Cie AG (CH)

Contract No: FIKW-CT-2001-00132

Final report

Work performed as part of the European Atomic Energy Community's R&T specific programme
Nuclear Energy 1998-2002, key action Nuclear Fission Safety (Fifth Framework Programme)
Area: Safety of the Fuel Cycle

Directorate-General for Research
Euratom

2006

EUR 22586

Project coordinator

Bundesanstalt für Geowissenschaften und Rohstoffe (BGR), DE

Project partners

1. Gesellschaft für Anlagen- und Reaktorsicherheit mbH (GRS), DE
2. Empresa Nacional de Residuos Radiactivos SA (ENRESA), ES
3. Asociación para la Investigación y Desarrollo Industrial de los Recursos Naturales (AITEMIN), ES
4. Centre International de Métodos Numérics en Ingenyería (CIMNE), ES
5. Nationale Genossenschaft für die Lagerung radioaktiver Abfälle (NAGRA), CH
6. Eidgenössische Technische Hochschule Zürich, Institut für Geotechnik (ETHZ), CH
7. Colenco Power Engineering Ltd (COLENCO), CH
8. Rothpletz Lienhard + Cie AG (RL), CH

ACKNOWLEDGEMENTS

The partners are thankful for the financial support of the European Commission, the Swiss State Secretariat for Education and Research (SER), and the German Federal Ministry of Economics and Technology (BMWi). The co-funding by the European Commission was done as part of the fifth EURATOM framework programme for Research and Training, key action Nuclear Fission (1998 – 2002). We appreciate the support of Christophe Davies of the European Commission and his dedication to the project throughout all its phases.

The persons listed below contributed to the preparation of this report:

Paul Bossart	GI
Christoph Bühler	Solexperts AG
Katja Emmerich	BGR, now ITC-WGT, Karlsruhe
Ana Maria Fernandez	CIEMAT
A Graf	GI
Stephan Kaufhold	BGR
Michael Kech	Solexperts AG
A. Lloret	CIMNE
T Meyer	GRS
Rüdiger Miehe	GRS
Juan Jorge Muñoz	CIMNE
Marcel Naumann	BGR
Christoph Nussbaum	GI
Thomas Pletsch	BGR
Ingo Plischke	BGR
Maria Rey	AITEMIN
Hajo Schnier	BGR
Kristof Schuster	BGR
Karlheinz Sprado	BGR
Thomas Trick	Solexperts AG
Klaus Wieczorek	GRS
A Zingg	GI

Executive Summary

The long-term safety of geological repositories for radioactive waste depends on a multibarrier system consisting of a combination of engineered and geological barriers. Interactions between these different barriers are important issues for waste disposal. In this project, investigations were carried out with the aim of understanding processes occurring during the transient phase of the repository lifetime when the buffer and the host rock start to resaturate, influenced by pore pressure, temperature gradients, and suction. The focus of the work was on the interaction between a clay formation (Opalinus Clay) and a clay-based buffer material (highly compacted bentonite). The objective of the experiment is to improve the understanding of the coupled thermo-hydro-mechanical (THM) processes in a host rock-buffer system, based on experimental observations and numerical modelling. In detail, the basic objectives are:

- Long-term monitoring in the vicinity of the heat source during hydration and heating phases, particularly observation and study of coupled THM processes in the near-field, i.e. continuous measurement of temperatures, pore pressures, displacements, electrical conductivity, and analysis of gas and water released into the rock due to the effects of heating.

- Determination of the properties of the barrier and host rock using results from laboratory and in situ experiments, i.e. general mechanical and mineralogical properties, in-situ stress state, and changes induced by the experiment.

- Study of the interaction between the host rock and the bentonite buffer, as well as validation and refinement of existing tools for modeling THM processes.

- Study of the reliability of instrumentation and measuring techniques, e.g. inspection of sensors after dismantling the experimental set-up.

To achieve the defined objectives, the experiment was accompanied by an extensive programme of continuous monitoring, experimental investigations on-site and in laboratories and numerical modelling of coupled thermo-hydro-mechanical processes. Finally, the experiment was dismantled to provide laboratory samples of post-heating buffer and host rock material.

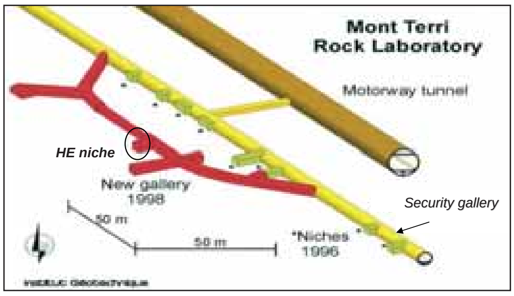

Figure 1: HE niche at the Mont Terri Rock Laboratory.

The HE experiment was performed at the Mont Terri Rock Laboratory in a niche excavated for this purpose in the shaly facies of the Opalinus Clay formation (Figure 1). The host rock is a highly consolidated stiff Jurassic clay-stone. A central vertical borehole (BHE-0) 300 mm in diameter and 7.5 m long was drilled in the niche floor. Heat-producing waste was simulated by a heater element with 10 cm diameter, held at a constant surface temperature of 100°C. The 2 m long heater element was placed in the vertical borehole at a depth of 4 to 6 m. It was embedded in a barrier of ring-shaped compacted bentonite blocks with an outer diameter of 30 cm and a dry density of 1.8 g/cm^3. A total of 19 boreholes were drilled in the niche floor for instrumentation purposes. Sensors for measuring the most relevant rock parameters, such as temperature, humidity, stress state, pore pressure, displacement, and electric resistivity, as well as devices for determining gas and water release, were installed in the boreholes. The experiment was designed to operate automatically with remote supervision via modem. To simulate long-term behaviour, and due to the absence of free water in the Mont Terri Rock Laboratory, an artificial hydration system was installed to accelerate the saturation process in the buffer prior to the heating phase. The water used was synthetic experimental water (Pearson's water A1 type), which is chemically similar to the water in the Opalinus Clay formation. The artificial saturation lasted for 35 months before the heating phase (duration 18 months) began. A time-table for the experiment is shown in Figure 2. Already during the hydration phase, several sensors (thermocouples, total pressure cells, pore pressure sensors) failed and had to be replaced.

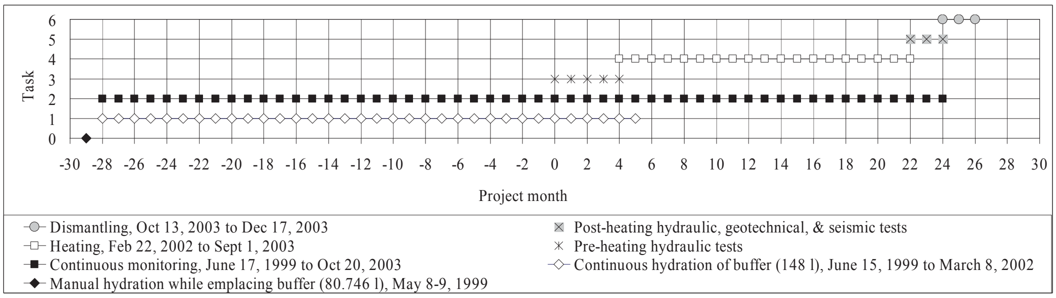

Figure 1.2: **Time-table for the HE experiment: negative numbers for project months indicate the installation period and positive num-bers the operational and post-operational phase when the project was co-financed by the EC.**

The first heating phase was carried out in different constant power steps (Figure 3), to allow adjustment of the parameters of the temperature control loop, reaching a maximum temperature in the bentonite blocks of about 68 ºC. The temperature control loop was then adjusted using the data obtained. The power applied to the heater was automatically regulated to a constant temperature of 100 ºC at the contact between the heater and the bentonite buffer. After the heater was switched off, the system cooled down rapidly. After about one month, the maximum temperature of 40 ºC allowed access for dismantling work. To identify potential changes in rock properties induced by the experiment, field investigations were performed during the cooling period, including hydraulic, geotechnical, and seismic tests. Additionally, rock samples were tested mechanically in the laboratory. The aims of dismantling were to

- determine the state of the bentonite after hydration and heating,
- analyse the performance of system components, e.g. sensors, engineered materials,
- visually inspect the performance of the system (cracks, sealing of buffer gaps, fractures, cables, etc).

The dismantling was done by excavating a vertical shaft, with sensors and samples being collected as planned after each meter of progress.

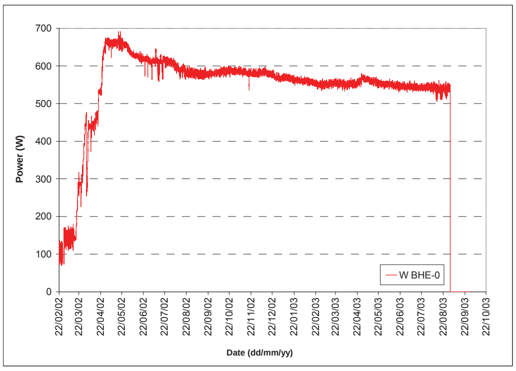

Figure 3: Evolution of power applied to the heater.

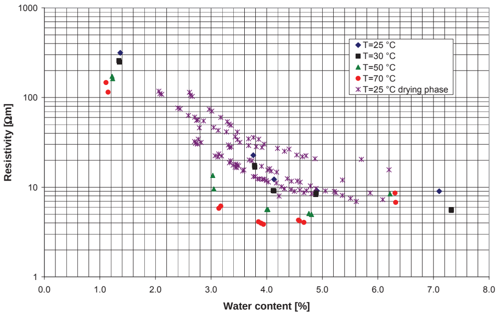

Figure 4: Results of resistivity measurements at different temperatures as a function of water content.

Monitoring results

The electric power needed to maintain a constant temperature of 100°C at the heater decreased with time, the most likely reason being a decrease in the thermal conductivity of the bentonite, probably caused by drying (Figure 3). Eight months after the start of heating, a constant temperature profile had developed at a distance of 1 to 2 m from the heater. In more peripheral regions, it took until the end of the heating phase to develop an approximately steady temperature state. The pore pressure sensors showed a pressure build-up at the beginning of heating, followed by a slow decrease and then a sharp pressure drop after heating stopped. The curves also differ in the size of their maxima, etc. Measurements of relative humidity (capacity sensors) showed no conclusive results and were probably perturbed by the heating. Radial displacement was measured using inclinometers; starting with the heating phase, the maximum values increased with time and began to drop slightly with cooling. With a maximum displacement of 5.5 mm, the measured values are more than one order of magnitude larger than the results of the computer simulations.

A geoelectric monitoring system was installed at Mont Terri in June 1999. It consisted of an automatic computer-controlled measurement and data acquisition unit with multiplexers for addressing the electrodes and an external injection voltage supply. Geoelectric measurements make use of the relationship between water content and electric resistivity of rocks and engineered barrier materials. Geoelectric tomography can be used to determine the resistivity distribution in larger areas of rock. The pore-water distribution can be derived if calibration measurements are available from laboratory tests. For the heater experiment, calibration measurements with samples of defined water content were performed for different temperatures. Repeated in-situ measurements were used to identify time-dependent changes in the water distribution.

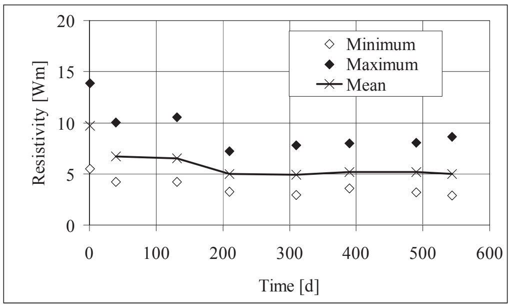

Figure 5: **Evolution of electric resistivity ρ between 4 m and 6 m depth in the plane between boreholes BHE-14 and BHE-17. Shown are the mean, maximum, and minimum values of resistivity.**

All resistivity curves show a decrease in resistivity with increasing water content (Figure 4). At higher temperatures the resistivities also decrease; this can be explained by the temperature dependence of the pore solution, because the conductivity of most electrolyte solutions increases with increasing temperature. The mean resistivity evolution in the heated area at about 0.7 m distant from the heater (Figure 5) shows a decrease during the first half-year of heating as a temperature effect (until a steady temperature field is reached). No resistivity increase attributable to desaturation was detected at any time. The only effect detected is a reduction in resistivity due to temperature increase. This result is confirmed by the post-dismantling investigations performed on samples from the test field.

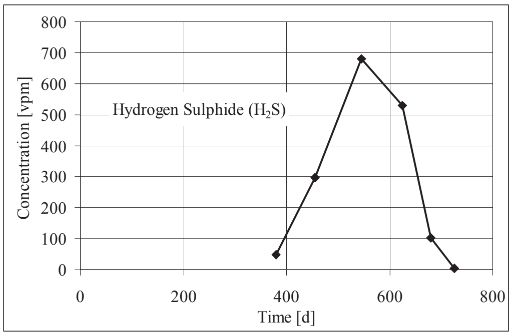

Figure 6: **Time-dependent evolution of hydrogen sulphide in the vicinity of the heater. Heating started at about day 200.**

Gas and water samples were collected via capillaries running through packers installed in vertical boreholes around the heater. A significant influence of heating was seen only in the borehole closest to the heater, e.g. hydrogen sulphide (H_2S) was generated (Figure 6), with concentrations up to 680 vpm at 0.35 m distance from the heater, while the other boreholes showed less than 12 vpm. H_2S in combination with water in the liquid or gaseous phase may lead to corrosion. The gas release from the host rock did not lead to a significant pressure increase in the residual volume of the boreholes. Furthermore, in the time period from February to September 2003 the concentration of carbon dioxide, helium, and hydro-carbons decreased slightly and the oxygen concentration increased. The laboratory investigations indicated that gas release from the Opalinus Clay is a very slow process and therefore sampling more often than three to four times a year reduces the gas concentration in the system.

Chemical analyses of the water showed a significant influence of either heating or proximity to the bentonite only in the borehole closest to the heater borehole (at 0.35 m distance). An increase in bicarbonate may indicate water movement from the bentonite to the Opalinus Clay.

Dismantling analysis - sensors

Signs of corrosion are evident in metallic parts, except those made of stainless steel, although it is generally superficial corrosion in staples, liner, heater tube, and some of the cables. Most of the sensors were quite resistant to corrosion (effects are slight and superficial), except for some piezometers (for pore pressure measurements) and total pressure cells (Figure 7). The common cause of failure of the total pressure cells was the penetration of water through the cable gland. This water damaged the electronics of the sensor, in some cases irreversibly. The piezometers failed because parts made of carbon steel were corroded; the zinc protection did not help. A defective Teflon protection on some of the cables made them less watertight and led to the failure of sensors in the hydrated zone. More or less all of the sensors in the hydrated zone, i.e. in the heater borehole and the bentonite buffer, became defective, while the same types of sensors in the more peripheral areas remained intact. The high salinity and the high acidity of the water, together with the increased temperature, seem to be detrimental to many metals. For future applications, high-alloy austenitic steel 316L or a similar steel is recommended.

Dismantling analysis – engineered barrier

The bentonite blocks were completely saturated at the time of dismantling. The volume increase amounted to 5 to 9% and was thus below the bentonite's potential. The 10 mm gap between the bentonite blocks and the Opalinus Clay filled with dry loose sand on the installation of the experiment was still intact.

Figure 7: Chemical corrosion in a total pressure cell (left) and detail of a piezometer installed in a borehole at 0.5 m distance from the heater (right).

Physico-chemical alterations due to heat and hydration are small. There are cementing processes, which slightly affect THM characteristics such as porosity and thermal properties. The HE bentonite itself shows negligible changes in mineralogical characteristics during the heater experiment. The capillary and interlayer water uptake with free swelling is slightly lower and slower in the heater region (Figure 8), which might be a consequence of the heating with associated cementing effects. The same samples also show higher bulk dry densities and lower outer surfaces (BET), which are parameters affecting the water absorption. A swelling pressure of the bentonite up to 2.8 MPa was reached within 6 days. The swelling pressure shows the normal behaviour for a calcium bentonite. The gravimetric water content shows a vertical and radial distribution (Figure 9) with up to 10 % lower values in the heater region, which is probably the result of drying due to heating. The dry density shows higher values in the heater region. Saturation of the bentonite was not achieved: the calculated saturation for all samples is slightly above 50 %.

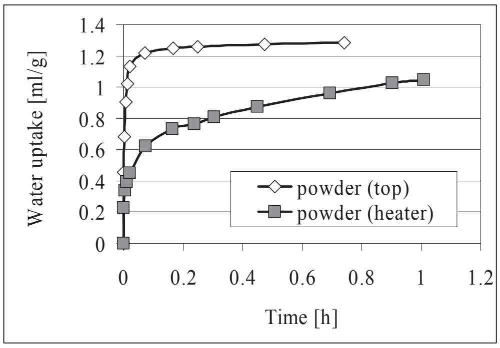

Figure 8: **Water uptake by selected samples from vertical positions at the top and near the heater under free swelling conditions.**

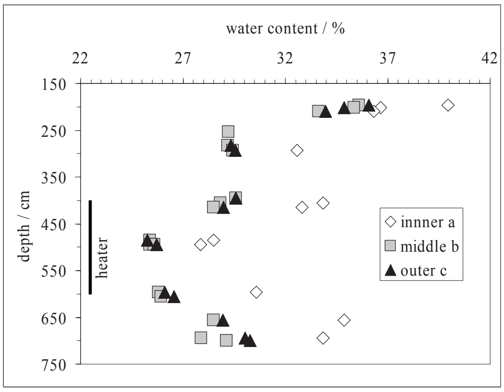

Figure 9: **Distribution of the on site gravimetric water content in the bentonite.**

Dismantling analysis – host rock

The mineralogical, mechanical, and hydraulic properties of the Opalinus Clay were determined in laboratory and in situ tests. The results of the investigations were input into the constitutive equations of the numerical models.

Table 1: Results of laboratory measurements of the linear thermal expansion coefficient α [1/K].

Laboratory	Inclination to bedding plane			Remark
	Parallel	Orthogonal	Other	
BGR (1)	1.2e-5 1.4e-5	2.5e-5 1.8e-5	-	Cooling, σ_{mean}=0.4MPa Heating, σ_{mean}=15MPa
BGR (2)	1.46e-5	5.13e-5	3.49e-5	Inclination angle 45°
CIMNE	-	-	8e-5 to 14e-5	Inclination angle 65° to 70°

As a rule, pre- and post-heating tests were performed to investigate the influence of temperature. As the temperature increase was negligible due to the low thermal conductivity of the bentonite buffer, no clear indication of heat-induced changes could be determined. The mineralogical investigations were planned to improve the understanding of the mechanical behaviour. The chemical composition of the Opalinus Clay proved to be very homogeneous and mechanical properties in the laboratory are mostly influenced by the microscopic structure of the clay sample (KLINKENBERG et al. 2005).

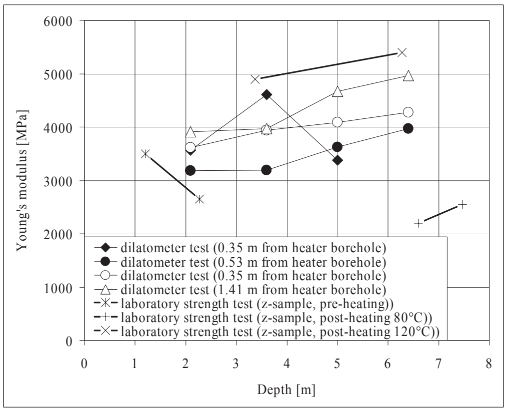

Figure 10: Measurements of Young's modulus of Opalinus Clay in the vicinity of the heater borehole from dila-tometer and laboratory tests.

Laboratory tests of rock mechanical properties (uniaxial and triaxial compression tests, Brazilian tests, and cubic samples in a true triaxial cell) were used to determine the elastic parameters (e.g. Young's modulus, Poisson's ratio) and failure strength of the orthorhombic host rock. Additionally, Mohr-Coulomb parameters (friction angle, cohesion) were derived from measurements. A rheological model (Burger's model) was used to describe the coupled elastic and creep behaviour. From heating and cooling tests, the linear thermal expansion coefficients were determined with respect to bedding direction (Table 1), andclearly display anisotropic material properties. Water retention curves and the hydraulic conductivity of saturated and unsaturated samples were also determined in laboratory experiments.

Immediately after switching-off the heater, 5 boreholes were drilled in the vicinity of the heater borehole, at distances between 350 and 1500 mm. The drill cores were used for post-heating geoelectric, rock mechanical, and mineralogical laboratory tests. Geotechnical, hydraulic, and seismic field measurements in the boreholes gave

- Young’s modulus from dilatometer measurements,
- Hydraulic permeabilities from pulse tests, constant head and constant rate injection tests, and
- P-wave velocities as a function of depth, indicating the extent of the excavation damaged/disturbed zone (EDZ/EdZ) and structural inhomogeneities of the host rock.

Young’s modulus increases with the depth of the borehole and the distance from the heater borehole. A comparison between the in-situ measurements and comparable laboratory results for samples in the z-orientation (i.e. at an inclination angle of 45°) show both sets of data in the same range (Figure 10). Compared with typical results for Opalinus Clay, the values are about 30 to 40% lower than expected (e.g. BOCK 2001).

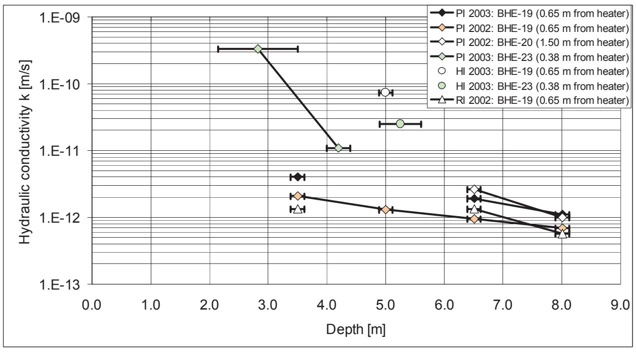

Figure 11: Results of hydraulic tests close to the heater bore-hole before and after the heating period. The abbreviations are as follows: PI – pulse injection test, HI – constant head injection test, RI - constant rate injection test.

The hydraulic conductivities in the heater niche were measured before and after the heating period. Compared with typical values for the Opalinus Clay matrix that lie between $5 \cdot 10^{-13}$ and $1 \cdot 10^{-12}$ m/s (Bock 2001), the rock in the heater niche shows a conductivity around one order of magnitude higher (Figure 11). The modelling parameters derived from the best fit of pore-water pressure measurements lie between $3.5 \cdot 10^{-19}$ and $8 \cdot 10^{-19}$ m^2 and are thus closer to the typical excavation damaged zone (EDZ) values (cf. GAUCHER et al. 2003).

Nevertheless, seismic measurements of interval velocities along the boreholes indicate that the EDZ does not extend beyond about 2 m depth (Figure 12). The P-wave velocity profile over depth displays features such as sandy layers interspersed within the shale clearly by velocity peaks. In the south-eastern half of the niche, a lower rock quality can be recognized by a larger scattering of the data.

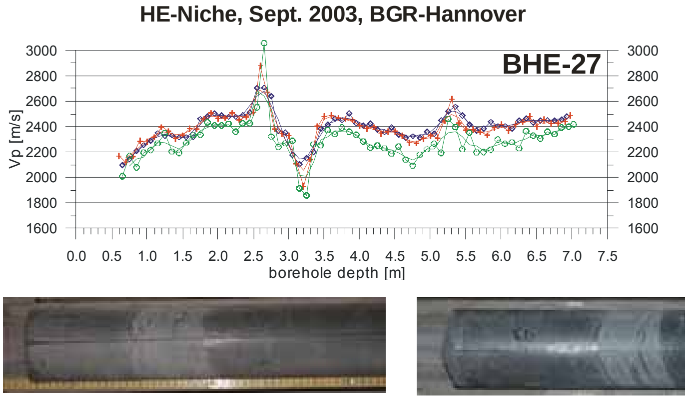

Borehole core BHE-27, 2.35 to 2.80 m depth, shale with inclusion of sandy layer

Borehole core BHE-27, 4.90 to 5.3 depth, shale with inclusion of sandy

Figure 12: Profiles of P-wave velocities over depth from seis-mic interval velocity measurements in borehole BHE-27 at 1.41 m distance from the heater borehole in the western part of the HE niche. Photographs of borehole cores show sandy layers that result in higher P-wave velocities in the profiles.

Modelling

The performance of the engineered barrier depends on its design and its interaction with the host rock. Identification and quantification of the interactions by investigation is complemented by modelling to improve the understanding of coupled processes and to validate the models. Modelling of the heater test was therefore performed for back-analysis as well as for prediction. The HE experiment allowed refinement of the finite element programmes used. Besides using axisymmetric models, the Opalinus Clay was modelled as the transverse isotropic material it really is, with laboratory and in situ experiments providing information on the material parameters needed for the constitutive equations.

The **near-field model** comprises the most important technical features of the engineered barrier. It includes all sequences in the history of the test, beginning with the excavation of the HE niche. Modelling the initial phases of the experiment is of vital importance, since they control the initial stress state and the pore pressure for the subsequent phases. The **far-field model** deals with the THM interactions in the host rock only.

Near-field models

The simplest model was axisymmetric. Comparison with monitoring results shows that the evolution of stress state and pore pressure during niche excavation and borehole drilling could be reproduced well. During the hydration phase, the high initial suction of bentonite induced an unsaturated state in the surrounding rock, reaching a maximum at a radial distance of 0.70 m. The desaturation and subsequent resaturation took place in approximately 200 days. The hydration of the bentonite generated high swelling pressures, reaching a maximum value of 14 MPa in the rock close to the interface. The bentonite swelling pressure produced significant changes in the stress state in the surrounding rock, affecting a zone of 1 m diameter. Plastic strains were produced in a narrow zone of the rock (diameter 0.05 m) adjacent to the bentonite-rock interface. The post-dismantling analysis showed that the in situ behaviour was different (see section on bentonite).

Modelled temperatures during the heating phase are close to the measured values. The area with increased temperature extends to a maximum radial distance of 5.0 m. The increase in the pore pressure and the subsequent dissipation measured during heating are well reproduced by the model. The positive pore pressure generated by temperature increases causes a drop in the effective stress, which implies a certain loss of rock strength. The magnitude of pore pressure increase is controlled by the rate of temperature increase, the rock permeability, the rock porosity, the rock stiffness, and the geometry of the experiment. The heating phase generates a transient change in the total and effective stresses. Successive heating extends the annular zone of plastic strain to a maximum diameter of 0.08 m. The latter, as above, could not be confirmed in situ.

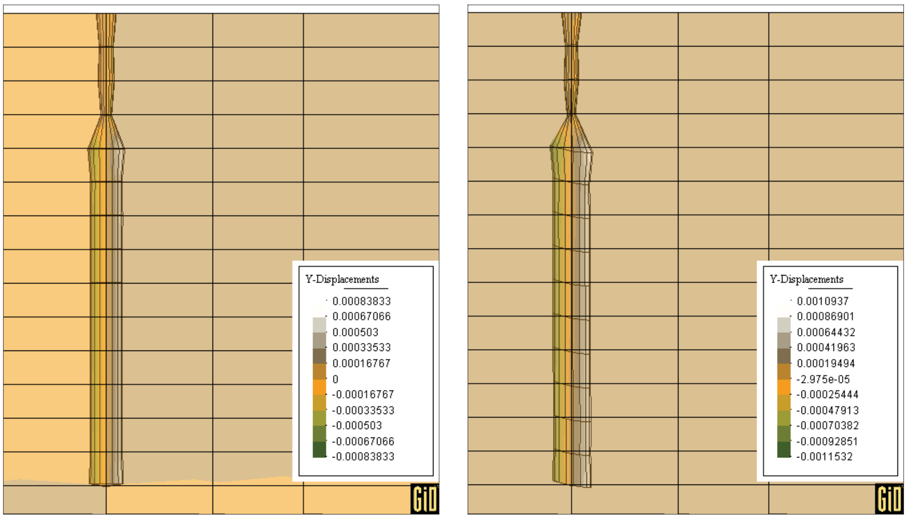

Figure 13: Displacement in Y direction. Isotropic model (left) and anisotropic model (right) during heating phase, t = 1070 days.

The cooling phase induces a reduction in pore pressure, the magnitude of which depends on the rate of the temperature decrease. The pore pressure reaches a stable state after approximately 250 days of cooling. Cooling implies a transient change in total and effective stresses. On the long term, steady state stresses do not seem to be affected by the heating and cooling phases.

To better represent the mechanical behaviour of the Opalinus Clay, an anisotropic elasto-visco-plastic model was developed. A significant proportion of the material parameters were taken from tests performed on the Opalinus Clay as part of the HE experiment. The constitutive model was calibrated by triaxial laboratory tests and the variation in rock strength with the angle of dip could be compared satisfactorily with laboratory results.

A three-dimensional (3D) finite element (FE) model was developed to reproduce the HE experiment, where the bentonite swelling was represented by a uniform pressure. Significant differences between the isotropic and the anisotropic models have been found in the

- direction and intensity of displacements
- stress distribution and
- plastic zone developed.

Points located at the same radial distance from the HE borehole axis but at different positions in the circumferential direction, show significantly different responses. Particularly sensitive are the calculated radial displacements caused by borehole heating (Figure 13).

Far-field models

A THM-version of the MEHRLIN code was developed by adding the thermal reaction. Verification and testing showed that the overall observed behaviour of the measurements with respect to TH-processes could be well reproduced by an axisymmetric model (Figure 14). The thermal parameters obtained by numerical fitting to in situ observations correspond well with the values measured on samples in the laboratory. Based on the data available, the work was not conclusive with regard to the simulation of mechanical effects: it was found that the volume of rock undergoing a rise in temperature by more than a few degrees was relatively small. The pore-water pressure rise due to heating was important, as expected in the low-permeability Opalinus Clay. The induced changes in effective stress are equally important and can, at least for low effective stress conditions, clearly not be ignored, both for mechanical stability (where applicable) and for changes in volumetric rock deformation and/or damage with the consequences for rock permeability and the creation of preferential features (fractures) and the integrity of the barrier. This aspect would be of key importance for design purposes, i.e. the back-fill material and geometry, as well as the maximum permissible heat load.

More detailed numerical THM-analysis of this and further experiments with various thermal loadings, based on THM coupled laws, are necessary in order to be able to predict the engineered barrier and Opalinus Clay performance with respect to effective stress-induced volumetric rock deformation.

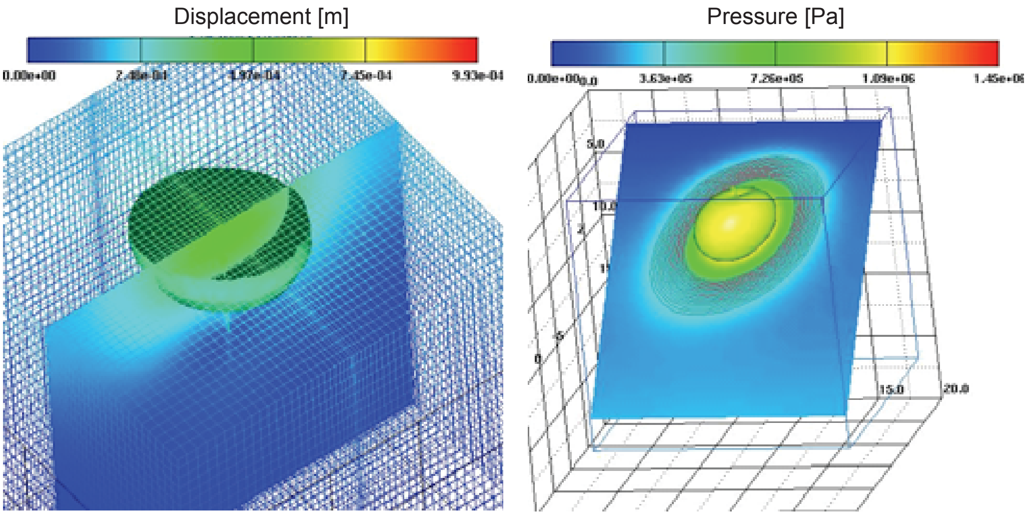

Figure 14: Results for anisotropic heat conduction: Displacement and pressure in the calculation domain (at time t = 170d).

Summary and conclusions

The continuous monitoring of the experiment by a large number of sensors (temperature, pore pressure, total pressure, relative humidity, and radial displacement) has generated a database reflecting the sequence of the experiment from hydration through heating to cooling. Nevertheless, the monitoring part of the experiment was less successful than expected: the dismantling confirmed that sensors installed in the bentonite buffer and its vicinity were, in most cases, not resistant to the conditions during hydration. Although some manufacturing problems were solved prior to installation, numerous sensors corroded in the presence of Pearson water, in some cases caused by manufacturing or construction defects (e.g. thermocouples, pore-pressure and relative-humidity sensors). Most sensors in the peripheral boreholes remained intact. The stainless steel 316L proved resistant to corrosion in situ.

Geoelectric measurements were another part of the continuous monitoring programme. They showed no decrease in the water content in the vicinity of the heater during the heating phase. Decreasing energy input to the heater element over time suggests that the bentonite dried out, leading to a decrease in its thermal conductivity. This was confirmed by laboratory results after dismantling. Gas release during heating showed a peak in the release of hydrogen sulphide – another possible corrosion agent - close to the heater.

The monitoring programme was complemented by a substantial laboratory programme for determining thermal, hydraulic, and mechanical properties of the host rock and providing input data for most of the parameters needed in the constitutive equations of the finite element codes. A post-heating drilling campaign in the HE niche provided samples for laboratory tests and allowed in-situ measurements for mechanical, hydraulic, and seismic information on the host rock that supported the laboratory results. With regard to heat-induced changes in bentonite and Opalinus Clay, no conclusive answers could be found because, for both clays, the temperatures were too low.

The monitoring database was used to validate and refine the finite element codes and the numerical models of the experiment. Numerical modelling of the near-field also served as an instrument for the prediction of experimental results and was useful for steering the experiment. The host rock was simulated in axisymmetric models as homogeneous and isotropic, as well as in full 3D models as an anisotropic (approximately transversely isotropic) medium. The most salient features of temperature and pore pressure development could be modelled well by the axisymmetric as well as by the 3D models. The swelling of the bentonite was far less pronounced in reality than in the near-field model. Differences in the determination of the radial displacements in the HE borehole are probably caused by some problem with the sensors. Regarding heat-induced changes in bentonite and, particularly in Opalinus Clay, future heater experiments should consider the use of a different test configuration to get more representative repository conditions, meaning higher temperatures on clay.

The continuous monitoring in conjunction with the numerical modelling improves the understanding of THM processes in a bentonite barrier and the surrounding rock. For future heater experiments, preparation of the experimental set-up by numerical simulation would be a constructive approach. For the installation, the role of corrosion should not be underestimated.

Table of contents

1. Objectives and strategic needs

1.1 Project objectives

As part of the fifth EURATOM Framework Programme, the EURATOM work programme defined the “safety of the fuel cycle” as one of the key aspects, with the specification of the “safety assessment of nuclear waste disposal in the deep geologic underground”. The long-term safety of geological repositories for radioactive waste depends on a combination of engineered and geological barriers. In the heater experiment (HE), the interactions between a bentonite buffer and an Opalinus Clay host rock formation were observed under thermal and hydraulic conditions close to the situation in a high-level waste repository. Hydration of the buffer at the beginning of the experiment was followed by a heating phase (cf. Figure 1.2 with the overall time-table of the experiment). The objective of the experiment was to improve the understanding of the coupled thermo-hydro-mechanical (THM) processes in a host rock-buffer system based on experimental observations and numerical modelling. The main objectives were

- Long-term monitoring in the vicinity of the heater during hydration and heating, particularly the observation of coupled THM processes in the near-field, i.e. continuous measurement of temperatures, pore pressures, displacements, and electrical conductivity and analysis of gas and water released into the rock by the effect of heating.

- Determination of the properties of the barrier and the host rock by laboratory and in situ experiments, i.e. measurement of the thermal, hydraulic, and mineralogical properties, the mechanical and hydraulic state in-situ and the changes induced by the experiment.

- Study of the interaction between the host rock and the bentonite buffer, as well as the validation and refinement of existing tools for modelling THM processes (i.e. the finite element codes CODE_BRIGHT and MEHRLIN).

- Study of the reliability of instrumentation and measuring techniques, e.g. by the inspection of sensors after dismantling the experimental set-up.

By calibrating modelling results with monitoring data, the experiment aimed to reduce the degree of uncertainty associated with all types of long-term prediction. The insights gained from a thorough analysis of experimental conditions and processes contribute to an improved scientific basis for the safety assessment of radioactive waste disposal in the deep geological environment.

1.2 Work programme

The HE experiment was performed in the Mont Terri Rock Laboratory in Canton Jura in the northwest of Switzerland. A niche was purpose-built in the shaly facies of the Opalinus Clay formation. The installation of the test was carried out as a Mont Terri Project, while the main part of the experiment was partly financed by the EC.

A heater element was installed in a vertical borehole drilled into the niche floor. Artificial hydration with synthetic formation water was sustained for 35 months (Figure 1.1), before the heater element was put into operation for 18 months. The experiment was then dismantled to provide valuable information on the post-hydration and post-heating state of the buffer, host rock, and instrumentation. The work programme for the HE experiment was broken down into 5 work packages (WP), plus co-ordination, reflecting either the course of the experiment (such as WP 1, 2, and 4) or merging activities running in parallel, such as WP 3 and 5:

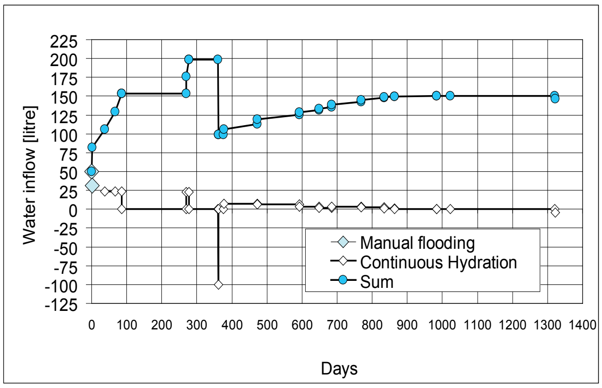

Figure 1.1: Hydration process of the bentonite buffer.

1. Test plan preparation
2. Operational phase
    - Supervision and data management
    - Geoelectric measurements
    - Gas and water sampling and analysis
3. Laboratory tests
    - Pre-dismantling laboratory tests
    - Post-dismantling rock mechanic analysis
    - Geoelectric calibration
    - Gas content and release
    - Bentonite analysis
    - Instrumentation analysis
4. Dismantling
    - Engineering design
    - Dismantling
    - Borehole measurements
5. Modelling
    - Near-field modelling
    - Rock modelling
6. Project co-ordination

The installation of the experiment is described in chapter 2. The monitoring installations and an overview of the most important monitoring results are given in chapter 3. The dismantling of the experiment after 35 months of hydration of the bentonite buffer and 18 months of heating is described in section 4.1, with the main findings on the geology around the heater element given in section 4.2, and the results of the instrumentation analysis summarised in sections 4.3f. The characterisation of the buffer material is presented in chapter 5 and the corresponding results for the host rock can be found in chapter 6.

Modelling of the near-field was used throughout the experiment to interpret the monitoring data and to adapt the experimental procedure. The main results are summarised in chapter 7. A simpler and less detailed modelling technique for the far-field was used in the rock modelling work package, the results of which can be found in chapter 8.

1.3 Innovative aspects

The HE experiment was planned as a complex test of a particular method for the disposal of high-level radioactive waste, designed on a reduced scale under conditions simulating phenomena that are typical for long-term evolution scenarios (such as hydration and heating). The experiment also posed challenges on the operational side and raised a number of questions regarding physical interactions in THM processes. As numerical modelling played a key role in the planning of the experiment, a number of material parameters as input to the constitutive equations of the finite element programmes had to be determined. Hence, the innovative aspects that evolved during the course of the experiment were considerable. In the following, the innovative aspects are compiled in the form of a brief overview. Discussions can be found in the subsequent chapters of the report.

Topics related to the scientific aspects of THM processes were the

- Changes induced by the THM processes related to hydration and heating, with regard to bentonite buffer, host rock, and instrumentation
- Interaction of the buffer (compacted bentonite) and host rock (claystone); here no prior experience was available
- Research on the behaviour of a particular type of bentonite, compacted into blocks, under hydration and heating conditions, particularly with regard to swelling and self-sealing properties
- Heat transport in the Opalinus Clay and extent of the temperature field, as well as the influence of THM processes on the heat transport
- Extent and role of the EDZ in the experiment
- Corrosive action of the clays in the buffer and host rock with respect to the metals used in the field, with investigation of the geochemical processes involved
- Monitoring and modelling of THM processes by determining the distribution of key parameters such as temperature, humidity, total pressure, pore pressure, etc.
- Monitoring of gas and water release

In relation to operational issues, the following topics were of interest and solutions were proposed:

- Development of an artificial hydration system for the bentonite buffer that allows fast saturation with high-salinity water with properties similar to the pore-water in the consolidated clay (synthetic formation water)
- Dismantling of the experiment using appropriate and cost-effective measures to obtain undisturbed samples of bentonite and Opalinus Clay and to retrieve most of the sensors
- Development of cost-effective means for the preparation, transport, and storage of Opalinus Clay samples from the test site to the laboratories of the partners

Support for the interpretation or prediction of processes was included in the research programme for the

- Calibration of geoelectric data in Opalinus Clay
- Calibration of gas release in Opalinus Clay
- Determination of the mineralogical and mechanical properties of bentonite blocks and Opalinus Clay before and after heating in the laboratory
- Determination of mechanical properties in situ after heating and comparison with laboratory results
- Determination of the anisotropic properties of the Opalinus Clay in the laboratory complemented by laboratory results for hydraulic properties

In the field of modelling, the following improvements were made:

- Development of the MEHRLIN finite element code from TH to THM coupling for the modelling of the host rock
- Development of the finite element code CODE_BRIGHT to model anisotropic behaviour (i.e. transverse isotropic, as the Opalinus Clay proved to be)
- Both codes used in the HE experiment (MEHRLIN and CODE_BRIGHT) modelled the THM behaviour in the HE experiment for the anisotropic Opalinus Clay and compared it to the results of isotropic models
- Although some of the in situ measurements did not yield the expected volume of data because corrosion was unexpectedly severe, comparisons between measured and calculated results are encouraging.

At BGR, the HE experiment triggered research resulting in a doctoral thesis by WOLTERS (2005) and Martina Klinkenberg is currently working on a doctoral thesis with the title “The influence of microstructure on rock mechanical properties”, see KLINKENBERG et al. (2005).

2. Description of the experiment

2.1 Configuration

The HE experiment was developed in a purpose-built niche in the shaly facies of the Opalinus Clay formation. It is identified as the HE niche and is located in the western wall of the new gallery in the Mont Terri Rock Laboratory (see Figure 2.1 and section 4.2.1, p. 27).

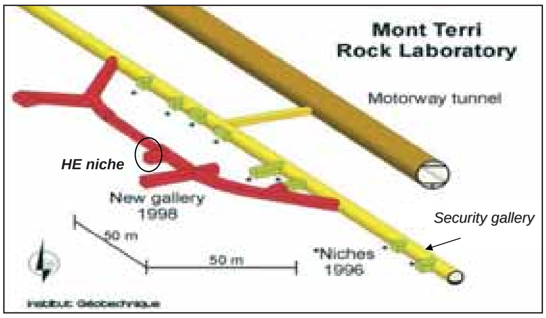

Figure 2.1: HE niche at the Mont Terri Rock Laboratory

A plan view of the test layout is shown in Figure 2.2. A central vertical borehole (BHE-0) 300 mm in diameter and 7.5 m long was drilled in the niche floor. A heater tube was installed in this borehole, surrounded in the bottom part by a bentonite buffer 5.1 m in height made of ring-shaped compacted bentonite blocks with a dry density of 1.8 g/cm^3. The bentonite used (so-called FEBEX bentonite) was non sodium-activated from the La Serrata area in Almería (Spain). Several sensors were installed in the bentonite buffer to monitor temperature, total pressure, pore pressure, and humidity.

Due to the virtual absence of free water in the host rock formation, an artificial hydration system was needed to accelerate the hydration process in the buffer prior to the heating phase. A cylindrical ceramic filter was fixed to the outer part of the heater tube and connected to the niche equipment by means of four tubes for water injection. The gap between the bentonite buffer and the rock, as well as the upper part of the borehole, were filled with sand (see details in Figure 2.3).

The heater borehole was covered with a steel lid anchored to the rock to support the potential thrust caused by bentonite swelling. A sealing plug basically made of epoxy resin was installed in the upper part of the borehole, to provide gas and water tightness. Two pass-through pipes with a valve were installed across this plug to allow gas and water sampling and pressure monitoring. Finally, the 2 m long heater element was introduced into the inner part of the central tube with its upper end at a depth of 4 m below the niche floor.

A total of 19 boreholes were drilled into the niche floor for instrumentation purposes (see Figure 2.5). Sensors for measuring the most relevant rock parameters, such as temperature, humidity, mechanical pressure, pore pressure, displacement, and resistivity, as well as gas and water release, were installed in those boreholes: BHE-1 to BHE-4 for temperature and total pressure, BHE-5, -6, -19, and BHE-20 for pore pressure, BHE-7 for radial displacement, BHE-8 and BHE-9 for longitudinal and radial displacement (Trivec), BHE-10 to BHE-13 for gas and water sampling, and BHE-14 to BHE-17 for geoelectric tomography. Table 2.1 summarises all permanent HE sensors. All sensors of the experiment were identified with a code number of the type

SPPP_DD.DD/N

where

S	Type of sensor: T-Temperature thermocouple, P-Total pressure (absolute), Q-Pore pressure (absolute), E-Electrolevels (inclinometers), W-Water content (capacitive), G-Fluid pressure (relative)
PPP	Positioning zone: Boreholes: borehole code; Heating system: *HE;* Hydration system: *HY*
DD.DD	Depth in meters, with a maximum of two decimal places
N	Order number

The experiment was designed to run automatically and unattended, with remote supervision via modem (see section 3.1). However, some of the instruments (for example the continuous extensometer or Trivec) required manual operation. The information provided by the sensors during the experiment has generated a large database that has led to a better understanding of THM processes in the bentonite barrier and in the surrounding rock. This information has also allowed ongoing validation and refinement of the numerical codes used for modelling such processes.

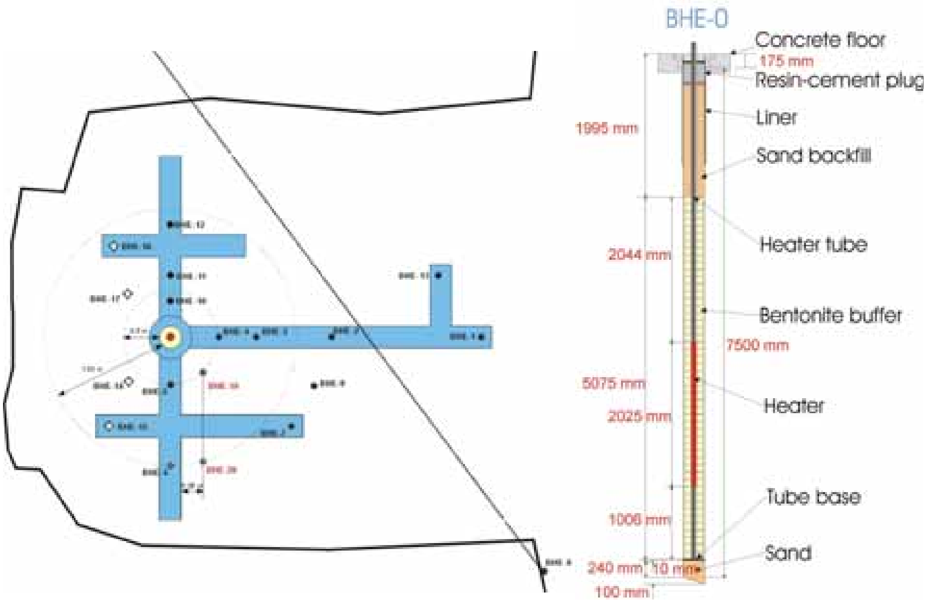

Figure 2.2: Layout of the HE experiment (plan view) and description of the central borehole BHE-0.

2.2 *Test installation*

The installation of the heater test was done prior to the EC contract as a Mont Terri Project and was performed according to the following sequence (see also Figure 1.2):

1. Niche excavation (March to April 1998)
2. Installation of the concrete floor and the cable channels (April 1999)
3. Drilling of roof and borehole cover bolts (April 1999)

4. Drilling of the heater borehole BHE-0 (27 April to 4 May, 1999)
5. Installation of the heater/buffer assembly and first hydration of the buffer (5 to 16 May 1999)
6. Drilling of instrumentation boreholes (from 17 May to 8 June, 1999)
7. Emplacement of instruments in boreholes, in parallel with drilling (from 17 May to 8 June, 1999)
8. Installation of data acquisition and control equipment (9 to 17 June, 1999)
9. Installation of the hydration system (niche components) (9 to 17 June, 1999)
10. Installation of heater and power regulation system (9 to 17 June, 1999)

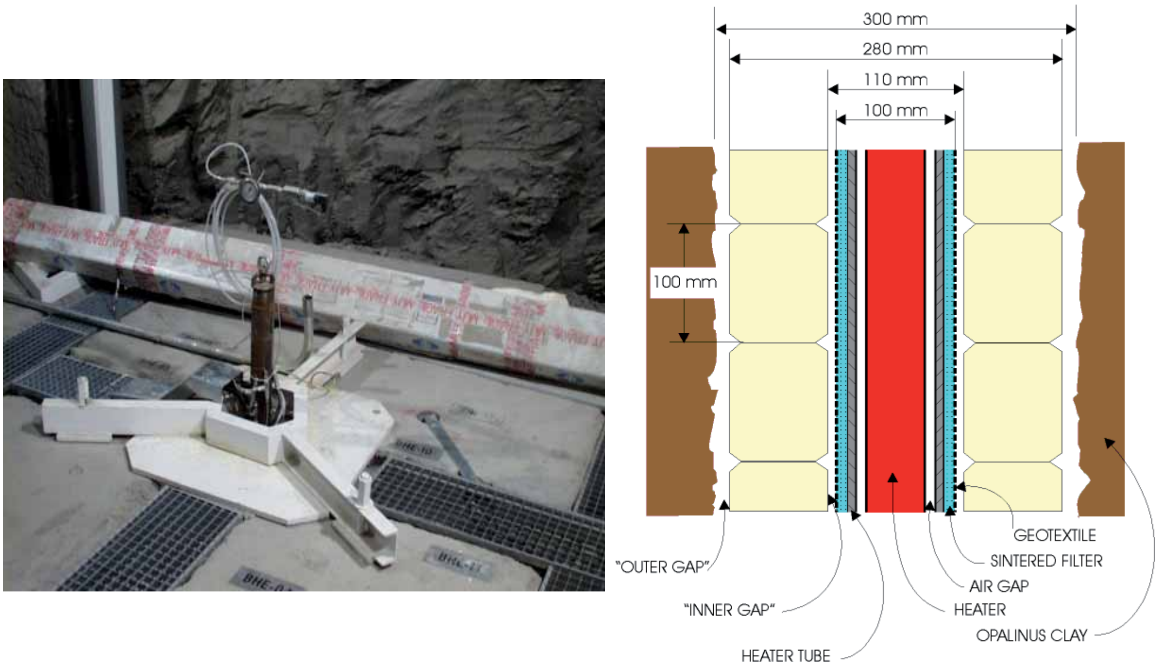

Figure 2.3: Detail of the heater borehole composition (heater and buffer).

Table 2.1: List of sensors installed.

Sensor type	Code	Heater	Hydr. System	Buffer	Rock (BHE-*)															TOTAL
		HE	HY	BHE-0	1	2	3	4	5&19	6&20	7	10	11	12	13	14	15	16	17	
Temperature	T	3		12+4	3	3	3	3	4	2										33
Total pressure	P			6	1	1	3	3												14
Pore Pressure	Q			11					5+5	3+3										27
Water content	W			5								1	1	1	1					9
Electrolevel	E										11									11
Fluid pressure	G		5																	5
Weight (level)	M		1																	1
Voltage meter	V	2																		2
Current meter	I	2																		2
Electrode chains	R															1	1	1	1	4
Packer	C											1	1	1	1					4
		9	6	34	4	4	6	6	9	5	11	2	2	2	2	1	1	1	1	112

The main difficulty was caused by the restricted height of the niche, which made it impossible to assemble all elements necessary for the buffer/heater setup before their insertion in the BHE-0 borehole (see Figure 2.4).

2.2.1 Flooding of the buffer gaps

Due to the virtual absence of free water in the host rock, the bentonite buffer was artificially hydrated to reach saturation as soon as possible. The water used was synthetic experimental water (Pearson's water A1 type, cf. section 3.4.2, p. 21), which is chemically similar to the water in the Opalinus Clay formation. The hydration was carried out in two stages: the first stage consisted of filling the sand and the construction gaps manually with synthetic water from the top of the borehole, just after the buffer/rock gap was backfilled with sand. The total amount of water introduced in this stage was 81.74 litres (May 1999). The second stage was done during test operation just after completing the test installation (see chapter 2.3.1).

Figure 2.4: Detail of the heater/buffer assembly installation.

2.3 Test operation

2.3.1 Buffer saturation

The second stage of hydration, also called *continuous buffer hydration*, was started on 15 June, 1999 and was done using the automatic hydration system (see Figure 2.6) until complete saturation of the buffer was reached by mid-October 2001.

Table 2.2: Record of injection since the start of the project.

Type of injection	**Dates**	Volume of water
Manual injection (before plug emplacement)	From 08/05/99 to 09/05/99	81.74 litres
Hydration system (at atmospheric pressure)	15/06/99	Start-up of injection
	From 15/06/99 to 03/08/99	71.71 litres
	From 04/08/99 to 07/02/00	Injection stopped
	From 08/02/00 to 15/02/00	45.47 litres
	From 16/02/00 to 24/05/00	Injection stopped
	From 25/05/00 to 31/08/00	13.97 litres
	From 31/08/00 to 31/12/00	12.64 litres
	From 31/12/00 to 26/02/01	6.28 litres
	From 26/02/01 to 31/03/01	3.46 litres
	From 31/03/01 to 24/06/01	7.16 litres
	From 24/06/01 to 30/08/01	5.53 litres
	From 30/08/01 to 30/09/01	1.82 litres
	From 30/09/01 to 31/01/02	0.27 litres
	From 31/01/02 to 08/03/02	0.46 litres
	From 08/03/02	Injection stopped

2.3.2 Injection record

A total of 150.51 litres were injected into the system from the beginning to 8 March, 2002. Table 2.2 shows the hydration record and Figure 1.1 shows the water inflow graphically.

2.3.3 Pre-heating phase incidents

Several incidents described hereafter were recorded during the continuous buffer hydration phase.

2.3.3.1 Failure of BHE-0 thermocouples

Almost all of the thermocouples installed in borehole BHE-0 failed several days after finishing the test installation on 3 June, 1999, probably due to the first stage of the buffer hydration (i.e. flooding of the buffer gaps). Therefore, from 18 to 22 October, 1999, four new thermocouples were inserted in the existing water injection tubes in positions close to the heater to allow adequate monitoring of the maximum temperatures in the buffer.

2.3.3.2 Failure of BHE-0 total pressure cells

Several hours after the manual flooding, the total pressure cells in borehole BHE-0 began to fail. Only the cell installed under the plug, which is in a relatively dry position, remained operational. The failure was due to a manufacturing defect which meant that the cell cable entry was not watertight.

Figure 2.5: Three-dimensional (3D) view of HE boreholes.

2.3.3.3 Water leak detected in heater tube

By the middle of October 1999, water from the injection system was found inside the heater tube up to 1 m below the niche surface. After pumping out most of the water, a small water leak was found, apparently in the joint between the two sections of the tube (occasional drops observed). To stop the leak, a pneumatic packer was placed inside the tube, above the heater element, at the joint level.

On the date initially planned for starting the heating phase (15/02/00), an electrical failure in the heater was detected (short-circuit between damaged cables and rock), caused by the presence of water in the heater tube. Consequently, the heater and the packer assembly were removed from the BHE-0 tube, the hydration process was stopped to avoid further water losses and the start of the heating phase was postponed.

To solve the water leak problem, it was decided to install a new tube inside the existing one (09/05/00). The gap between the two tubes was filled with epoxy resin and closed at the top with a welded stainless steel part (see Figure 2.7). This solution required reducing the outer diameter of the heater element, but the length and the total power remained the same.

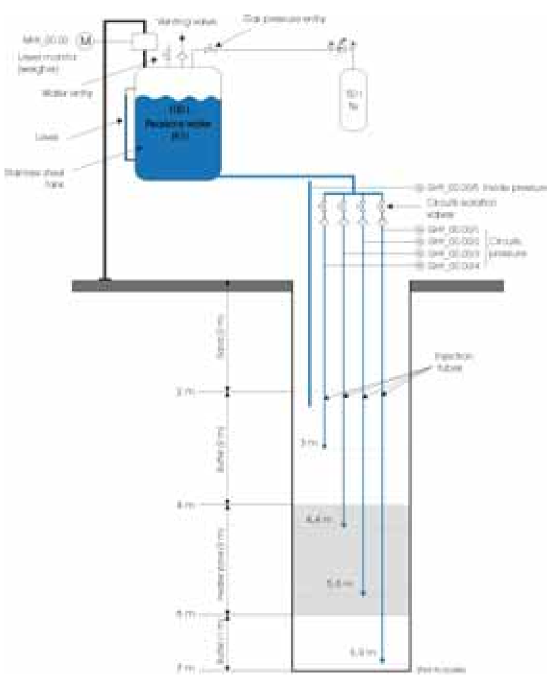

Figure 2.6: Scheme of the continuous hydration system.

2.3.3.4 Installation of the new boreholes BHE-19 and BHE-20

During the hydration phase, the in-rock pore pressure sensors installed in boreholes BHE-05 and BHE-06 at distances of 0.5 m and 1.5 m from the central borehole BHE-0, respectively, showed a very slow response. Therefore, from 27 to 28 February 2000, two new boreholes, BHE-19 and BHE-20, were drilled close to BHE-05 and BHE-06. In March 2000, the new boreholes were equipped with PP type piezometers, which normally show a faster response at the Mont Terri laboratory. Consequently, and to allow water pressure build-up, as well as the complete saturation of the bentonite buffer with water, the beginning of the heating phase was scheduled for a later date.

2.3.4 Heating phase

The heating phase was the first operating stage under the EC project, starting just after completion of the hydration phase and after performing the hydraulic characterisation campaign. The heating phase started on 22 February, 2002.As initially planned, the first heating phase was carried out in several constant power steps to allow adjustment of the parameters of the temperature control loop. The first step had a value of 140 W, and the second step a value of 150 W; a third and fourth step of 285 W and 440 W, respectively, were then applied to the heater, reaching a maximum temperature in the bentonite blocks of about 68ºC (cf. Figure 3.2 on p. 14).

The temperature control loop was then adjusted using the data obtained. The power applied to the heater was automatically regulated by the monitoring and control system to maintain a constant temperature of 100ºC at the contact surface between the heater (in fact the ceramic filter, cf. Figure 2.3 on p. 10) and the bentonite buffer. The hottest point was located at the level of the centre of the heater, so this point was used as reference for the power control.

When the heating period had been completed, the system was cooled down to a temperature that allowed access for dismantling (max. 40ºC). The heating phase had a total duration of 18 months, from February 2002 to the end of August 2003.

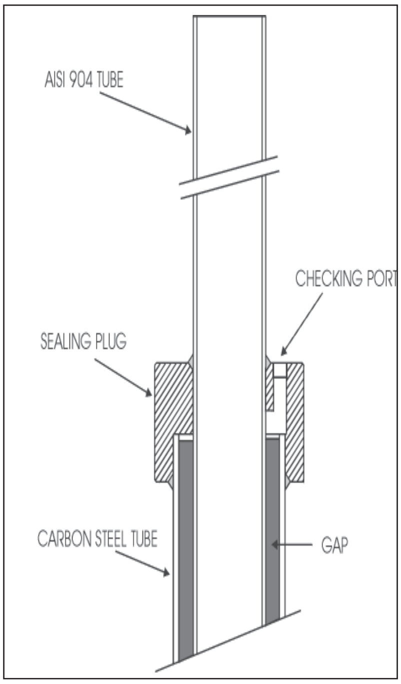

Figure 2.7: Detail of the two concentric heater tubes (top part).

2.3.5 Chronology of the experiment

Table 2.3 shows the chronological development of the HE project; cf. also Figure 1.2 on p. VI.

Table 2.3: Details of work phases in the heater experiment.

Phase	Date
Installation of the experiment	May to June 1999
Saturation phase	May 1999 to March 2002
Heating phase	22 February 2002 to 1 September 2003
Cooling phase	September 2003
Drilling phase	October 2003
Dismantling phase	20 October 2003 to the end of December 2003 (DAS dismantled in January 2004)

3. In-situ monitoring results

3.1 Supervision and data management

3.1.1 Monitoring and control system

The design of the monitoring and control system was determined by the requirements of unattended operation and the remote control characteristics of the experiment. This led to two different subsystems, one for the HE niche named LMS (Local Monitoring System, cf. Figure 3.1), and another for the AITEMIN control office in Madrid, called RMS (Remote Monitoring System), both linked by modem.

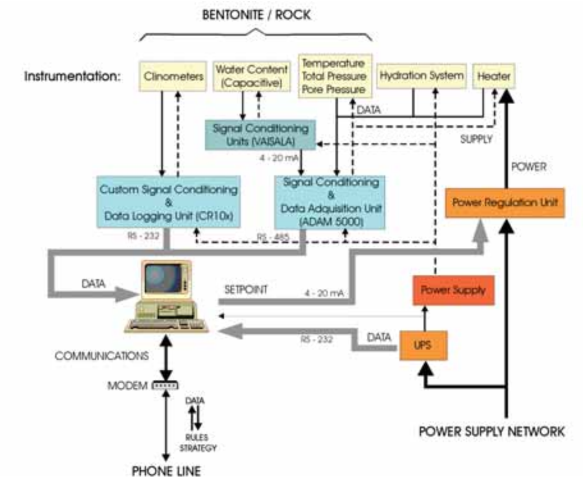

Figure 3.1: Scheme of the Local Monitoring System (LMS).

The LMS included a signal conditioning and data logging system, an instrumentation power supply, a heater power regulation unit, a host computer (PC) and an uninterrupted power supply system. Due to the special characteristics of some instruments such as electrolevels or humidity sensors, it was not possible to integrate the conditioning modules of all sensors into a single unit. It was therefore necessary to provide conditioning units dedicated to each type of sensor.

The host computer of the LMS read the data from the respective signal conditioning and data logging units. Data were processed, visualised, and stored in an internal data-base. The computer also generated the power set point for the heater power regulation unit as a function of the programmed control strategy.

The RMS located at the main office of AITEMIN in Madrid performed the experiment remote supervision and data analysis functions. The data base stored on the local PC at Mont Terri secured the average values of the measurements every hour. Data were collected by the RMS twice a week to update the experiment data-base and to make the analysis necessary for the heater control strategy, or to detect monitoring and control malfunctions. If necessary, it was also possible to connect by RMS to LMS for real time monitoring of the test.

3.1.2 Data reporting

After the conclusion of the HE installation on 17 June, 1999 (day 0 in the data graphs), the data acquisition system started collecting data and remote supervision of the experiment began. All information gathered was stored and analysed. The data obtained were displayed in graphical form (data trends) and – supplied with comments - distributed as data reports to the project partners almost every three months. Five data reports were delivered before the EC contract began and six reports were delivered during the EC contract.

3.2 Monitoring results

3.2.1 Temperature

The temperature data collected by the thermocouples on the heater element have shown fairly constant behaviour since the end of April 2002. The maximum temperature was registered in the upper zone of the heater. These thermocouples were disconnected during preparatory work shortly before the dismantling operation and the extraction of the heater element. After the end of heating on 1 September, 2003, temperatures decreased very rapidly, reaching values of about 48ºC on the second day, 2 September, 2003.

Data obtained by BHE-0 thermocouples (external to the heater element, in the bentonite blocks) showed an almost constant value up to the stop of heating. The evolution of temperatures and power applied to the heater is shown in Figure 3.2. The thermocouples in peripheral boreholes showed increasing temperature readings from the start of the heating, changing this trend to a more stable one in the last months of the heating phase (see an example in Figure 3.3).

After the end of the heating phase, a general decrease in the temperature registered by all sensors was recorded, with a minimum value of 18.7 ºC in BHE-4 (i.e. 0.65 m from the heater borehole). In boreholes closer to the heater borehole BHE-0, the change was also significant. Figure 3.4 shows temperature profiles in the rock formation since the start of the heating phase.

3.2.2 Pore pressure in the rock

As shown in Figure 3.5, all pore pressure sensors showed a similar evolution since the start of data recording. The general trend was a pressure build-up after the start of the heating phase. The maximum values registered differed, however, and were higher in borehole BHE-19, which, at 0.65 m from BHE-0, was located closer to the heater borehole than BHE-20 (at 1.5 m distance). After the initial pressure build-up, a pressure decrease was detected by all sensors. The end of the heating phase also influenced the values registered by the sensors, as they showed a clear pressure drop from the beginning of September 2003.

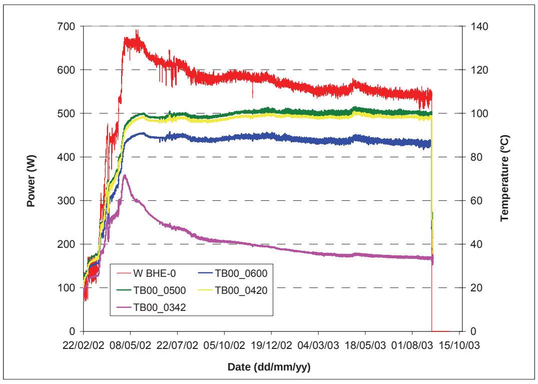

Figure 3.2: Evolution of applied power (W BHE-0) and temperatures in BHE-0 (numbers indicating the depth of the sensor in the vertical borehole, e. g. 0500 meaning 5 m, see chapter 2.1), versus time.

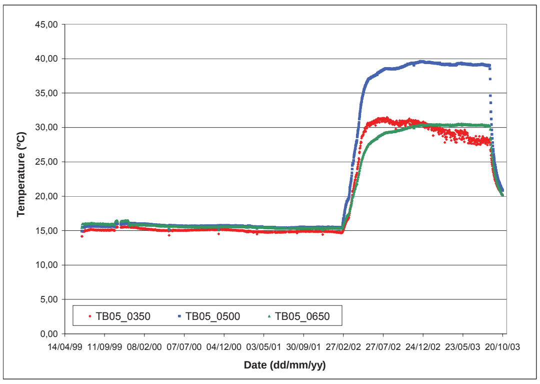

Figure 3.3: Evolution of temperature in borehole BHE-5 (about 0.65 m from the heater borehole).

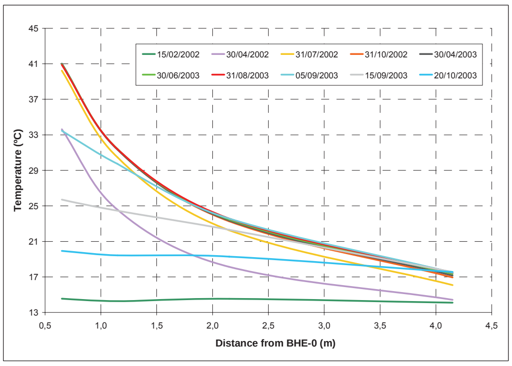

Figure 3.4: Evolution of temperature in the rock formation.

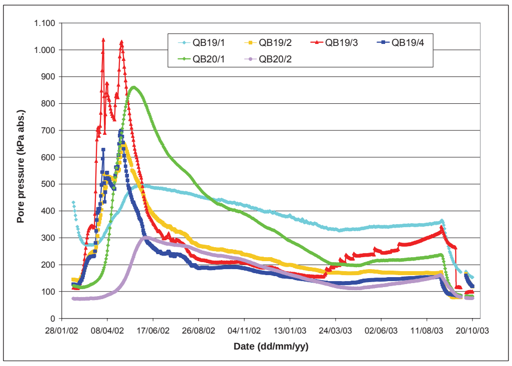

Figure 3.5: Evolution of pressure in boreholes BHE-19 and BHE-20. Depth of sensors is given by the suffixes /1 = 3.5 m, /2 = 5 m = mid-heater, /3 = 6.5 m, /4 = 8 m).

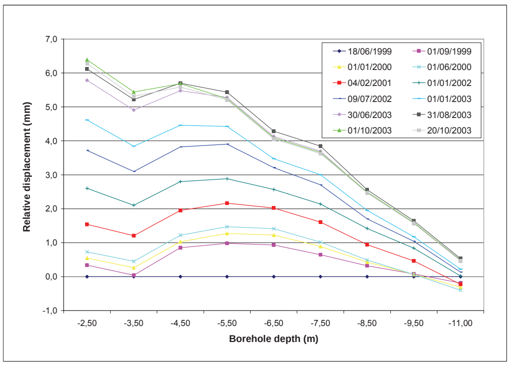

Figure 3.6 Temporal evolution of accumulated displacements.

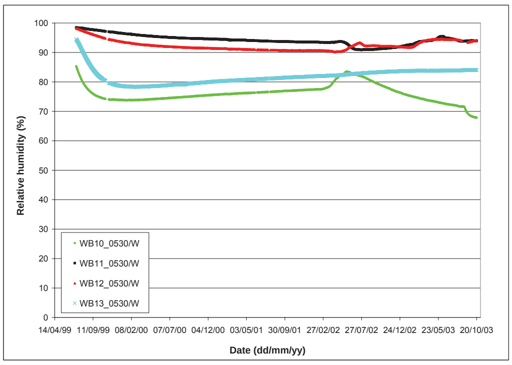

Figure 3.7: Evolution of relative humidity in boreholes BHE-10 to BHE-13.

3.2.3 Relative humidity

Humidity sensors installed in boreholes BHE-10 to BHE-13 showed different behaviour in the experiment, as can be seen in Figure 3.7. Most sensors suffered a perturbation at the start of the heating phase, which was more pronounced in those nearer to the heater (WB10_05.30/W in borehole BHE-10 about 0.5 m from the heater borehole, and WB11_05.30/W in borehole BHE-11 about 0.7 m away). WB13_05.30/W, installed in BHE-13 - the most distant borehole with about 3 m - did not register any change in trend caused by the beginning of heating.

3.2.4 Inclinometers (relative displacement)

Two types of inclinometers were used, those measuring radial displacements (nine sensors) and those registering perpendicular displacements. The angle variations registered by the inclinometers were very small. The graphs shown in Figure 3.6 represent the accumulated radial displacements in mm over time. According to these data, there was a progressive displacement from the heater, clearer in those inclinometers installed at depths closer to the heater (4.5 m, 5.5 m, and 6.5 m). The trend was maintained until the end of the heating phase (see the lines corresponding to June 1999 and August 2003).

The maximum displacement registered was about 5.5 mm, measured a few days after the end of heating, and in the inclinometer placed at 4.50 m depth. Beginning with the end of the heating phase, the displacements decreased slightly.

3.3 Geoelectric measurements and calibration

Geoelectric measurements make use of the relationship between water content and electric resistivity of rocks and engineered barrier materials. Geoelectric tomography in particular can be used to determine the resistivity distribution in larger areas of rock. Resistivity can be used to derive the pore-water distribution if calibration measurements are performed on samples in the laboratory. Repeated in-situ measurements allow temporal changes in water distribution to be determined.

3.3.1 Measurement and evaluation principle

An electric current is supplied to the formation via two electrodes. The magnitude and direction of the resulting electric field are dependent on the resistivity conditions in the rock. The potential difference between two other electrodes is measured. A large number of measurements with different current and potential dipoles is required to reconstruct the actual resistivity distribution. Measurements are evaluated by inverse finite element modelling. Starting with a usually homogeneous model, the expected vector of apparent resistivities for the set of measurement configurations is calculated and compared to the actually measured apparent resistivities. The model is then iteratively improved to minimize the deviations between calculated and measured values. GRS uses the commercial software package SensInv2D (Fechner 2001) which allows a two-dimensional inversion of the measured apparent resistivity data. The improvement strategy employed is the multiplicative simultaneous inversion reconstruction technique (MSIRT) of Kemna (1995).

3.3.2 Electrode array and measurement system

A total of 132 electrodes were installed in four boreholes in the test field (see Figure 3.8). The boreholes marked BHE-14 to BHE-17 have a diameter of 86 mm and a depth of 8.0 m each. They were drilled in May 1999. Immediately after drilling the boreholes, the electrode chains, each consisting of 33 electrodes with a spacing of 25 cm, were emplaced and then grouted with a special mixture of cement, Opalinus Clay powder, and water. The geoelectric monitoring system was installed in the Mont Terri tunnel in June 1999. It consists of an automatic computer-controlled measurement and data acquisition unit with multiplexers for addressing the electrodes and an external injection voltage supply.

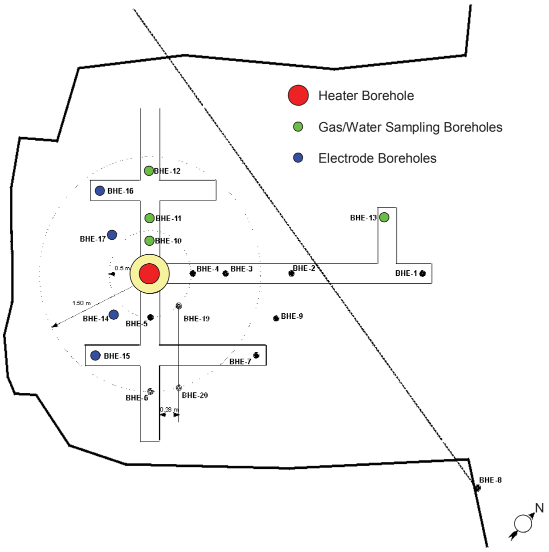

Figure 3.8: Plan view of the test field with the instrumentation boreholes.

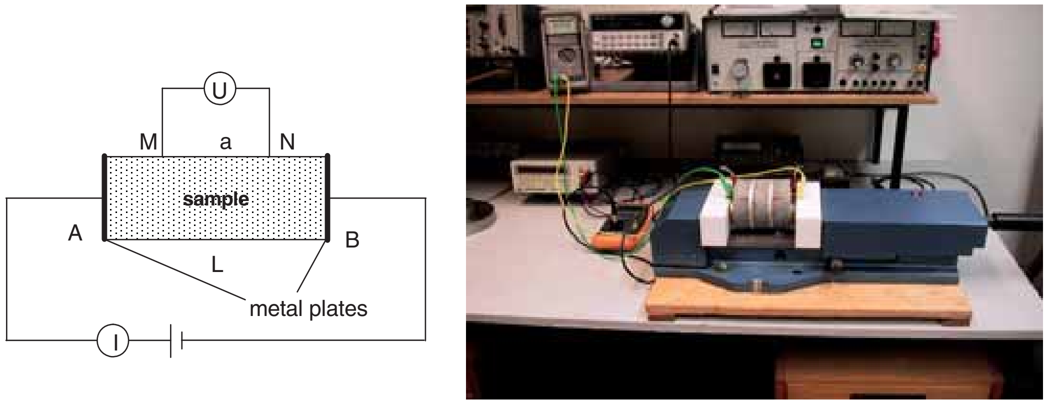

Figure 3.9: **Measurement set-up for clay rock resistivity (resistivity $\rho = \frac{U \cdot A}{I \cdot a}$ with U - electrical potential, A - cross section of sample, I - current, and a - distance of the electrodes M and N, see sketch).**

3.3.3 Laboratory calibration

To interpret the results for electric resistivity in terms of water content distribution in the rock, calibration measurements with samples of defined water content had to be performed in the laboratory. For the HE experiment, these measurements had to be performed at different temperatures, since the electrode array is located in the area of increased temperatures. The investigations on the samples were carried out in two different ways. In a first approach, the samples were investigated in the state of delivery, with a water content of about 4.6 to 6.2 wt.-% without initial resaturation. For these first investigations, the samples were dried under ambient temperature conditions to a water content of approximately 2.1 to 3.3 wt.-%. The resistivities at each drying step were determined using the four-point method. Here, the current I is injected at the end surfaces of the sample and the difference in the electrical potential U is measured at the voltage electrodes M and N (see Figure 3.9).

In the second approach, the samples were first saturated in an exsiccator at different air humidities of about 20 %, 42 %, 76 %, 90 %, and 100 %, respectively. To achieve the required air humidities, different salt solutions and water were used. To investigate the influence of temperature on the resistivity for each water content, the exsiccators with the samples were heated in an oven. Ensuring almost constant saturation conditions during the heating process, the samples were stored at the different air humidities. At each stage of saturation and temperature, the resistivities were measured in the same way as in the first approach and the water contents of the samples were determined. Since the water content is given by the ratio of wet mass and dry mass, the samples were finally dried at 105°C until the mass was constant. This is assumed to represent zero water content conditions. The actual water content was then calculated on the basis of the actual mass at the different saturation conditions.

The results of all geoelectric calibration measurements are shown in Figure 3.10. All resistivity curves show a decrease in resistivity with increasing water content. The results of the resistivity measurements at ambient temperature without resaturation are comparable to those with resaturation in the exsiccator. The figure also shows the dependence of resistivity on temperature. At higher temperatures, the resistivities decrease. This can be explained by the temperature dependence of the pore solution, because the conductivity of most electrolyte solutions increases with increasing temperature.

The resistivity increase at high water content for the 50°C- and the 70°C-curves is probably a measurement error introduced by evaporation of water at the sample surface during measurement.

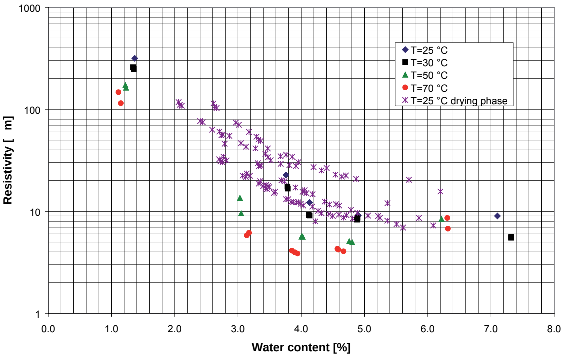

Figure 3.10: **Results of resistivity measurements at different temperatures as a function of the water content, determined in the state of delivery without additional saturation (approach1) and after saturation of the samples (approach2).**

3.3.4 Field results and interpretation

Geoelectric measurements had been performed in the plane between boreholes BHE-17 and BHE-16 since June, 1999, and in all planes between the four boreholes since July, 1999. Measurements stopped at the end of August, 2003, when heating was terminated and post-heating investigations started. Figure 3.12 shows inversion results for the planes between the boreholes BHE-17 and BHE-16, BHE-14 and BHE-15, and BHE-14 and BHE-17 in three-dimensional graphs, for the time between January 2002 and August 2003, all generated with SensInv2D. The electrode chains in the boreholes are depicted as black lines in the figures. Figure 3.12 shows, on the left hand side, the result of a measurement performed in January 2002, prior to the start of heating. Apart from the upper and lower ends of the model, which are influenced by boundary effects, the resistivity distribution is fairly homogeneous, with values of 7 to 20 Ωm that can be related to full saturation. A low-resistivity anomaly around 7 m depth is caused by the metallic heater. In February 2002, heating of the lower part of borehole BHE-0 was started. The tomogram from April 2002 (Figure 3.12, centre) shows a reduction in resistivity, particularly in the plane close to the heater borehole (between BHE-17 and BHE-14), which is due to an increase in conductivity of the pore-water caused by increasing temperature. From September 2002 on, the resistivity distribution changed only insignificantly until, in August 2003, the last measurement at the end of the heating period was made (Figure 3.12, right). It can be concluded that a steady state temperature field had been reached from around September 2002.

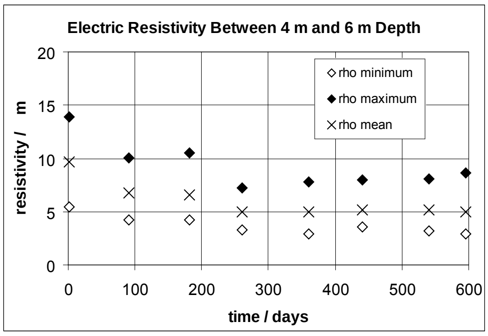

Figure 3.11: **Evolution of electric resistivity ρ between 4 m and 6 m depth in the plane between boreholes BHE-14 and BHE-17. Shown are the mean, maximum, and minimum values of resistivity.**

To better visualise the resistivity evolution, the time-dependent evolution of the mean resistivity in the heated area between the boreholes BHE-17 and BHE-14 is shown in Figure 3.11. The resistivity decrease during the first half-year of heating is caused by the temperature increase (until a steady temperature field is reached) and the subsequent steady-state resistivity can be seen clearly. In particular, no resistivity increase which could be attributed to desaturation effects was detected at any time.

Overall, it can be stated that the geoelectric measurements give no indication of heat-induced desaturation of the clay rock up to the end of the heating period. The only effect detected is a reduction in resistivity due to temperature increase. This result is confirmed by the post-dismantling investigations performed on samples from the test field.

3.3.5 Post-dismantling laboratory measurements

To check the in-situ results on the effect of heating on the water distribution, and thus on the resistivities in the HE niche, laboratory investigations on core samples collected after the heating phase were carried out. One borehole was drilled into the floor between the electrode chains BHE-14 and BHE-17 (the formerly heated region), and one at 1.5 m distance from the heater borehole. From each borehole, four samples were investigated. The measurement procedures for the determination of resistivity and water content were the same as described above.

The resistivities measured on the post-dismantling samples were not significantly different from those measured on samples obtained before heating. The water content was even slightly higher, which might be explained by the different storage time before the measurements (the pre-heating samples had not been tested directly after drilling, but had been taken to the GRS laboratory first, while the post-heating samples were tested on site). In particular, no desaturation of the clay rock during heating was detectable from these investigations, which confirms the results of the geoelectric in-situ measurements.

3.4 Gas and water sampling and analyses

For gas and water sampling, four vertical boreholes were drilled with a diameter of 86 mm, a length of 7.0 m, and distances to the heater borehole between 0.50 and 3.64 m. The locations of boreholes BHE-10 to BHE-13 are shown in Figure 3.8 (p. 17). They were sealed with special packer systems as shown in Figure 3.13. Via three capillaries running from a valve panel in the open gallery through the packer into the residual volume of the boreholes, gas and water samples could be collected.

3.4.1 Gas release measurements

The gas was extracted from the residual volume of the four boreholes by a manual pump and transferred to gas bags. These bags were sent to the GRS laboratory for analysis. In July 2003, a portable gas chromatograph was installed in the test field for on-site analysis. The advantage of this method is that analyses can be performed immediately after extraction and only a small amount of gas is needed. The influence of sampling is therefore minimized.

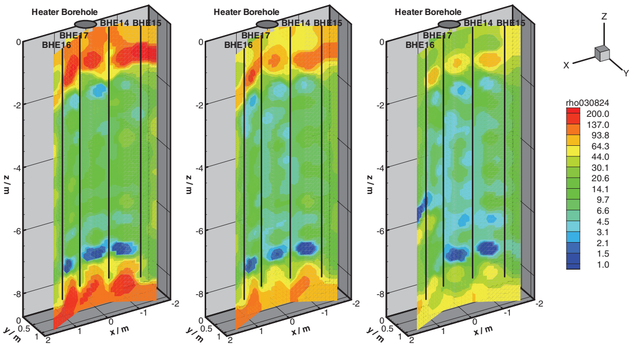

Figure 3.12: Resistivity tomograms obtained on January 1, 2002 (prior to heating - left), on April 1, 2002 (during heating - centre), and on August 24, 2003 (end of heating - right).

The boreholes were drilled and sealed in May 1999. For the first sampling immediately after sealing, the residual volumes were filled with mine air (about 80% N_2, 20 % O_2, 1% Ar and 400 to 500 vpm

CO_2). Gas sampling and analysis started in February 2000, around two years before switching on the heater in February 2002. The results of the gas compositions in borehole BHE-10, which is closest to the heater, are shown in Figure 3.14 and Figure 3.15. At mine temperature (about 14 °C) prior to heating, already carbon dioxide, some helium, and hydrocarbons are released from the Opalinus Clay. As a result of oxidation of organic material in the clay, the concentration of oxygen decreases from 20% to a few percent. The concentration of the gas components varies significantly up to a factor of 15 among different boreholes (e.g. BHE-10 and BHE-11). This indicates that the Opalinus Clay - which seems to be homogeneous macroscopically - is heterogeneous with regard to gas release.

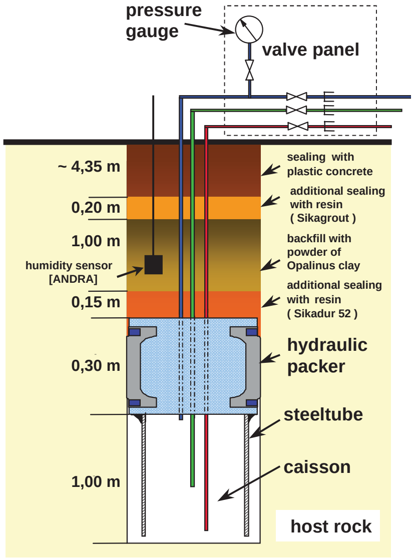

Figure 3.13: Installation of the boreholes BHE-10 to BHE-13: Packer with caisson for taking gas and water samples.

Gas release versus time is shown in Figure 3.16. A significant influence of the heating was seen only in the borehole closest to the heater (BHE-10 with a distance of about 0.5 m). The concentration of carbon dioxide increased from 814 vpm (ml/m^3) in February 2002 to 36000 vpm (3.6 vol.-%) in February 2003. The hydrocarbons (CH_4, C_2H_6, C_3H_8, C_4H_{10}) increased from 234 to 3303 vpm, and helium from 21 to 114 vpm. Hydrogen sulphide (H_2S) was generated after heating began. It was found in borehole BHE-10 in concentrations of up to 680 vpm, while in the other boreholes it was less than 12 vpm.

Hydrogen sulphide is important for the disposal of radioactive waste because, even at low concentrations, it leads to corrosion of the waste and the waste container if it occurs in combination with water and oxygen in the liquid or gaseous phase.

The gas release from the host rock did not lead to a significant pressure increase in the residual volumes of the boreholes. Furthermore, the concentration of carbon dioxide, helium, and the hydrocarbons decreased slightly and oxygen increased in the time period from February to September 2003. Obviously, the host rock is not gas-tight. On the other hand, the laboratory investigations indicated that gas release from the Opalinus Clay is a very slow process and therefore sampling more often than three to four times a year reduces the gas concentration in the system.

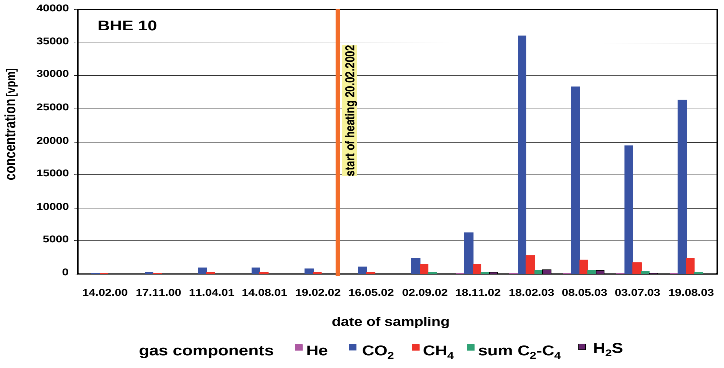

Figure 3.14: Concentrations of gas components in borehole BHE-10.

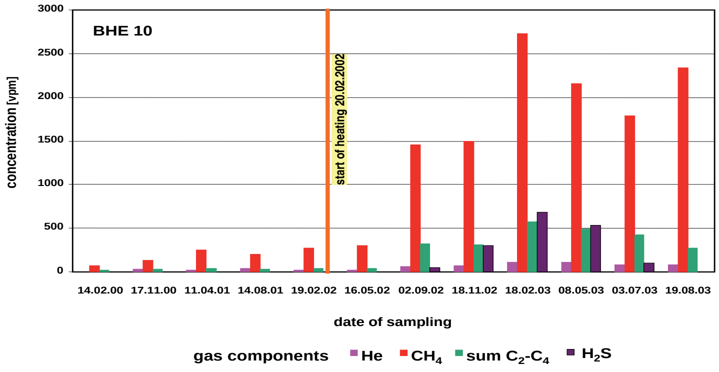

Figure 3.15: Concentrations of gas components without CO_2 in borehole BHE-10.

For comparison purposes, and for testing the analytical system, additional gas samples were taken from the mine air in the HE niche. These measurements indicated that even the mine air has an increased concentration of helium (20 vpm) and carbon dioxide (800 vpm) as a result of gas release from the open surfaces of the host rock.

The measurements on site with the portable gas chromatograph system and samples transferred in gas bags to the GRS laboratory in Braunschweig for analysis did not show significant differences. The advantage of the portable gas chromatograph with in-situ analysis is that the whole system is less disturbed as only a small amount of gas is needed. Furthermore, artefacts caused by sampling and transporting the gas bags to the laboratory are excluded.

The absolute humidity in the residual volumes of the boreholes varies in the range between 7.9 and 13.5 gram water per m^3 air, which is influenced mainly by the temperature in the HE niche. The niche temperature is influenced by the season and the intensity of ventilation.

3.4.2 Water analysis

After gas sampling in August and October 2003, the water in the boreholes was extracted and transferred into sampling bags without coming into contact with the mine atmosphere. The amounts are shown in Table 3.1. This water was sent for chemical analysis to CIEMAT in Madrid. At the CIEMAT laboratory (Pore Water Laboratory), the bags were placed in an anoxic glove box for measuring pH, Eh, and electrical conductivity. Other water aliquots were acidified, depending on the type of chemical analysis required, and the chemistry of the water was then analysed outside the anoxic chamber. The total alkalinity of the samples (expressed as mg/L of HCO_3^-) was determined by potentiometric titration using a Metrohm 682 titrator. The major cations were analysed by Inductively Coupled Plasma-Atomic Emission Spectrometry (ICP-AES) in a Perkin-Elmer Elan 5000 spectrometer. Sodium and potassium were determined by flame atomic emission spectrometry, AAS-Flame, in a Perkin Elmer 2280 spectrometer and trace elements were determined by ICP-MS (Finningan Mat SOLA). Anions were analysed by ion chromatography (Dionex DX-4500i). The silica was detected using a UV-Vis spectrophotometer by means of the silico-molybdic colourimetric method. It was estimated that the maximum analytical errors were ± 10% for the major ions.

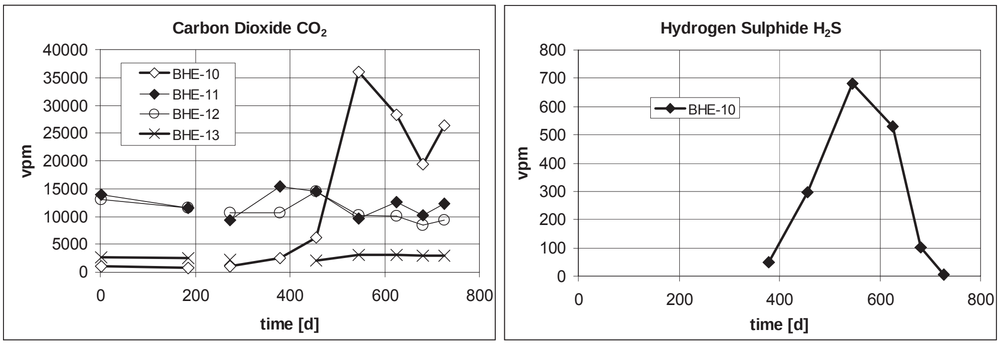

Figure 3.16: **Time dependent development of the concentrations of carbon dioxide and hydrogen sulphide in the vicinity of the heater. The heating started at about day 200.**

Table 3.1: **Amounts of water extracted from the gas sampling boreholes.**

Borehole	Amount of water extracted in August 2003 [ml]	Amount of water extracted in October 2003 [ml]
BHE-10	2231	0
BHE-11	658	0l
BHE-12	1160	213
BHE-13	335	139

Based on the chloride concentration, a dilution of the rock water composition is observed in the BHE-10 borehole. This can also be observed in the concentration of sulphate and cations. However, an increase in bicarbonate is observed in this borehole (BHE-10), which seems to indicate water movement from the bentonite, during the saturation phase, towards the formation and dissolution of the carbonate phases of the Opalinus Clay or the bentonite. Due to this process, some exchange reactions could be occurring, increasing the Na content in the rock water and decreasing the Ca and Mg contents. On the other hand, the bentonite could have adsorbed some ions of the rock pore-water during its saturation. The bentonite was not saturated at the end of the experiment, so the rock water in the BHE-10 borehole did not recover.

Based on the chloride contents (see Figure 3.17 and Figure 3.18), a salinity increase is observed in the rock (cf. boreholes BHE-11, -12, and -13) as a function of time and the distance to the BHE-0 borehole, i.e. there is an increase in salinity towards the BHE-13 borehole. This salinity increase is more accentuated in the second sampling campaign, for which the values are higher than the concentrations obtained in the pore-water samples of the BWS-A1 borehole (Figure 3.18), and similar to the highest values for chloride found in the Opalinus Clay at the contact to the Jurassic marl formation.

There is an increase in sulphate in all boreholes except BHE-10, which indicates a slight oxidation of the rock. This is in agreement with the Eh measured in the waters (see Table 3.2, where SHE values are not shown), whose values are oxidized. This does not correspond with the reducing conditions of the Opalinus Clay system. Thus, as concluded above (section 3.4.1), the rock is not completely gas-tight. On the other hand, the rock-water system in the boreholes was oxidized at the initial conditions of the heating test. Hence, heating may have perturbed the system and caused the oxidation of the rock. However, the reducing conditions appear not to have recovered over time.

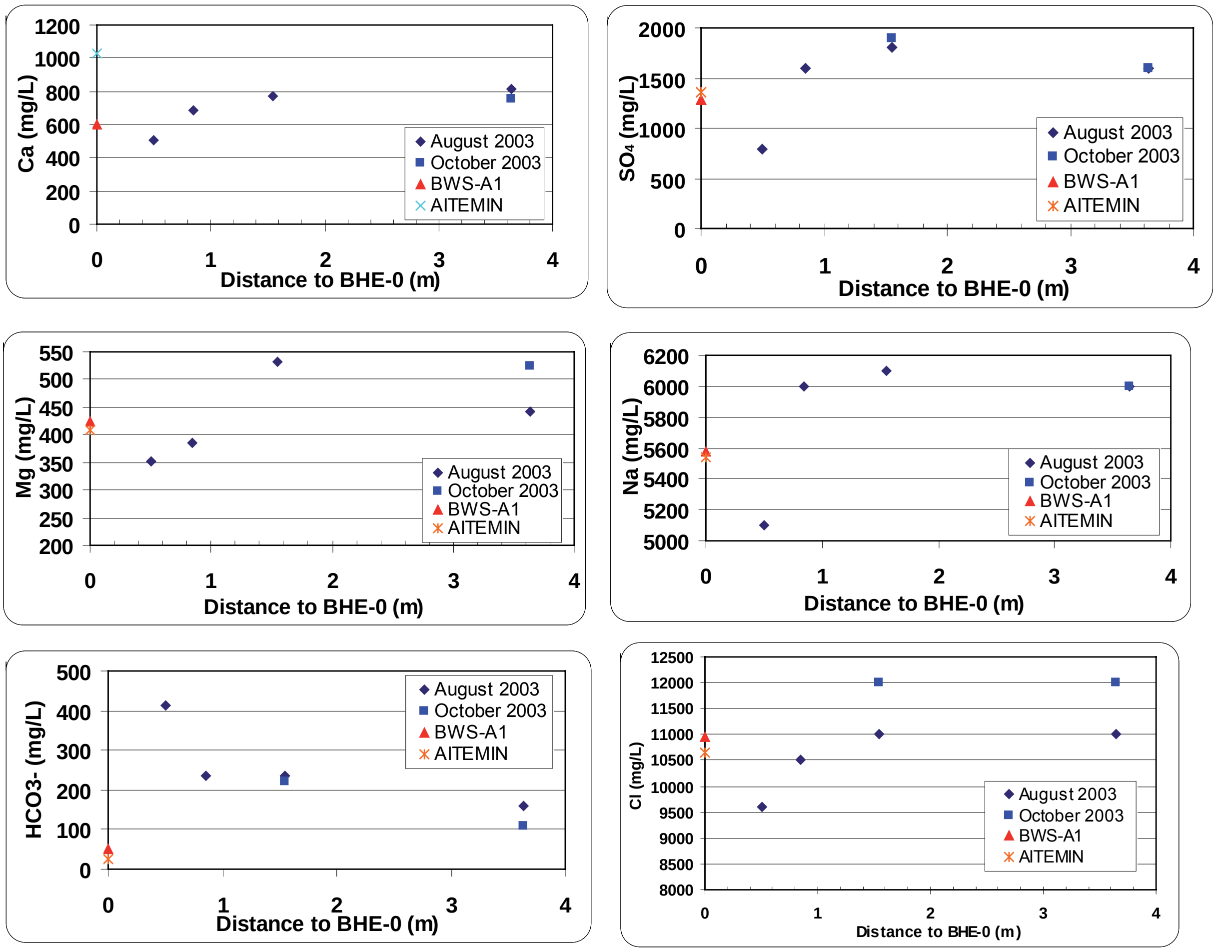

Figure 3.17: Ion Concentration in the boreholes BHE-10, -11, -12 and -13 in comparison to the A1-type synthetic water injected by AITEMIN and the water of the BWS-A1 borehole.

Table 3.2: Chemical composition of the rock waters in the HE test field at Mont Terri URL.

Parameters	Borehole BHE-10	Borehole BHE-11	Borehole BHE-12	Borehole BHE-13	Borehole BHE-12	Borehole BHE-13	BWS-A1 seep water	BWS-A1 squeezed water
Date	August 2003				October 2003			
pH	7.04	7.9	7.16	7.2	7.4	6.9	8.67	7.48
Eh (mV)	-66.3	--	-76.5	-87.7	--	65.6	-88 (SHE)	--
Cond. (mS/cm)	23.1	25.6	27.3	27.6	28.2	27.3	--	--
Cl$^-$ (mg/L)	9600	10500	11000	11000	12000	12000	10958	10300
SO_4^{2-} (mg/L)	790	1600	1800	1600	1900	1600	1280	2120
HCO_3^- (mg/L)	414	234	236	158	221	107	52.0	41-113
Br$^-$ (mg/L)	21	15	26	26	27	26	33.0	33.1
F$^-$ (mg/L)	0.45	0.68	0.48	0.73	0.65	0.63	0.59	--
I$^-$ (mg/L)	2.2	2.3	2.7	2.9	2.7	2.6	2.16	--
NH_4^+ (mg/L)	12	14	13	13	14	13	1.1	--
SiO_2 (mg/L)	15.5	10	10.2	7.5	--	7.7	27.8	--
Ca (mg/L)	505	685	775	811	--	757	600	793
Mg (mg/L)	352	385	533	441	--	525	424	537.8
Na (mg/L)	5100	6000	6100	6000	--	6000	5575	5650
K (mg/L)	75	75	82	81	--	79	42.8	34.7
Mn (mg/L)	0.10	0.21	0.2	0.24	--	0.2	0.025	0.27
Al (mg/L)	0.1	0.08	0.11	0.1	--	0.05		0.357
Fe (mg/L)	0.262	--	2.3	1.1	--	< 0.05	--	0.74
Fe^{2+} (µg/L)	0.262	--	2.3	1.1	--	< 0.05	--	--
Sr (mg/L)	26	31	37	41	--	35	35.0	51.7

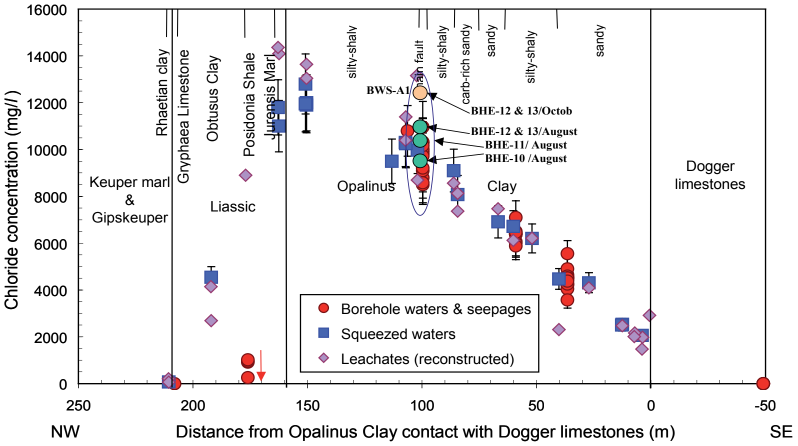

Figure 3.18: NW-SE cross-section of chloride concentration in Opalinus Clay pore waters according to PEARSON et al. (2003), and comparison with the data obtained in the HE experiment.

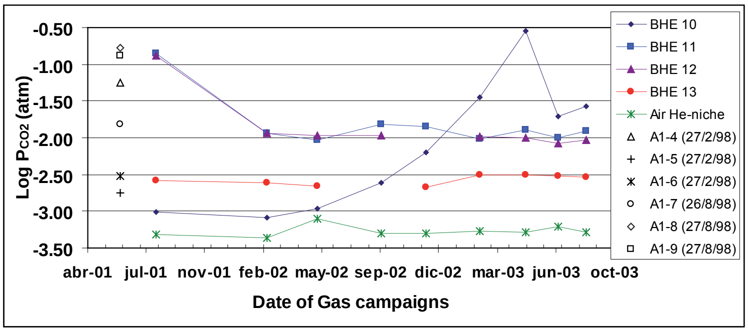

Figure 3.19: Evolution of the partial pressure of CO_2 (atm) in the boreholes BHE-10 to BHE-13. Data are compared with the chemical composition of headspace gas (A1-x samples) in the packed-off interval of the borehole BWS-A1 (PEARSON et al. 2003).

Regarding the CO_2 content, which is a key parameter of the rock water composition, the partial pressure of CO_2 is always higher than that of air (Figure 3.19). The average amount of Log P_{CO2} is –2.09 atm. Regarding the Log P_{CO2} value, the BHE-11 and BHE-12 boreholes show similar behaviour, with an average value of –1.83 atm. The BHE-13 borehole has an average value of –2.57 atm. However, the BHE-10 borehole, close to the bentonite buffer, behaves differently. It seems that there is a significant influence of heating, which is only seen in this BHE-10 borehole. The minimum value of Log P_{CO2} is –3.09 atm, and the maximum value is –0.55 atm, with a final average value of –1.65 atm. All these data are in the range of values measured in other experiments in the Opalinus Clay (PEARSON et al. 2003).

4. Dismantling

4.1 Dismantling operations

4.1.1 Objectives and sequence of dismantling operations

The basic objectives of the HE project dismantling operation can be summarised as follows:

1. Analysis of the THM behaviour of the bentonite buffer and surrounding rock, in order to determine the state of the bentonite after the hydration and heating phases and the degree of rock “damage” due to the heating and the bentonite swelling pressure.
2. Analysis of those aspects which require visual inspection (cracking, sealing of buffer gaps, fractures, cabling, etc.), particularly the sand at the bentonite-rock contact and the performance of the steel tubes.
3. Analysis of the behaviour and failure mode of the different installed instruments.
4. Analysis of the performance of the engineered materials (corrosion of metals, degradation of plastics, behaviour of the resin plug, etc.).
5. Performance of an intensive sampling programme of test components (bentonite, rock, metals, instruments, etc.).

The dismantling operation was carried out in the following sequences:

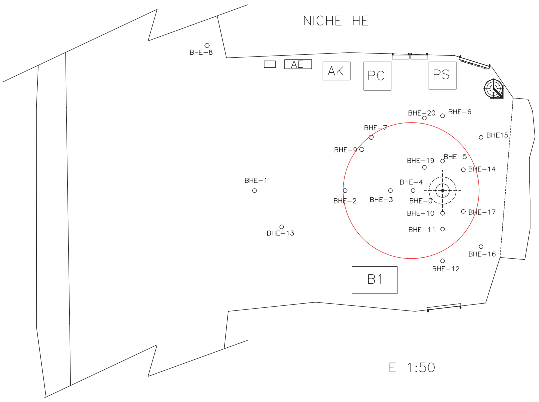

Figure 4.1: Positioning of the shaft.

1. Cooling period
2. Partial removal of equipment and Data Acquisition System (DAS) rearrangement[*]
3. Borehole drilling (5 boreholes) and sampling (about 28 to 30 samples)[1]
4. Borehole measurements (hydraulic pulse tests, seismic, dilatometer and caliper measurements and video inspection)[*]
5. Preparatory works
6. Dismantling, mapping, and sampling operation
7. Removal of DAS
8. Niche conditioning

The sequence of activities, including the sampling during the dismantling operation, is shown in the time-table in Table 4.1.

---

[*] Items 2 to 4 were performed during the cooling period.

4.1.2 Cooling and DAS rearrangement

The heater was powered down by remote control from AITEMIN headquarters in Madrid on 1 September, 2003. The heater was extracted from the heater tube of borehole BHE-0 on 2 September, 2003. Dismantling started with a cooling period allowing the temperature in rock and bentonite blocks to reach tolerable levels, making their handling more feasible (see section 2.3.4). The DAS (Data Acquisition System) cabinets were moved to a different position and covered with plastic sheets to protect them from possible damage during the dismantling operations. Finally, all failed sensors were disconnected from the DAS as they were no longer recording valid data.

4.1.3 Borehole drilling, measurements, and sampling

The aim of the borehole measurements was to determine and evaluate the "in situ" geomechanical and hydraulic state of the rock-mass surrounding the heater and the identification of changes in rock properties induced by the experiment. Immediately after switching-off the heater, 5 boreholes (BHE-23 to BHE-27) were drilled in the vicinity of the heater borehole, at distances between 350 and 1500 mm. The drillcores were used for the post-heating geoelectric, gas content and water release, rock mechanical, and mineralogical laboratory tests. The seismic, hydraulic, and geotechnical in situ measurements were performed as planned prior to the dismantling operation. The borehole measurements comprised velocity measurements and video inspection (see section 6.8), dilatometer tests and caliper measurements (see section 6.5) and hydraulic pulse tests (see section 6.9). The combination of seismic, geotechnical, and hydraulic measurements provided a detailed description of the state of the host rock after heating and of the degree of rock damage.

Table 4.1: Chronology of the dismantling operation.

Activity	Date
Partial relocation of equipment and reconditioning of DAS	1-3 September 2003
Excavation phase 1	20-24 October 2003
Sampling phase 1	
Excavation phase 2	27-31 October 2003
Sampling phase 2	
Excavation phase 3	1-7 November 2003
Sampling phase 3	
Excavation phase 4	17-21 November 2003
Sampling phase 4	
Excavation phases 5 to 7	8-18 December 2003
Sampling phases 5 to 7	
Dismantling of DAS	21-23 January 2004

4.1.4 Preparatory work

This task consisted of all the preparatory work and service installations (power, water, ventilation, etc.) required to perform the dismantling operation.

Figure 4.2: **General view of the excavation work (phase 1).**

4.1.5 Dismantling method

The dismantling method used was to excavate a vertical shaft in the niche floor around the heater borehole (Figure 4.1) and perform the dismantling and sampling from the inside. The shaft was excavated using a drilling hammer on the niche floor in the first phase (Figure 4.2) and a smaller drilling hammer machine inside the shaft in the later phases. The shaft has a circular cross-section with a diameter of about 3 m and a final depth of 7 m. The excavation was done in seven phases of one meter depth each. At the end of each drilling phase, the installed sensors were recovered and the sampling programme was carried out as planned.

To ensure safe working conditions inside the shaft, after the excavation of each depth meter, the complete perimeter of the shaft was reinforced with a metallic mesh and the upper section of the rock wall was secured with shotcrete.

The most important conclusions from the dismantling operation are:

- The resin and cement plug installed on top of the central borehole BHE-0 was found to be intact, homogeneous and free of cracks. It functioned correctly during the whole experiment.
- Most of the sensors in the central borehole were recovered as planned. A significant number of sensors in the peripheral boreholes was also recovered, although some were quite damaged by the excavation operation.
- Cables and injection tubes were in perfect condition along their entire length, passing through the plug and the sand installed on top. The failure of thermocouples at the beginning of the experiment was not a result of a failure of the cables (for details, see section 4.3.2.1 on p. 32).
- Signs of corrosion are evident in metallic parts not made from stainless steel, although it is generally a superficial corrosion in staples, liner, heater tube, and some of the cables (Figure 4.3). Most of the sensors were quite resistant to corrosion (effects are slight and superficial), except for piezometers installed in borehole BHE-5. Nevertheless, serious damage due to chemical attack were found in the total pressure cells of BHE-0.

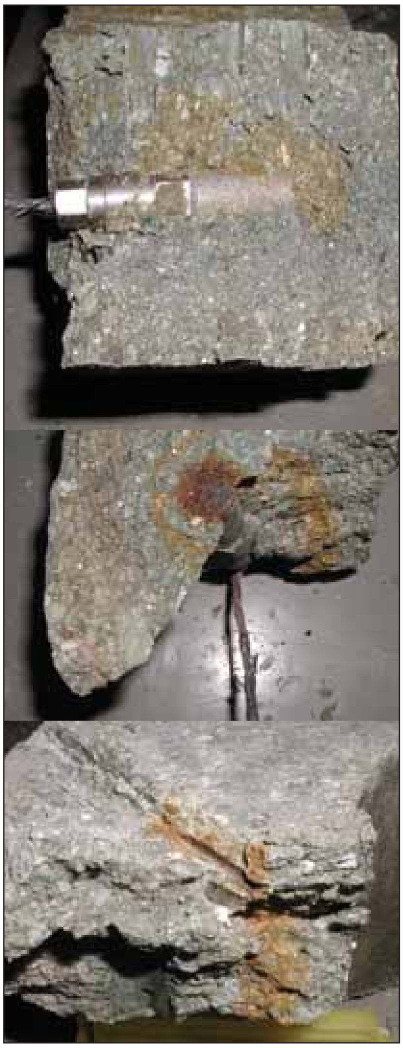

Figure 4.3: **Details of corrosion of sensors in a bentonite block.**

- The coupling of the two sections of the heater tube showed a mechanical failure in the screw coupling and this was the main cause of water entering the tube at the beginning of the heating phase. The welded seam in the base of the tube also failed, but it seems unlikely that water entered at this point because the resin plug had previously been applied.
- The filling sand was found to be quite clean, not very compacted (probably as a result of the decompression caused by the excavation) and humid. A gap of about 1 cm, completely filled with sand, was found between the bentonite buffer and the rock.
- The bentonite blocks did not show evidence of deformation, apart from that caused by the local swelling as a consequence of the excavation itself. There are no noticeable mechanical effects on the instrumentation that might have been caused by the swelling of the bentonite.
- The components of the hydration system, such as ceramic filters, geotextile mat and polyamide tubes, indicate that pressure was exerted by the bentonite (e.g. fracturing of ceramic parts), but they did not lose their integrity.

4.2 Structural and geological mapping of the HE shaft

Geological mapping of the walls was carried out during the excavation of the shaft. The structural map of tectonic faults and EDZ (Excavation Disturbed Zone) fractures in the shaft is compared to the mapping of twenty-one drillcores of boreholes in the vicinity of the shaft.

4.2.1 Geology of the Mont Terri Rock Laboratory

The Mont Terri Rock Laboratory is situated in the southern limb of the Mont Terri anticline located in the Jura fold and thrust belt (Figure 4.4). The Mont Terri anticline is the north-westernmost of the Jura Mountains and is the result of the ramping and thrusting of the Folded Jura over the Tabular Jura. The tectonic style of the Jura Mountains is controlled by two end-members of fault-related folds, i.e. fault-bend folds and fault-propagation folds, which result in distinct fold-thrust (ramp) interactions. The rock laboratory lies in the Opalinus Clay formation (lower Dogger, Aalenian). The Opalinus Clay formation can be divided into three subfacies (Thury & Bossart 1999):

i. shaly facies
ii. sandy facies and
iii. carbonate-rich sandy facies.

The geological site map is shown in Figure 4.5. The HE niche is located in the shaly facies of the Opalinus Clay formation. The shaft was excavated below the Main Fault, which is an important thrust zone at the laboratory scale. The distance between the Main Fault and the shaft is about 6 meters.

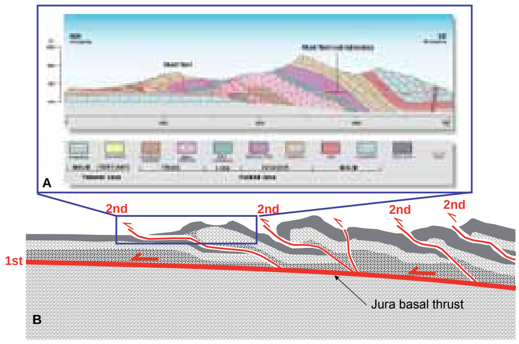

Figure 4.4: A) Cross-section through the Mont Terri anticline showing the location of the Mont Terri rock laboratory in the southern limb (FREIVOGEL & HUGGENBERGER 2003). B) Large-scale cross-section.

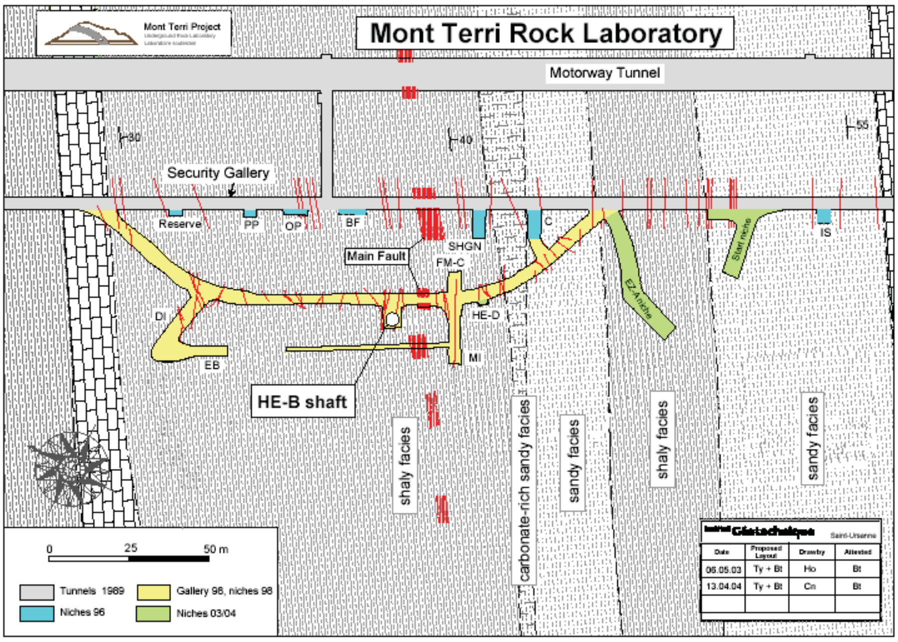

Figure 4.5: **Mont Terri Rock Laboratory site map showing the location of the HE niche and shaft.**

4.2.2 Shaft map

The geometry of the shaft can be treated as an open vertical cylinder of 7 m depth with a diameter of 3 m in the upper part (from 0 to 5 m) and 2 m in the lower part (from 5 to 7 m). The structural map (Figure 4.6 on p. 29) is the result of the mapping of the shaft walls restored from the internal side of a cylinder (3D) into a rectangle (2D). The mapping of the shaft walls reveals the traces of many thrust faults in the upper part of the shaft between the surface (floor of the HE niche) and 2.5 m depth. In fact, between 0 and 2.5 m the shaft intersects a fault network whose boundaries (orientation and plunge) are sub-parallel to the bedding planes (Figure 4.7). Kinematics of the fault planes, deduced from the systematic analysis of slickensides (calcite fibers, striae, Figure 4.8) on the fault planes, show that the fault network is a thrust zone with many imbrications. The geometry of slickensides gives the shear sense that was applied on the fault plane. The deformation is locally intense and led to the folding of strata restricted by the rock mass between two close thrust planes (see between faults h and I in the left part of Figure 4.6). Generally, fault planes plunge towards the SE (azimuth range of 130° to 160°) with a dip angle between 30° and 35°. Fault planes with steeper plunges (> 35°) act as ramps to transfer the shortening from a lower stratigraphic level towards an upper stratigraphic level. In this way, they connect the different thrust plane levels with each other. The resulting structural pattern corresponds to the so-called “flat-ramp geometry”. The detailed structural analysis of the overlying Main Fault led to similar observations (Nussbaum et al. 2001). Some discrete fault planes were identified below the thrust zone between 2.5 m and 4 m. The lower part of the shaft between 4 m and 7 m depth seems to have been less affected by the deformation, since no obvious markers of deformation (except of one fault at about 5 m depth) could be recognized. In this area, the main structural element is the bedding plane whose orientation and dip display homogeneity (Figure 4.9). The azimuth range lies between 140° and 155° and the scattering of the dip angle is very restricted (between 32° and 35°).

In conclusion, the geological structures intersected by the shaft reflect, on the meso-scale, the geometry of the Folded Jura on a larger scale. The tectonic pattern within the shaft exhibits inhomogeneously distributed structures. The structural pattern of the shaft can be divided into two parts:

- The upper part from 0 to -2.5 m, strongly deformed, transected by a complex thrust zone with many imbrications (two sets of fault with the same orientation - range of 130° to 160° - but two different plunges of 30° - 35° and 50°).
- The lower part from 2.5 and 7 m, weakly deformed, affected by only two fault planes (noted as q and r on the map). As these fault planes are parallel to the bedding, the resulting anisotropy is uniform in the lower part (azimuth: 140° - 155°; dip: 30° - 35°). The only difference is in the lateral continuity of the discontinuities. The fault planes extend over large areas, while bedding planes developed along discrete planes.

Besides the tectonic fractures, few true EDZ fractures could be identified. Most of them are due to the mechanical reactivation (slip) of bedding planes or of sub-parallel fault planes. The reactivation of these planes increases the anisotropic pattern of the rock mass.

4.2.3 Correlation with drillcores in the vicinity

The structural pattern displayed on the shaft walls is in full agreement with the structural mapping of drillcores in the vicinity of the shaft.

4.2.4 Conclusions

There is a network composed of imbricated faults located between 0 and 3 m depth and artificial fractures that developed below the floor of the HE niche. This combination of tectonic and EDZ fractures increases the fracture density in the upper part of the shaft significantly. The geoelectric monitoring (section 3.3) accordingly shows increased electric resistivity in the upper part of the shaft between 0 and 3 m.

The well-developed bedding in the Opalinus Clay leads to an anisotropy pattern which is accentuated by the occurrence of a fault system sub-parallel to the bedding. This fault system is responsible for the folding of the Mont Terri anticline. The rock mass displays orthorhombic symmetry with different properties in the bedding plane and normal to the bedding plane along the strike as well as normal to the strike direction.

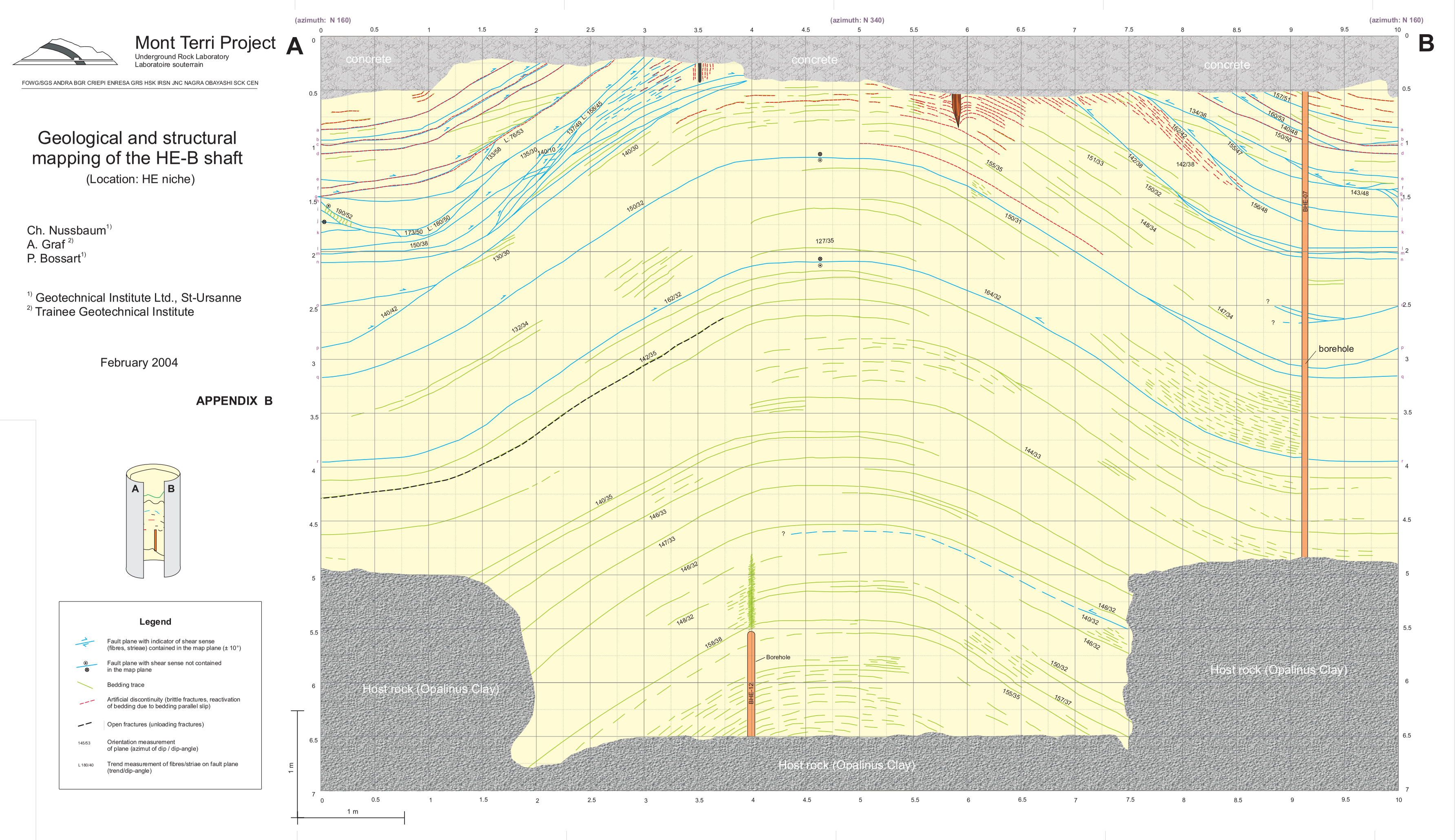

Figure 4.6: Shaft map.

Figure 4.7: View towards the thrust zone between 0 and 2.5 m depth (view towards the rear end of the HE niche). A grid was installed for precise mapping. Right: the central heater borehole containing the heater casing.

Figure 4.8: Slickensides on a fault plane (broken block). Shear sense is consistent with a thrust movement. The upper part (hanging wall) is ramped above the lower part.

Table 4.2: Total sensors recovered.

Type of sensor	Total
Thermocouple	22
Total Pressure Cell	11
Pore Pressure	11
Relative Humidity	6
Inclinometer	4
Piezometer	3
Total	57

Figure 4.9: Photo taken at a depth of 6 m. The well-developed bedding leads to a strong anisotropy. side square length is 0.5 m.

4.3 Instrumentation analysis

4.3.1 Retrieved sensors and analysis method

Table 4.2 shows the total list of sensors recovered during the dismantling operation, grouped by type of sensor. Although the number of sensors recovered during dismantling was smaller than initially planned (some sensors were lost and others were not dismantled due to the reduction of the excavated section from a depth of 6 m downwards), and despite the poor condition some of them were in as a result of the excavation work, laboratory analysis of sensors was possible as planned. The analysis performed for each type of sensor was:

- Checking the measurement accuracy of sensors that are still operational, and
- More detailed analysis of damage, particularly for failed sensors.

4.3.2 Results of the analysis

4.3.2.1 Temperature sensors (thermocouples)

Type T thermocouples were used in boreholes BHE-0 to BHE-6. Most of the sensors installed in the central borehole BHE-0 failed prematurely after the initial manual hydration of the sand. In some cases, after the failure water passed along the cable and reached the electronics installed at the surface. A later analysis of the cable protection, made of Teflon, showed that it was not continuous and therefore did not ensure that the cables were watertight. On the other hand, most of the thermocouples installed in the peripheral boreholes remained operational during the duration of the experiment. The corrosion found in some of the metallic parts of the thermocouples (inside which the junction is located) is only superficial. The cables were neither externally altered nor damaged, but they were less flexible than at the time of installation - probably due to the effects of bentonite and temperature. All thermocouples installed in BHE-0 showed some kind of corrosion in the inner part as a result of a chemical reaction such as e. g. oxidation. The metallic sheet appeared corroded, the plastic components damaged, or the internal juncture was also corroded. The accuracy of all thermocouples that were still operational is similar to the accuracy at the start of the experiment.

According to the results of the analysis, it can be concluded that the water injected by the continuous hydration system entered the thermocouples of borehole BHE-0 through the external jacket and first came into direct contact with the cable conductors. The reason was that the cable protection made of Teflon was not continuous but coiled around the cables and hence could not ensure water-tightness. This fabrication defect was detected after the sensors had been installed in BHE-0, i.e. when they started to fail. The high-salinity water may then have entered the thermocouple's metal body via the resin protection of the thermocouple junction. It is not clear if there was a defect in the sealing, or if the material suffered a chemical attack. Probably, the corrosion process took place in the central borehole BHE-0 only, as it was the only place where free water was available.

4.3.2.2 Pore pressure sensors

All the pore pressure sensors installed in the central borehole BHE-0 were in direct contact with the bentonite buffer. Almost all sensors failed during the experiment and water was frequently found in the cable protection jacket, which reached the surface electronics. The functional verification made for these sensors confirmed that none of them were operational. The rust found in the metallic parts of the sensors was superficial, except for one that suffered some chemical attack which damaged it seriously (see Figure 4.10).

Figure 4.10: Effects of corrosion in a pore pressure sensor.

In general, the porous filter placed in the sensor head resisted the experimental conditions. Most of the sensors and cables were in good condition, while the sensors installed in the vicinity of the heater showed evidence of chemical attack, probably strengthened by the effect of temperature. The most damaged part of the cable was near the gland, which probably debilitated the cable and made it more vulnerable to chemical attack. Signs of rust appeared in almost all sensors analysed, as well in the metallic shield in the inner part of the cable. This proves the presence of water even in sensors with cables that are apparently in perfect condition. There were also traces of bentonite and humidity under the O-ring of the cable gland, which indicates the entrance of water in the body of the sensor through this gland.

According to the results obtained, the most probable cause of failure of this type of sensors was water entering the inner part of the measuring head, which may have damaged the electronics. The water could have entered through the cable gland or through the cable itself in the case where the Teflon jacket was defective.

4.3.2.3 Relative humidity sensors

The relative humidity sensors used were of the capacitive type. All sensors installed in borehole BHE-0 failed gradually during the experiment. In some cases, water drainage was detected along the cables, reaching the surface electronics. On the other hand, relative humidity sensors installed in peripheral boreholes remained operational during the whole experiment.

Due to the dismantling work, the cabling of the sensors had to be disconnected from its electronic card or cut. When reconnecting it for verification, the initial calibration was inevitably lost, but their operability could be checked. The verification showed that 100 % of the dismantled sensors were operational.

From the mechanical point of view, the state of the sensors was acceptable. No damage as a consequence of the dismantling operation was detected, apart from cuts in the external cable jacket of some sensors. All of the metallic parts show minor signs of surface corrosion, except in the connector to the cable where corrosion was more pronounced. There were no signs of corrosion in the inner part of the filter or in the measuring sensor.

Free water was found inside the bodies of all the sensors installed in the bentonite buffer. This water had a high salinity (20 g/l Cl), was very acid (pH = 1.3) and contained high concentrations of Cu, Cr, Fe, Mn, Zn, and Pb, probably coming from the sensors themselves.

According to the results obtained, the water entered the sensor through the cable gland (Figure 4.11) and, once it was inside, it moved upwards to the surface through the internal wires, corroding the protective metallic shield. The measuring element seems to remain unaffected, as it was protected from the water by a resin seal that was very efficient.

Figure 4.11: Corrosion in the metallic cable gland of a relative-humidity sensor.

4.3.2.4 Total pressure sensors

The installed pressure cells were based on a solid-state silicon pressure transducer (4 active semiconductor strain gauges) coupled to a fluid-filled diaphragm. Nearly all of the total pressure cells installed in the central borehole BHE-0 failed soon after the initial manual hydration of the sand. Therefore, and previous to the installation of the pressure cells in the peripheral boreholes, these cells were analysed, and a defect in the construction of the cable entry was found, which meant that they were not watertight. The remaining cells were sent back to the manufacturer (KULITE) for repair before they were installed. The total pressure cells installed in the peripheral boreholes had a much smaller rate of failure.

The total pressure cells retrieved from the central borehole BHE-0 were quite damaged (Figure 4.13). Only two of the five sensors examined reacted to an increase in the applied pressure. They had been installed at higher depths. The corrosion detected in the metallic parts was slight, although there were clear signs of chemical attack, probably caused by sulphates. Water was detected in the inner part of the sensors, although the measuring membrane was in perfect condition in all cases. The cable gland was corroded in all cases, as well as the cable's protective metal jackets.

Figure 4.12: Details of a piezometer installed in borehole BHE-5.

The total pressure cells installed in the peripheral boreholes had an additional protection of the cable entry in the form of a thermo-retractile cover filled with epoxy resin. The external corrosion of these sensors was also smaller. Four of the six cells tested reacted to a pressure increase. The remaining two had mechanical damage caused by the dismantling operation.

As a conclusion, the common cause of failure of the total pressure cells was the penetration of water to the sensor through the cable gland. This water damaged the electronics of the sensor, in some cases irreversibly.

4.3.2.5 Piezometers from borehole BHE-05

The piezometers are pore pressure sensors specially designed for measurements in low-permeability rocks such as Opalinus Clay. They have a small measurement chamber in the shape of the borehole (diameter 86 mm) and are connected to the wall by a hydraulic jack. Two metal tubes that connect the chamber with the outside have a metal mesh for protection and a Teflon filter.

The piezometers were very slow in detecting thermal effects during the experiment. The sensors analysed were in very poor condition, showing a general state of corrosion. The parts of the sensors made of carbon steel were totally corroded, while those made of stainless steel 316L did not suffer.

Therefore, the high corrosion found in the sensors was a consequence of the material they were made of. The zinc protection of the carbon steel was not suitable for use in permanent and direct contact with saline water. The remaining elements were in good condition and damage by corrosion does not seem to have caused deficient operation of the sensors.

4.3.2.6 Inclinometers from borehole BHE-07

A chain of very sensitive inclinometers (uniaxial electrolytic tilt sensors) were installed in borehole BHE-7 to monitor the deformation of the rock. Most of the inclinometers remained operational during the experiment. Only four out of the eleven sensors installed were recovered and most of them were in very good condition; any damage was the consequence of the dismantling operation. The sensors worked correctly and the design and installation were optimal for the experimental conditions. Nevertheless, comparison with numerical results (see section 7) raises questions regarding the reliability of results.

Figure 4.13: Corrosion in a total pressure cell.

4.3.3 Conclusions from the analysis of sensors

Many of the sensors installed in the bentonite buffer (BHE-0) were not sufficiently watertight in the presence of saline water. Some sensors, e.g. the thermocouples or the total pressure cells, failed prematurely due to manufacturing defects. On the other hand, pore pressure and relative humidity sensors failed gradually, most probably due to corrosion damage in the cable gland. In contrast, most of the sensors installed in the remaining (peripheral) boreholes maintained operability as the free saline water conditions did not exist in this case. Some manufacturing problems were also solved prior to their installation (in the case of the total pressure cells). According to the results from the sensors installed in borehole BHE-5, manufacturing of all metallic elements from stainless steel with a similar quality to 316L should be considered to avoid corrosion problems in this medium. In conclusion, it is recommended to reinforce the quality controls to which the sensors are subjected after their manufacturing, as well as the controls prior to their installation, even if it means a delay in the implementation of the project.

4.4 Corrosion analysis of the heater tube

The Corrosion and Materials Integrity Department of EMPA Dübendorf was commissioned by NAGRA to investigate the fractured screw coupling (Whitworth thread with Teflon O-ring) of the BHE-0 heater tube made of unalloyed steel for chemical corrosion and metallurgical properties and to assess the causes of the damage.

4.4.1 Findings

After removal of the filter material, the following observations were made on the outside of the BHE-0 heater tube section from 2.85 m to 3.45 m depth:

- The pipes made of unalloyed steel have a coat of organic corrosion protection paint in the region of the screw coupling (35 mm above to 200 mm below). There is no detectable corrosion protection in the other areas.
- In the regions with no corrosion protection, the pipe surfaces are covered by an irregular crust of brown iron corrosion products. The steel surfaces have been extensively attacked by corrosion in the form of pitting. The maximum depth of corrosion is about 0.5 mm.
- In the regions with corrosion protection, the pipe surfaces are similarly covered by crusts of brown iron corrosion products, although only in certain zones. The steel surfaces in these zones are affected by corrosion in the form of pitting. The maximum depth of corrosion is about 0.5 mm.

The following visual observations were made in the region of the screw coupling:

- The screw coupling is fractured at the point on the pipe where the outside thread starts (approximately 5 mm wide groove with wall thickness of about 1.5 mm), Figure 4.15 and Figure 4.14. The fracture runs radially after the last turn of the thread.
- The groove and the surface fracture are covered by an irregular crust of brown iron corrosion products. The steel surface is extensively attacked by corrosion in the form of pitting (Figure 4.15 to Figure 4.17). The maximum depth of corrosion is about 0.2 mm.

4.4.2 Summary of the investigation results

4.4.2.1 Metallographic investigation

For the metallographic investigations, one sample each was taken from the fracture and counter-fracture. The micro-sections were ground in the axial direction (Figure 4.14). The steel has a ferritic/perlitic structure stretched in lines with a slight preponderance of ferritic phase components (Figure 4.17). In terms of structure, the steel can be classified as a general carbon steel. There are


Figure 4.14: Fracture region (inside; after chemical removal of the corrosion products.


Figure 4.15: Fracture region (outside; after chemical removal of corrosion products).

no defects in the steel structure. The pitted corrosion on the surfaces of the pipe sections and on both fracture surfaces can be categorized as secondary (Figure 4.17). The outside thread was cut by machining. Vickers hardness measurements (HV) indicate an average hardness of approximately 245 HV10. This value corresponds to a tensile strength of approximately 780 N/mm^2 and correlates with the high perlite content ascertained in the assessment of the structure.

4.4.2.2 Corrosion-chemical investigation

Using X-ray microanalysis REM/EDX, considerable quantities of silicon and chlorine were detected in the iron corrosion products from the outside of the BHE-0 heater tube, as well as large quantities of iron and oxygen. Significant quantities of corrosion-enhancing chlorides (1.1 weight-%) were determined in the 1:20 aqueous extract of the iron corrosion products which reacts as an acid (pH value 4.5) and has a high electrical conductivity of 1.680 µS/cm.

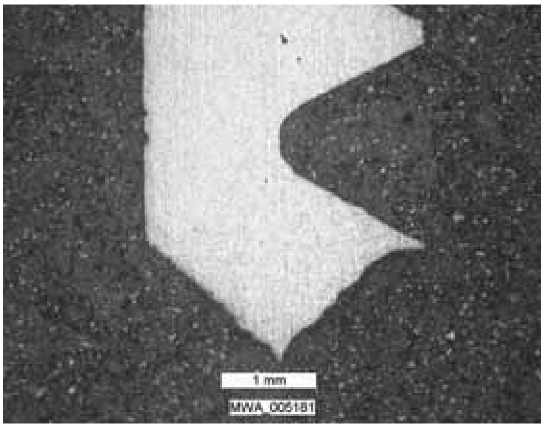

Figure 4.16: Metallographic sample of the screw coupling: overview of the end of the thread and the fracture sureface.

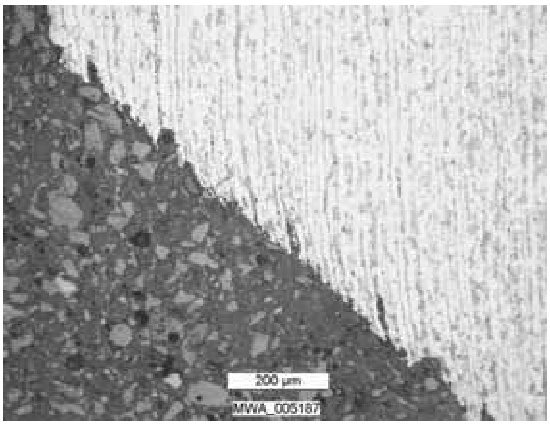

Figure 4.17: Metallographic sample of the screw coupling: ferritic-perlitic steel structure, corrosion on fracture surface (detail from Figure 4.16).

4.4.3 Assessment

The corrosion detectable on the outside of the BHE-0 heater tube is attributable to the effects of moisture/wetness and the presence of corrosion-enhancing chlorides. The maximum depth of the corrosion is generally about 0.5 mm; in the fractured region where the outside thread on the pipe starts it is about 0.2 mm. Since the detected depth of pitting caused by corrosion resulted after an exposure time of at least 4 years, but the leak in the region of the pipe coupling was already detected after only a few months of exposure, there is apparently no causal relation between the corrosion and the leaking of the pipe.

The leak is far more likely to be the result of a purely mechanical fracture (forced failure due to overstressing, assisted by the notch effect of the thread) of the screw coupling at the 5 mm wide groove at the point on the pipe where the outside thread starts. The pipe material does not show any material or structural defects in the fracture area which would have assisted or caused this. The fracture seems to have been a consequence of the reduced thickness of the tube in the area of the screw.

4.5 Corrosion analysis from laboratory experiments

The program of rock mechanic laboratory tests was delayed by two severe (and costly) cases of corrosion: The surfaces of a testing machine made of high-alloy steel were heavily corroded during contact with a Mont Terri Opalinus Clay sample at 50°C and a relative humidity of 90%. During another test, aluminium disks below an Opalinus Clay sample (at natural water content) were corroded. There are different conceivable causes for the corrosive reactions:

Figure 4.18: Corrosion of laboratory equipment exposed to Opalinus Clay samples.

- Pyrite (FeS_2) oxidizes in the presence of air and water. The products of the reaction are Fe-oxy/hydroxides and H_2S. H_2S oxidizes in aqueous solution to sulphurous (H_2SO_3) or sulphuric (H_2SO_4) acid. Both acids corrode high-alloy steel, particularly at high humidity and increased temperature. The pyrite content is less important than the permeability of the rock, because it is a surface reaction. Only at the surface are oxygen and water able to come into contact with the finely dispersed pyrite.

- Chlorine ions Cl^+ present in the porewater of Opalinus Clay are also likely to fuel corrosion of metals, particularly e.g. in austenitic steels.

- Humid clays or suspensions of clay act in combination with an aluminium surface as a catalyst for oxidization. The reaction products are aluminium hydroxide and hydrogen. The amount of water needed for the reaction is a matter of controversy. The same holds for the exact reaction process. The reaction appears in different clay minerals and has been observed in minerals of the Opalinus Clay (NÜESCH 2004).

The mechanisms of metal corrosion by clays are not yet fully understood. Therefore - inspired by the experience in the HE experiment - several studies are underway to provide more knowledge on the topic.

5. Experimental characterization of the engineered barrier: bentonite

Laboratory tests were performed to determine the mechanical, hydraulic, and geochemical characteristics of the buffer to validate model predictions, e.g. of saturation, and to identify variations in the material properties. The main objective of the bentonite sampling and analysis program was the identification of physico-chemical alterations occurring in the clay due to the effects of heat and hydration. The work includes laboratory tests on bentonite block samples taken during the dismantling operation from the heated and non-heated areas in the test field. This chapter provides a description of the buffer dismantling and bentonite sampling operation and the results of the bentonite hydro-mechanical analysis, the bentonite and porewater geochemical analysis and the bentonite mineralogical analysis obtained by in-situ observations during sampling, on-site analysis and laboratory tests.

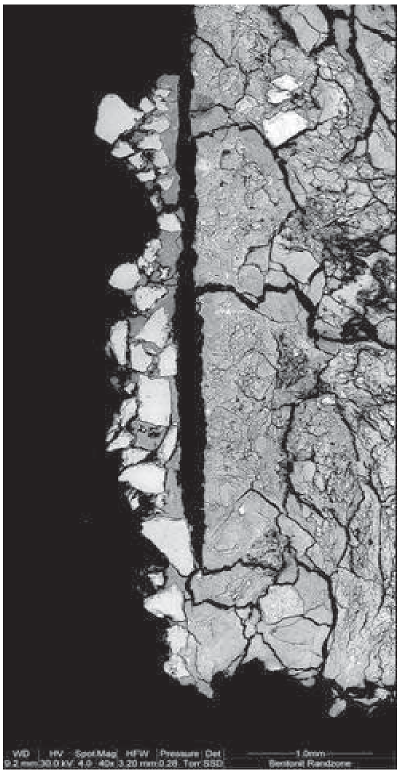

Figure 5.1: Electron microscopy of the interface between the bentonite (dark grey) and the sand (pale grey).

5.1 Bentonite sampling, visual inspection, and geometric considerations

The main experimental area (around borehole BHE-0) was dismantled to obtain the required samples. For the laboratory investigations of bentonite buffer and host rock, samples from the heated and non-heated areas in the test field were taken. Sampling and determination of water content distribution in the buffer material were made on site in direct conjunction with the excavation. The samples for other laboratory measurements were obtained, taking care to ensure a small mechanical influence on the samples and a minimal water loss as a result of handling the specimen in the open air.

During the dismantling operation, a careful visual inspection of macroscopic aspects (rock/bentonite interface, joints between the blocks, etc.) and photo recording of the main components of the experiment (sand, bentonite blocks, heater tube, buffer instruments) was done. Sampling started on top of the buffer with block no 50. In the heater region, the blocks are numbered from 30 to 10. The radial direction is given by degrees where the 0-direction points to the east and the 90-direction to the south (cf. Figure 3.8, p. 17).

The time between the excavation of the Opalinus Clay and the bentonite sampling amounted to a couple of hours. This was long enough for drying of the bentonite buffer, even if it was wrapped in film. As a result, dry cracks can be observed on blocks which were exposed the longest to air (Figure 5.2). A further reason for crack formation is the unloading caused by removing the Opalinus Clay. An oval deformation in the cracking direction of the blocks could be observed.

The radial dimension and the height of the blocks were measured during dismantling to detect volume changes due to hydration/heating. The initial height of the blocks was 100 mm. The five blocks on top show an increase in height: block 50 – 49: 120 mm and block 48 – 46: 105 mm.

Table 5.1: Values of water content w, dry and solid density ρd, ρs, porosity n, degree of saturation Sr and water content at saturation ws for samples from different vertical positions in the middle of the bentonite blocks close to the heater. Sample number code is: block number – position of the sample (m for middle) – radial direction – distance from heater (a for near).

Sample number	Depth [cm]	w [%]	ρ_d [g/cm^3]	ρ_s [g/cm^3]	n	S_r [%]	w_s [%]
41-m-0-b	293	29.4	1.47	2.5736	0.43	101	29.1
30-m-170-b	405	28.8	1.52	2.5796	0.41	106	27.1
22-m-90-b	485	25.4	1.56	2.5887	0.40	99	25.5
10-m-90-b	606	25.9	1.55	2.5885	0.40	100	25.9
1-m-180-b	695	27.9	1.48	2.5760	0.43	96	29.0

The others stay at 100 mm. The conical initial ring width of the blocks was 85.5 - 87.75 mm. The final ring width was measured as 90 - 95 mm. Hence, the swelling potential of the bentonite has not been exhausted (see also section 5.2.3 below, p. 42). The swelling amounted to about 5 - 9 % volume change in the circumferential direction, except for the uppermost block that swelled more and also in the vertical direction. The 10 mm gap filled with dry loose sand still remains between the bentonite buffer and the Opalinus Clay. Electron microscopic inspection of the interface between the bentonite and the sand shows a close indenting between the bentonite and the first layer of sand grains (Figure 5.1). The bentonite-sand layer separates easily, which was observable macroscopically and microscopically.

5.2 Results of laboratory measurements

5.2.1 Water content, density, and porosity

The gravimetric water content (according to Swiss Code SN 670 3406) of the bentonite determined on-site is on average 30.4 %. A vertical and radial distribution was found. In the heater region, the water content shows up to 10 % lower values, which can be assumed to be the result of drying due to heating. The inner part of the bentonite buffer shows a water content which is about 4 % higher (on average 33.4 % versus 29.5 %) caused by drying of the outer material before sampling (Figure 5.3).

The bulk wet density ρ determined with the Hg immersion method is on average 1.89 g/cm^3 and the calculated dry density ρ_d is 1.47 g/cm^3. According to the water content, the dry density shows higher values in the heater region (1.45 to 1.55 g/cm^3 versus 1.35 to 1.47 g/cm^3) and, on average, the dry density is 0.8 g/cm^3 lower in the inner part of the bentonite buffer (Figure 5.4). On average, specific solid densities ρ_s of 2.582 g/cm^3 were measured with the He pycnometer. The calculated saturation is about 100 % for all samples.

Figure 5.2: Bentonite buffer with dry crack in 330-direction, blocks 12 to 5, depth 5.80-6.60 m, sensor FB00_05.80 at block 12, brownish coloration coming from the sensor due to corrosion during hydration.

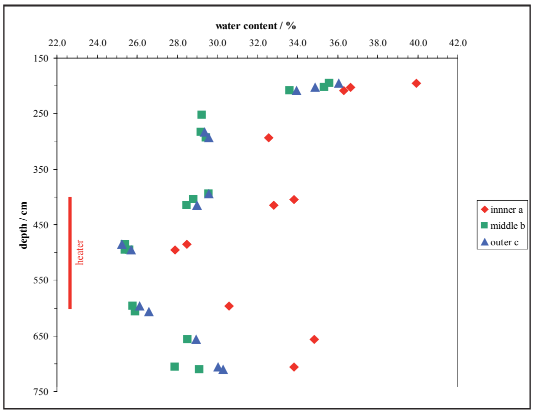

Figure 5.3: Distribution of the gravimetric water content in the bentonite determined on-site.

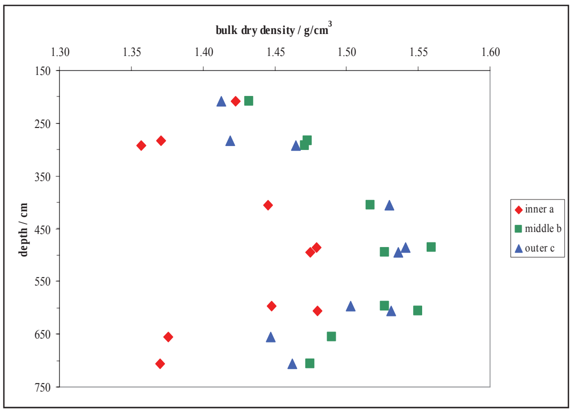

Figure 5.4: Vertical and horizontal distribution of the bentonite dry density in the buffer.

The porosity was measured using mercury intrusion porosimetry for open intracrystalline pores between 100 and 0.002 µm. The average pore radius is 9.3 nm. The measured total porosity is on average 11.7 %. This value is lower than the calculated porosity *n* from the experimental measurement of specific density and dry density with an average value of 41 % (Table 5.1). There is a significant volume of pores with a size of less than 2 nm (the innercrystalline pores on average 19.4 %) or not interconnected (about 10 %).

Specific surface areas were determined by N_2-adsorption measurements. An average value of 68 m^2/g was measured. The lowest values were found for bentonite from the heater region (Figure 5.5). In contrast to nitrogen, which is adsorbed at the external surface of the stacks of layers only, water molecules can be adsorbed on the whole surface, including the interlayer surface of smectite. The amount of adsorbed water is in equilibrium with the relative humidity. Water vapour gravimetric adsorption measurements were carried out by storing the samples at defined relative humidity for two weeks. Storing the samples at 90% relative humidity causes water contents up to 21%. Storing at 75% relative humidity causes two adsorbed water layers. The average water content reached 19.33%. This water content can be seen as an expression of innercrystalline porosity (interlayer, water accessible only). The overall surface was calculated under the assumption that 1% water in a monomolecular layer covers 35 m^2. By subtraction of the BET surface (outer surface), the inner surface as a measure for the amount of swellable layers can be calculated. The values are similar for all samples (520 - 560 m^2/g).

ESEM investigations show closing of the dry cracks at elevated relative humidity due to swelling (Figure 5.6). This process takes place on a timescale of seconds. At the in-situ determined water content of about 30% cracks should be closed.

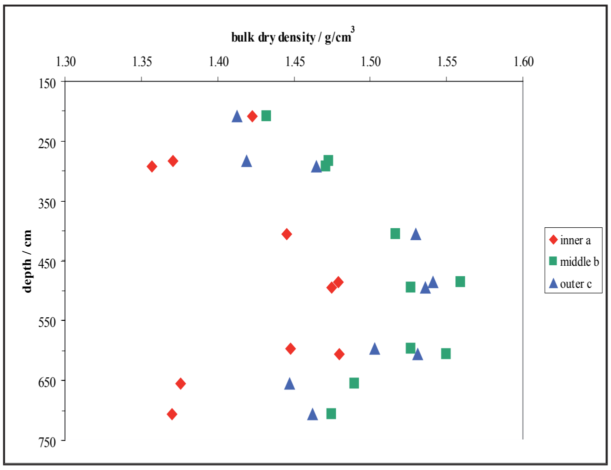

Figure 5.5: BET external surface of the bentonite on various positions in the buffer.

5.2.2 Mineralogical and chemical analysis

X-ray diffraction analyses were carried out to identify and quantify the mineralogical composition of both the bulk material and the < 2 µm fraction. No significant differences were found between the excavated samples and in relation to the untreated FEBEX bentonite. The predominant mineral is a smectite (90%). The smectitic phases are made up of a smectite - illite mixed layer, with about 8% illite. The bentonite also contains minor amounts of quartz (2%), feldspar (8%) and calcite (1%). The < 2 µm fraction contains about 95% smectite. Small amounts of quartz and illite could be found. The basal spacing d(001) of the smectite shows slight variations between 13.8 Å and 14.8 Å without any relationship to depth or horizontal distance to the heater. The average value is 14.32 Å, which indicates a predominance of divalent cations in the interlayer position. The investigation of the XRD basal spacing of the montmorillonite at various relative humidities (RH) shows a smeared stepwise interlayer swelling from 12.3 Å (at 5% RH) to 15.5 Å (at 75% RH), which is typical for a calcium montmorillonite (Plötze & Kahr 2003). Calculation of FWHM (full width at half maximum) for the (001)-lines does not show a significant evolution in the thickness of the clay particles. The crystallite thickness (calculated with Scherrer relation) is close to 50 Å for all samples.

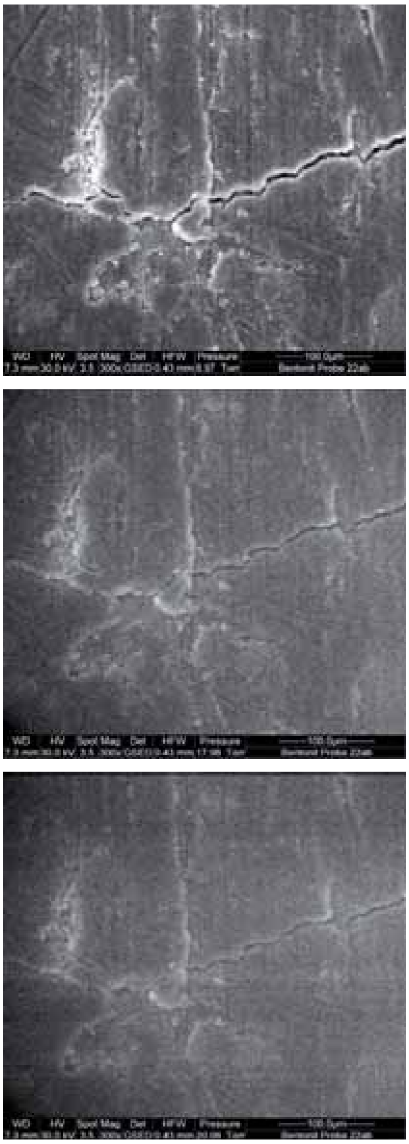

Figure 5.6: ESEM pictures of bentonite sample 22 at 40 % relative humidity (top) to 90 % relative humidity (bottom). Pictures are taken after 1 min equilibration time.

The relationship between XRD basal spacing and the mean layer charge calculated using the n-alkylammonium ion-exchange technique were used to determine changes in the mean total layer charge and charge distribution. The material is very homogeneous concerning the layer charge ξ and layer charge distribution with the average layer charge $\xi = 0.35 \pm 0.01$. There is a very weak decrease in the layer charge for montmorillonite from the heater region (sample 22, $\xi = 0.33$), which could be explained with a possible migration of small interlayer cations (e.g. Li^+) into vacant octahedral sites (Hofmann & Klemen 1950). The cation exchange capacity values lie on average at 103 meq/100 g. There are no changes in relation to the heater position.

IR spectra serve as a fingerprint to distinguish between different clay minerals and to provide fundamental information on their chemical composition, surface properties and structural changes that occur as a consequence of their chemical modification. The spectra obtained are very similar. They are dominated by the typical montmorillonite bands. In the clay size fraction, partially of sample 1, an iron oxyhydroxide contribution is to be mentioned. Disappearance of the Al-Mg-OH band at 845 cm^{-1}, which would be an indicator for the migration of small interlayer cations into vacant octahedral sites (Calvet & Prost 1971), as well as for Mg^{2+}- release from octahedral sites, could not be observed even in the purified clay size fraction because of the too small sensitivity of the method. A Si-O band indicates CT-opal, which was however not found with XRD.

The thermoanalytical curves showing weight changes during a heating procedure are almost identical for all samples. They show a dehydration peak at 106°C with a mass loss of 10.5%. The shift of the small shoulder at about 170°C to lower values for sample 22 is the sign of a relative decrease in calcium in the interlayer. The dehydroxylation peak at 657°C with a mass loss of 4.4% is typical for a *cis*-vacant montmorillonite. There is no shift of this peak to lower temperatures indicating a transformation in the *trans*-vacant form during the heating (EMMERICH et al. 1999).

No changes in the chemical composition of the clay were expected and found but in the interlayer and the pore solution. As the nature of the interlayer cations affects not only the exchange properties but also the swelling capacity and the rheological behaviour, the different cation occupations have been determined. The differences in the content of interlayer exchangeable cations are very small. The smectite contains to almost a third calcium, magnesium, and sodium ions in the interlayer. Minor amounts of potassium, iron, and manganese were found. The proportional amounts change in relation to the position in the buffer. Samples from the heater region show an increase in the amount of magnesium. To investigate the changes in the chemical composition of the pore solution, the ground samples were repeatedly eluted with methanol. The upper and lower blocks show a much higher content of sodium ions in the pore solution. This sodium possibly comes from the Pearson water used for hydration. The sodium content does not reflect the amount of sodium in the interlayer, it means that sodium was not exchanged in the interlayer of the smectite. Furthermore, an increase in iron and copper has to be mentioned in samples from outer positions in the bentonite of the heater region.

5.2.3 THM parameters

The capillary and interlayer water uptake with free swelling was determined using the Enslin-Neff technique on powdered bulk material and on pieces of the compacted bentonite. The powdered samples have a water uptake of on average 105%. The samples from the heater region show slightly lower and slower water uptake. Pieces of compacted bentonite soaked in much lower amounts of water during 24 h (Figure 5.7). The slower water absorption from samples near the heater seems to be an indicator of the influence of heating with associated cementing effects. Also, these samples show higher bulk dry densities and lower outer surfaces, which are parameters affecting the water absorption.

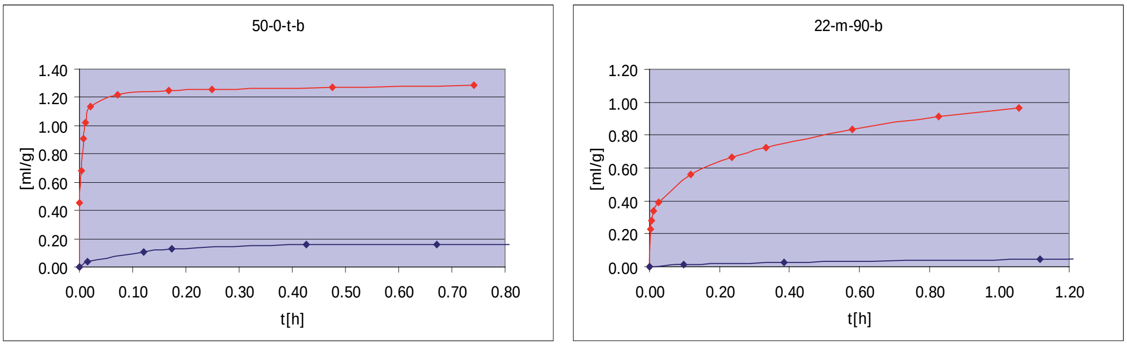

Figure 5.7: **Water uptake of selected samples from various vertical positions (50...top, 22…near heater) under free swelling conditions. Red – powder samples, blue – compacted bentonite.**

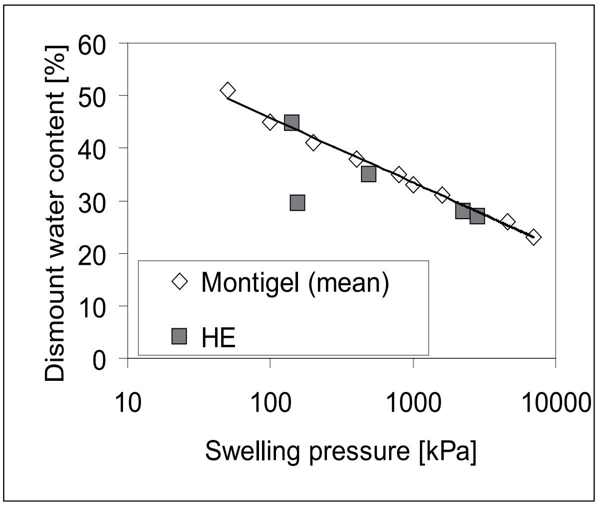

Figure 5.8: **Dismount water content vs. swelling pressure for the HE bentonite and - for comparison – for Montigel bentonite (Kahr et al. 1989).**

Specially designed swelling pressure oedometer cells were used to investigate the swelling behaviour of selected bentonite block samples. Desalted water and - in a second experiment - Pearson water were used for the percolation through the sample. A swelling pressure of the bentonite of up to 2.8 MPa was reached within 6 days. The swelling pressure shows the normal behaviour of a calcium bentonite (Figure 5.8).

Under the assumption that the volume of the water uptake adds to the total volume, the theoretical swelling strain was calculated at 50 to 80%. Sample 22 (near the heater) has the maximum free swelling potential. Sample 49 was already swollen in situ and shows the lowest values. The use of Pearson water causes about 10% smaller values of the swelling strain.

The main parameters describing the thermal properties of materials are the thermal conductivity λ (W/m/K) and the specific heat capacity *c* (J/kg/K). They are influenced by parameters such as mineralogy, porosity, water content, density, texture and temperature of the bentonite (Haehnel et al. 1988, Kahr & Müller-Vonmoos 1982). The thermal conductivity was measured with the Quick Thermal conductivity Meter (QTM), which is based on an impulse of thermal flow into the analysed material induced by a linear surface probe. The moist samples (water content w ~ 20.2%) show thermal conductivities of 1.25 to 1.30 W/m/K. Sample 22 (near the heater) has the highest value. The anisotropy is very weak. The air-dry samples show lower values (1.06 to 1.24 W/m/K), which reflects the large influence of the water content. To evaluate the influence of temperature and humidity on the heat conductivity, measurements were carried out at various temperatures and humidities. The value of the moist sample, registered at 90°C, is approximately 20% lower than that determined at ambient temperature, which corresponds to the general trend of decreasing thermal conductivity with increasing temperature. The measurement of the specific thermal capacity of rock samples is based on the principle of the mixing of two materials with different temperatures (Schärli & Rybach 2001). The specific heat capacity *c* of the air-dry and the moist samples are in the same range (1.12 – 1.30 J/g/K). The oven-dry samples show clearly a lower specific heat capacity (0.6 J/g/K).

5.3 Summary

The results indicate that the HE bentonite undergoes only small changes during the heater experiment. There are cementing processes, which slightly affect some THM characteristics such as porosity and thermal properties. The HE bentonite itself shows negligible changes in mineralogical characteristics during the heater experiment.

6. Experimental characterization of the host rock: Opalinus Clay

6.1 Mineralogy

6.1.1 Introduction

This study was conducted to answer the following questions:

1. Characterisation of the mineralogical composition of the Opalinus Clay and identification of differences.
2. Which measurable parameter might have an effect on mechanical properties?
3. Is it possible to identify an effect of the heating phase on clay properties?

According to state-of-the-art of clay mineralogy, the characterisation of clays (question 1) requires the enrichment of the so-called "clay fraction". Due to the small grain size of clay minerals, the clay fraction is defined as the "< 2 µm fraction". The complete separation of this fraction is only rarely achieved. It firstly requires a time-consuming disaggregation, because clay minerals might appear in aggregates which consist of fine-grained clay minerals bound by mineral cement. The cement can be either SiO_2, $CaCO_3$, iron-oxyhydroxides (like ferrihydrite or goethite) and/or organic matter. A particularly strong aggregation of clay minerals is often found in consolidated clays such as the Opalinus Clay. Commonly, a sophisticated chemical sample preparation technique is used for removing the four potential cements (Tributh & Lagaly 1986). However, a lot of data exist on how this procedure might affect clay minerals (e.g. change in layer charge density by changing the oxidation state of structural iron). It is, therefore, doubtful if this procedure is optimal for the characterisation of clays. Accordingly, it was decided to additionally test repeated ultrasonic treatment for disaggregation without the use of chemicals. Six samples which were taken before the heating phase were treated by both methods. Different grain size fractions were obtained by sieving and sedimentation. The effect of both treatments on the results of composition and additional parameters (like CEC and BET surface area) is discussed. Finally, the preferred method is used for the characterisation of four samples taken after the heating phase (to answer question 3).

6.1.2 Methods

6.1.2.1 Samples of Opalinus Clay

Six samples of Opalinus Clay from before the heating phase and four samples from after the heating phase were investigated. From each location, approximately 1.5 kg of borehole sample was homogenised for analysis. Therefore, a volume of ca. 1 dm^3 was considered as homogenous material. The exact locations of the boreholes are given in Figure 6.1. Sample 1-0-000 was collected by a chisel as close as possible ("directly") to the heater (next to the engineered barrier).

6.1.2.2 Method 1 for disaggregation (ultrasonic treatment)

For disaggregation by ultrasonic (US) treatment, about 80 g of air-dried Opalinus Clay were divided into eight portions of 10 g each. First, 100 ml of deionised water was added to each sample and kept for three days. Then, the samples were put into thin plastic cups in an ultrasonic bath (Qualilab USR 57, Figure 6.2). After 1 minute of US treatment, the generated suspension was passed through a 63 µm sieve and collected in buckets. The residue was returned to the sample in the ultrasonic bath.

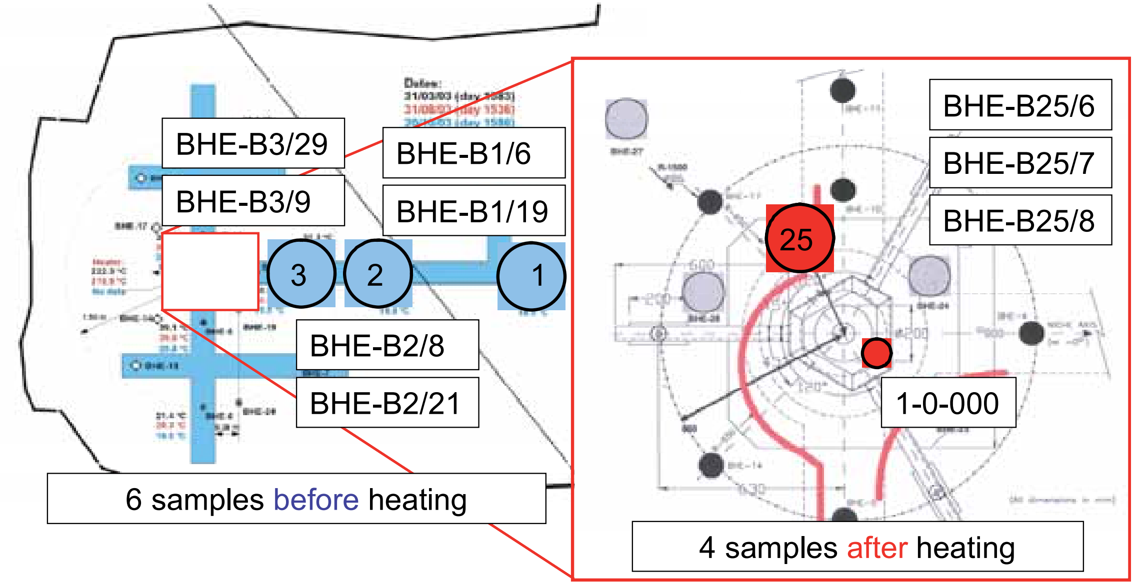

Figure 6.1: **Location of the boreholes contributing mineralogical samples.**

After each step, fresh deionised water was added and the ultrasonic treatment repeated. After 40 - 50 cycles, the time was increased to up to 15 minutes. Finally, approximately 35 l of suspension were obtained from each sample. To concentrate the solid in the suspension, NaCl was added as flocculating agent. The clear supernatant was removed. The solid was then washed with deionised water and the < 2 µm and 2 – 20 µm fractions were separated by sedimentation. The < 2 µm fraction was enriched by flocculation using NaCl and subsequently dialysed to remove excess NaCl. The coarser fractions were only washed with deionised water. Finally the samples were dried at 60°C and ground. Fractions > 20 µm were ground by a McCrone mill and passed through a 20 µm sieve. The finer fractions were ground by a hand mortar.

6.1.2.3 Method 2 for disaggregation (Tributh & Lagaly 1991)

According to Tributh & Lagaly (TL), it is possible to chemically remove the mineral and organic cement of clays. The modified Tributh-Lagaly treatment is divided into 3 steps:

- removal of carbonates
- removal of organic matter
- removal of iron oxides/hydroxides.

Siliceous cement was not present (< 0.06 wt.-%, determined for all samples) and Na_2CO_3-treatment for the removal of amorphous silica was therefore omitted. For removing carbonates, 100 g samples were reacted with 1 litre of an acetic acid – acetate solution (pH 4.8) at room temperature. The reaction time was 8 days and the suspension was stirred every 24 h for 1 h. The organic matter was removed by oxidation with H_2O_2 at room temperature. 100 ml of a 35% H_2O_2 solution were added to 200 ml suspension containing about 20 to 25 g clay. After 48 h, the suspension was heated to 70°C until ≈ 200 ml evaporated. To oxidise possible residues of organic matter, again 100 ml of a 10% H_2O_2 solution were added and heated to 70°C until another 100 ml evaporated. Iron oxides/hydroxides were removed using the dithionite-citrate-bicarbonate (DCB) method (MEHRA

& JACKSON 1960) which, in this study, was conducted at room temperature to save chlorite from dissolution.

Figure 6.2: Photograph of the thin plastic cup containing the mixture of sample and water which is placed in the ultrasonic bath. The generated suspension is decanted and collected in a bucket.

The content of SiO_2 which is soluble in sodium carbonate was determined by shaking a suspension of a 500 mg sample (dried at 105°C) and 50 ml 4% Na_2CO_3 solution. The SiO_2 content was < 0.1 wt.-% and dissolution of SiO_2 was therefore omitted. Between each step, the samples were washed three times with a 1 M NaCl solution (solid/liquid-ratio: 40 – 50 g/l). After all three steps, the samples were first treated four times with 1 M NaCl and then washed with deionised water. Then, the < 2 µm and 2 – 20 µm fractions were separated by sedimentation and the solid enriched by flocculation using NaCl, followed by dialysis in order to remove excess NaCl. Finally, the < 2 µm fractions were dried at 60°C and homogenised by grinding with a hand mortar. The other fractions were obtained by sieving.

6.1.2.4 Sample preparation and mineralogical methods

Approximately 1.5 kg of material were taken from the drillcores and crushed to below 5 mm by a jaw crusher. The samples were divided into 60 g portions for whole rock analysis, and 80 to 100 g portions for both disaggregation methods. The investigations of the water content are summarized in section 6.4 on p. 57 below. The bulk density was measured by a Micromeritics GeoPyc1360. The specific density of material dried at 105°C was determined by a He-Pycnometer (Micromeritics AccuPyc 1330). The porosity was calculated from bulk density, specific density and geotechnical water content. Moreover, the porosity was calculated by considering only the bulk density of air-dried material and the specific density of material dried at 105°C. However, the values obtained by both methods are almost identical.

The BET-surface area was determined by a Micromeritics Gemini using 5 adsorption points. The samples were dried at room temperature under vacuum for two days. The carbonate content was measured by a modified Scheibler method (KLOSA 1994). The sulphur, C and C_{org} content (content of organic carbon) were determined by a LECO CS-444 analyser. The cation exchange capacity (CEC) was also measured by the Cu_{triene} method (MEIER & KAHR 1999) and the $AgTu_{Cc}$ method (DOHRMANN 1997). The amount of soluble silica was determined photometrically by soda extraction according to KAUFHOLD (2001). XRD analyses were carried out by a Philips diffractometer (PW 3710) using CuK_{α} radiation. For quantitative mineralogical analysis, the Rietveld programme AutoQuan® was used. IR-spectra were recorded on a Nicolet Nexus FTIR-spectrometer (KBr pellets and MIR range). The quantitative mineralogical composition was derived from all results obtained (particularly XRD and XRF analyses).

6.1.3 Comparison of two methods for disaggregation

6.1.3.1 Amount of < 2 µm fraction and weight loss

Firstly, both methods (see sections 6.1.2.2 and 6.1.2.3) are compared with respect to the amount of the < 2 µm fraction obtained (Figure 6.3). It is clear that both methods provide comparable values if the < 2 µm fraction is referred to the initial weight (before chemical or mechanical treatment). If the < 2 µm fraction is calculated by referring its recovered weight to the total recovered weight (sum of fractions after treatment), significant deviations can be observed (Figure 6.3), which can be easily explained by the higher amount of carbonates which are dissolved during method 2 (Tributh & Lagaly 1991, TL). In the fractions obtained by method 1 (US), carbonates are not completely dissolved and therefore contribute to the recovered weight after treatment. This result is confirmed by Figure 6.4, which shows that the differences in the weight loss of both methods can be explained by the carbonate content. Of particular interest is the weight loss that can be explained only by frequent sample transfer from one bottle to another or by decantation.

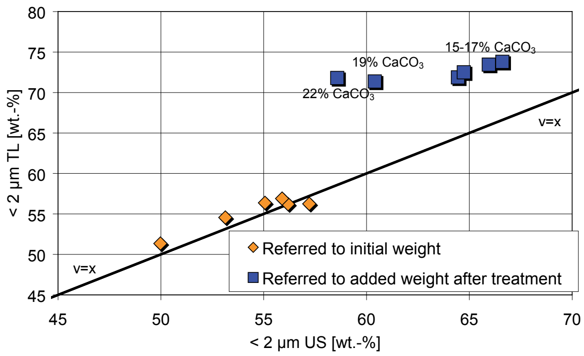

Figure 6.3: **Comparison of the amount of the < 2 µm fraction obtained by the two different disaggregation methods, see sections 6.1.2.2 and 6.1.2.3.**

For the ultrasonic treatment (method 1), 84 g of sample BHE 1/6 was used. After fractionation, the sum of all fractions was 73.9 g. Accordingly, 10.1 g were lost during the procedure. The extensive use of water during the ultrasonic treatment obviously led to the partial dissolution of calcite (80 % on average). The calcite content was calculated from TIC (LECO) of each fraction and added considering the portion of the respective fraction. It is clear that about 10 g of calcite were lost, which fully explains the observed weight loss of approximately 10 g. By considering S data (sulphur content; LECO) and conversion to pyrite, an additional 0.5 – 0.9 g loss of weight can be explained. By comparing the S content before and after US treatment (method 1), it is concluded that 30 – 40 wt.% (average 38 wt.%) of pyrite is dissolved. Organic carbon was not dissolved. For sample BHE 1/19, a remaining weight loss of 2.1% was recorded, which can only be explained by an unsystematic loss of weight and is therefore referred to as “loss of weight due to transfer” (meaning the sum of small unavoidable weight losses during repeated transfer of suspensions from one bottle to another).

In the case of method 2, the systematic weight loss is determined by the dissolution of organic matter (calculated from C_{org} using 1.4 as factor), $CaCO_3$ content, and the content of dissolved Fe phases (iron-oxy-hydroxides or pyrite, assumed to be 2%). The remaining weight loss is significantly higher when using method 2 (4.5% compared to 1.6%).

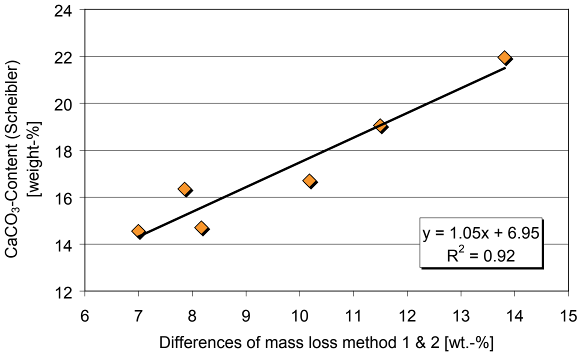

Figure 6.4: **Differences in the weight loss of both disaggregation methods (see sections 6.1.2.2 and 6.1.2.3) can be explained by the calcite content..**

6.1.3.2 Grain size distribution

In Table 6.1, the grain size distributions of the samples obtained by the two disaggregation methods are shown. The amounts were calculated by referring the recovered weight of each fraction to the sum of recovered material. Using method 1 (US), higher amounts of the coarse fractions (20 – 63 and > 63 µm) were found, which can be attributed to the presence of coarse grained carbonates which were not dissolved (compare Figure 6.3 and Figure 6.4). Sample BHE 1/19 has an exceptionally high content of coarse grains, particularly of > 63 µm, which were almost entirely removed when using method 2.

Table 6.1: Amounts of fractions after treatment for both disaggregation methods (in wt.% referred to recovered weight).

	US	TL	US	TL	US	TL	US	TL
	< 2 µm		2-20 µm		20-63 µm		> 63 µm	
BHE 1/6	60.4	71.4	33.2	27.8	2.4	0.9	4.0	0.0
BHE 1/19	58.6	71.8	28.8	27.4	2.9	0.6	9.8	0.2
BHE 2/8	66.6	73.8	30.9	25.4	1.4	0.6	1.1	0.2
BHE 2/21	64.4	71.9	31.3	27.6	1.6	0.5	2.6	0.0
BHE 3/9	65.9	73.4	28.7	26.0	1.7	0.5	3.7	0.1
BHE 3/29	64.7	72.5	30.7	27.0	1.3	0.5	3.2	0.0

11.1.2.3 BET surface area

The BET surface area as determined by N_2 adsorption in the presence of swelling clay minerals can be strongly influenced by the type of interlayer cation (lower for Na^+ than for Ca^{2+}) and by organic matter blocking micropores, which, in turn, leads to a lower surface area. Samples treated by disaggregation method 2 can have lower BET values due to Na^+ as a counter–ion, but higher values due to the removal of organic matter. Results are compared in Table 6.2. The BET surface area of the investigated samples is determined particularly by the swelling clay minerals. Therefore, a significantly higher surface area of the < 2 µm fraction, as shown in Table 6.2, was expected. Obviously, the chemical treatment caused an increase in the BET surface area (5 - 7 m^2/g). The dissolution of organic matter is known to increase the surface area of clays by deblocking pores at the edges of the clay minerals. In contrast, the BET values of the 2 – 20 µm fractions are lower for the material produced by disaggregation method 2. This difference cannot be explained clearly. Probably, the 2 – 20 µm fractions produced by disaggregation method 1 contain more goethite, which is dissolved in method 2. Additionally, it is assumed that the content of clay minerals is slightly higher in the 2 – 20 µm fractions (method 1).

Table 6.2: BET surface area of samples pre-treated by either of the 2 disaggregation methods.

Sample		US	TL	US	TL
	initial material	< 2 µm		2 - 20 µm	
	[m²/g]	[m²/g]	[m²/g]	[m²/g]	[m²/g]
BHE 1/6	30.0	54.0	59.7	14.0	6.4
BHE 1/19	30.0	55.0	62.3	14.0	7.1
BHE 2/8	33.0	54.0	62.2	16.0	7.5
BHE 2/21	32.0	55.0	62.4	13.0	6.5
BHE 3/9	32.0	54.0	61.5	13.0	7.2
BHE 3/29	31.0	55.0	61.9	14.0	7.2

6.1.3.4 Chemical composition

The differences between the two disaggregation methods were evaluated by the chemical composition of the < 2 µm and the 2 – 20 µm fractions. The < 2 µm fractions produced by method 2 have about 1 wt.% less Fe_2O_3, which can be explained by the dissolution of iron-oxyhydroxides or pyrite. Trace elements like Co, Ni, Zn and possibly Ce are assumed to be associated with the iron phases, leading to smaller contents in the < 2 µm fractions produced by method 2. Due to dissolution of calcite, the CaO values are slightly lower. In the 2 – 20 µm fractions, 4 – 5% less Fe_2O_3 was analysed due to the dissolution of Fe-phases which – similar to the < 2 µm fraction – may have led to a reduction of Ce, Co, Cu, Ni, V and Zn. On the other hand, the SiO_2 contents are 7 – 9% higher in the 2 – 20 µm fractions produced by method 2. This can be explained by a higher quartz content. The slightly higher Ba contents of samples produced by method 2 would suggest increased feldspar contents. These results are further discussed in the following section.

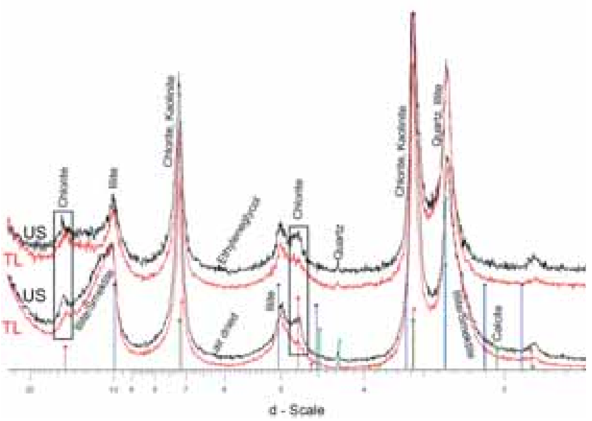

Figure 6.5: Comparison of the XRD-analyses of the < 2 µm fractions for the 2 disaggregation methods of the representative sample BHE 3/9. XRD pattern were recorded as texture slides with (above) and without ethylene glycol solvation (below).

6.1.3.5 XRD analysis

The < 2 µm and 2 – 20 µm fractions obtained by the two disaggregation methods are compared by X-ray diffraction (XRD) analyses. As almost the entire amount of the fractions > 20 µm obtained by method 2 was used for XRF analysis, it was not possible to investigate these fractions by XRD.

According to the previous section, no significant chemical differences between the < 2 µm fractions were detected by the two disaggregation methods. This result is confirmed by XRD analysis (Figure 6.5). The only difference is a slightly sharper 001-reflection of chlorite (at about 14 Å), which is particularly evident in the XRD pattern after treatment with ethylene glycol. The shoulder of illite-smectite mixed layer minerals of the fractions < 2 µm produced by both methods disappears due to treatment with ethylene glycol, indicating a random mixed layering.

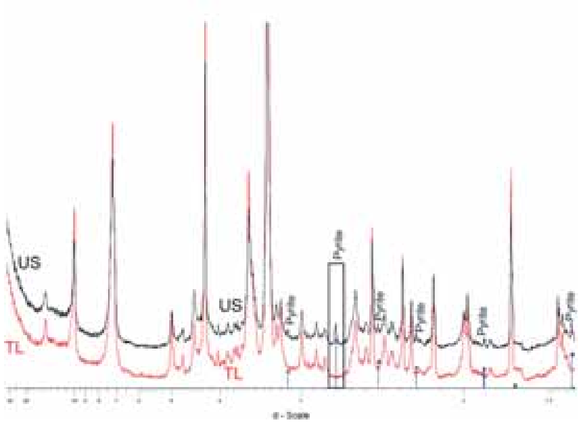

Figure 6.6: Comparison of the XRD-analyses of the 2 - 20 µm fractions obtained for the 2 disaggregation methods of the representative sample BHE 3/9.

According to the previous section, significant chemical differences between the 2 – 20 µm fractions were found for the 2 disaggregation methods. XRD analysis (Figure 6.6) only shows the complete disappearance of the pyrite reflections at: 3.12, 2.70, 2.42, 2.21, 1.91, and 1.63 Å. Obviously, pyrite is at least partly preserved by the ultrasonic treatment. The qualitative interpretation of the pattern did not indicate differences in the quartz contents which could explain the chemical differences. By applying the quantitative Rietveld-analysis, 6% more quartz and 1% more feldspar were found, which explains the chemical differences quite well.

6.1.3.6 Cation exchange capacity (CEC)

In Table 6.3, the cation exchange capacities (CEC) of the samples collected before the heating phase are compared. It can be concluded that the repeated washing steps using NaCl solution of disaggregation method 2 caused a more complete Na saturation. For the production of the < 2 µm fraction by method 1, NaCl was only used for flocculation (no extensive washing steps). Obviously, this treatment did not lead to complete cation exchange of Ca^{2+} by Na^{+} (initially about 1 : 1). However, the sum of cations and CEC values of the < 2 µm fractions obtained by both methods are comparable. Therefore, it can be deduced that the chemical treatment (method 2) did not affect the charges of the clay minerals. The cation populations do not represent the initial state of the Opalinus Clay.

6.1.3.7 Determination of an appropriate method for disaggregation

In conclusion, the ultrasonic method (method 1) is appropriate for quantitative separation of the < 2 µm fractions of Opalinus Clay. Surprisingly, the chemical and mineralogical compositions of these fractions produced by both methods are almost identical. Significant differences were observed in the fractions 2 – 20 µm and > 20 µm as discussed in section 6.1.3.5 above (p. 47). With respect to the quantitative Rietveld analysis, differences in the > 2 µm fractions do not cause serious problems. The quantitative analysis of clay minerals which are enriched in the < 2 µm fractions is still a challenge. For mineral quantification, particularly of the < 2 µm fractions, both methods are appropriate. For the pre-treatment of the samples after heating, method 1 was selected due to the following advantages:

- Less loss of weight,
- Fe-minerals are not completely removed; no interference of Fe-minerals with respect to XRD analysis was found,
- At least a larger amount of calcite is preserved; therefore the calcite distribution can be assessed slightly better,
- The C_{org}-distribution can be analyzed,
- The layer charge distribution of clay minerals is not chemically affected by oxidation and/or reduction.

Table 6.3: CEC and exchangeable cations of the < 2 µm fractions obtained by the 2 disaggregation methods (S-value = sum of cations, T-value = CEC, S-T-value = difference between sum of cations and CEC).

Sample	Method	Na [meq/100g]	K [meq/100g]	Mg [meq/100g]	Ca [meq/100g]	S-value [meq/100g]	T-value [meq/100g]	S-T-value [meq/100g]
BHE 1/6	US	16.7	0.6	1.2	4.3	22.8	22.9	-0.1
BHE 1/6	TL	20.6	0.6	0.8	0.1	22.1	23.5	-1.4
BHE 1/19	US	15.3	0.7	1.3	3.9	21.2	21.7	-0.5
BHE 1/19	TL	20.0	0.6	0.6	0.0	21.2	23.0	-1.8
BHE 2/8	US	16.3	0.8	1.0	3.6	21.7	22.0	-0.3

BHE 2/8	TL	19.7	0.7	0.8	0.1	21.3	23.4	-2.1
BHE 2/21	US	16.4	0.7	1.0	3.8	21.9	22.2	-0.3
BHE 2/21	TL	20.3	0.7	0.6	0.1	21.7	23.6	-1.9
BHE 3/9	US	18.3	0.4	1.3	3.9	23.9	23.8	0.1
BHE 3/9	TL	19.8	0.7	0.7	0.1	21.3	23.2	-1.9
BHE 3/29	US	18.2	0.5	1.0	3.4	23.1	23.7	-0.6
BHE 3/29	TL	19.5	0.7	0.6	0.1	20.9	23.1	-2.2

6.1.4 Comparison of samples before and after the heating phase

For fractionation, the more advantageous disaggregation method 1 was used. From temperature sensors which monitored the experiment throughout the heating phase, it can be concluded that the Opalinus Clay located close to the engineered barrier was heated up to about 40°C, which is insignificant compared with the geological history of this clay.

6.1.4.1 Chemical composition

The chemical composition of the bulk material of all samples is comparable. The main differences are reflected by the mineralogical composition, which is discussed in the following section. Significant chemical differences were observed in the > 20 µm fractions. Particularly high Zn and Pb contents were found in sample 2/8. Due to the high Fe_2O_3 content of this sample, it is conceivable that Zn and Pb are associated with Fe-minerals such as goethite. This assumption is supported by the composition of sample 25/6, which also contains much Fe_2O_3 and relatively much Zn and Pb. From these data it can be tentatively concluded that the trace element composition of Fe-minerals is quite variable in the Opalinus Clay.

6.1.4.2 Quantitative mineralogical composition

The mineralogical composition was determined by XRD, LECO, CEC and XRF analyses of the initial samples and of all fractions obtained by disaggregation method 1, cf. Table 6.4. XRD patterns were analysed by the Rietveld technique (AutoQuan®). The quantitative results for each fraction were compared with the chemical composition by adding the atomic masses according to the mineral formula and the content suggested by AutoQuan®. Particularly the contents of minerals such as kaolinite, which are known to show small chemical variation but are difficult to describe by crystal models for AutoQuan® calculations, were corrected using this procedure. The chemical composition of illite, smectite, illite/smectite mixed layers and chlorite had to be assumed. The amount of smectitic layers (smectite and smectitic layer in illite/smectite mixed layer minerals) was calculated by CEC using the assumption of a layer charge density accounting for 0.33 C/FU (charge per formula unit) and a variable charge of 15%. For the correction of pyrite and carbonate contents, the LECO values were taken into account. After fitting the XRD results using the parameters mentioned above, the results were synthesised considering the weight loss during fractionation. Significant differences were only observed for calcite and pyrite, which partially dissolve. The contents of illite, smectite (illite/smectite mixed layer minerals) and muscovite were added and assigned as "dioctahedral 2:1 layered silicates" because the XRD intensities can be hardly distinguished. This sum is assumed to be correct. The results indicate that the Opalinus Clay contains irregular illite/smectite mixed layer minerals with a content of smectitic layers of 30 - 50%.

Table 6.4: Quantitative mineralogical composition of all investigated samples.

	Calcite	Chlorite	Goethite	Gypsum	2:1 dioc. layered Silicates (Ill, Smt, Musc.)	*Smectitic layers thereof*	K-Feldspar	Kaolinite	Na/Ca-Feldspar	Pyrite	Quartz	Rutile	Siderite	C_{org}
	[wt.%]	[wt.%]	[wt.%]	[wt.%]	[wt.%]	*[wt.%]*	[wt.%]	[wt.%]	[wt.%]	[wt.%]	[wt.%]	[wt.%]	[wt.%]	[wt.%]
Samples before heating														
BHE 1/6	16	9	2	1	30	*10*	3	23	1	2	10	1	1	1
BHE 1/19	**18**	7	1	1	31	*14*	3	20	2	2	12	1	1	1
BHE 2/8	13	8	1	1	32	*12*	4	24	1	2	11	1	1	1
BHE 2/21	13	8	2	1	32	*12*	4	23	1	2	11	1	1	1
BHE 3/9	14	8	2	1	32	*12*	3	23	1	3	10	1	1	1
BHE 3/29	14	8	2	1	33	*12*	3	23	1	2	10	1	1	1
Samples after heating														
BHE 25/6	14	8	2	1	33	*13*	3	22	1	3	10	1	1	1
BHE 25/7	14	8	1	1	33	*12*	3	22	2	2	10	1	2	1
BHE 25/8	**22**	8	1	1	30	*11*	2	19	1	2	10	1	2	1
BHE 1 0 000	17	8	1	1	31	*12*	3	22	1	2	10	1	2	1

As can be seen in Table 6.4, the quantitative mineral composition of all investigated Opalinus Clay samples is comparable. Samples BHE 1/19 and BHE 25/8 show a higher content of calcite and a lower clay mineral content. Compared to the mineralogical composition given by NÜESCH (1991), less quartz and more kaolinite were found. The results of Table 6.4 agree quite well with the mineralogical composition given by NAGRA (2002).

Carbonates are considered important minerals with respect to geological barriers because they influence the pH value of pore fluids and therefore the solubility and stability of minerals. Furthermore, their content in the Opalinus Clay is variable, which may have an effect on mechanical properties. For the quantitative determination of the carbonate content two methods are compared. The total inorganic C content (TIC) was determined by LECO. The calculation of the $CaCO_3$-content is based on the stoichiometry. Results can be affected by the presence of carbonates other than calcite. The second method (Scheibler method) is based on the reaction of carbonates with HCl. In a closed system, the pressure – resulting in the reaction product CO_2 – depends on the content of carbonates. As can be seen in Figure 6.7, the $CaCO_3$-content determined by the Scheibler method is approximately 10% higher than the value derived from the total inorganic carbon content (TIC). This can be explained by the presence of sulphides (pyrite). If sulphides react with the acid they form H_2S which contributes to the total pressure from which the $CaCO_3$ content is calculated. Based on sample B1/19 (does not contain gypsum), 1.1 wt.% S is supposed to derive from pyrite (≈ 2 wt.%). Based on an approximation following the ideal gas law, it was calculated that 1 wt.% S leads to a $CaCO_3$ overestimation of 3 wt.%. Therefore, it can be concluded from Figure 6.7 that pyrite does not dissolve completely in HCl; otherwise an even higher $CaCO_3$ content would have been determined by the Scheibler method.

6.1.4.3 Grain size distribution

In Table 6.5 the amounts of the different grain size fractions of samples collected before and after the heating phase are compared. Theoretically, heat treatment is supposed to facilitate aggregate formation and/or stabilization, which, in turn, can lead to coarser grains in the heated samples. Statistically, samples collected after the heating phase show a higher content of the 2 – 20 µm fraction and a lower content of the < 2 µm fraction. Besides the fact that a total of four or six samples should not be interpreted statistically, these results cannot be related to temperature effects. They rather reflect mineralogical differences (carbonate content).

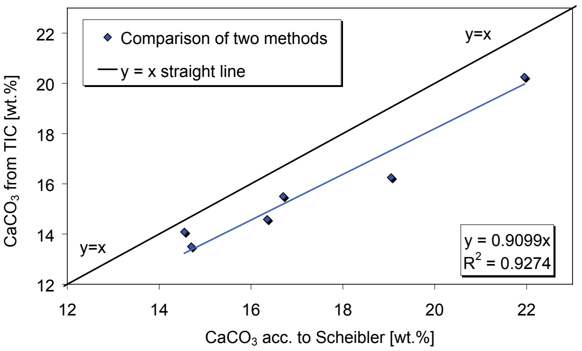

Figure 6.7: Comparison of the CaCO3-content obtained by two different methods (Scheibler and TIC, see text of section 6.1.4.2).

6.1.4.4 Water uptake capacity

Comparing the water content of differently transported samples, a significant weight loss (1 - 2%) depending on packaging and duration of transport was observed. Additionally, it is likely that water is lost during drilling. Therefore, it is not possible to determine “correct” water contents of the clay representing the original state. Before carefully sealing the samples, a water content of 4 - 6 wt.% was measured, which increased to ca. 7 wt.% (Klinkenberg 2004, unpublished) due to fast transport and careful sealing.

However, the affinity of the clay for water is an important property of the material. To determine the affinity for water (water uptake capacity), which highly influences water contents, water adsorption isotherms were recorded by a stepwise increase in the relative humidity of dried (60°C) and ground material. The “zero-value” was determined after adsorption by oven-drying at 105°C for 4 days. An equilibration time of 12 hours per step (4 g sample in Al crucible with a diameter of approximately 7 cm) was sufficient. As can be seen in Figure 6.8, sample 1-0-000 has the lowest water uptake capacity, which might be an effect of the heating phase. Generally, samples collected after the heating phase show lower water uptake capacities, particularly the sample which comes directly from the heater. However, it is not possible to conclude without doubt that this is actually an effect of the heating phase. Theoretically, swelling clay minerals can irreversibly collapse upon drying. This effect usually occurs at temperatures > 100°C. The reasons for the different water uptake capacities are investigated in Table 6.6. The water uptake (in wt.%) is given at 10, 50 and 70% relative humidity, where 10% represents the rapid water uptake. According to Keeling et al. (1980), the water uptake capacity at 50 and 70% can be tentatively correlated with the surface area. The degree of water uptake at 50 and 70% relative humidity can be explained by the amount of exchangeable Na^+ ions in the interlayer of swelling clay minerals, cf. Figure 6.9. Due to a comparable ratio of exchangeable cations (Ca+Mg)/Na, this parameter is related to the amount of clay minerals, which, in turn, strongly influences the amount of the < 2 µm fraction. The significant differences for the water uptake at 10% relative humidity cannot be explained yet.

Table 6.5: Comparison of the grain size distribution of samples before and after the heating phase (values obtained by method 1).

Samples before heating							
	BHE 1/6 [wt.%]	BHE 1/19 [wt.%]	BHE 2/8 [wt.%]	BHE 2/21 [wt.%]	BHE 3/9 [wt.%]	BHE 3/29 [wt.%]	Mean [wt.%]
< 2 µm	60.4	58.6	66.6	64.4	65.9	64.7	63.5
2 - 20 µm	33.2	28.8	30.9	31.3	28.7	30.7	30.6
20 - 63 µm	2.4	2.9	1.4	1.6	1.7	1.3	1.9
> 63 µm	4.0	9.8	1.1	2.6	3.7	3.2	4.1
Samples after heating							
	BHE 25/6 [wt.%]	BHE 25/7 [wt.%]	BHE 25/8 [wt.%]	BHE 1 0 000 [wt.%]			Mean [wt.%]
< 2 µm	62.0	58.1	47.5	52.6			55.1
2 - 20 µm	34.3	39.8	37.5	38.4			37.5
20 - 63 µm	1.7	1.9	2.7	2.6			2.2
> 63 µm	2.1	0.2	12.3	6.4			5.2

Table 6.6: Water uptake capacities of all samples at 10, 50, and 70 % relative humidity, and correlation with parameters that theoretically influence the water uptake capacity.

Sample	wt.% H_2O 10% rel. hum.	wt.% H_2O 50% rel. hum.	wt.% H_2O 70% rel. hum.	CEC Cu [meq/100g]	< 2 µm [wt.%]	BET [m2/g]	exch. Na [meq/100g]	Porosity [%]	water content [wt.%]
BHE 1/6	0.5	1.2	2.0	9.9	60.4	30.0	6.4	16.0	1.0
BHE 1/19	0.6	1.3	2.0	10.0	58.6	30.0	5.3	15.0	1.6
BHE 2/8	1.3	1.8	2.6	10.8	66.6	33.0	7.2	17.0	1.3
BHE 2/21	0.9	1.5	2.3	11.3	64.4	32.0	6.3	15.0	1.6
BHE 3/9	0.7	1.4	2.1	10.9	65.9	32.0	6.0	14.0	1.7
BHE 2/29	0.5	1.6	2.4	10.6	64.7	31.0	7.0	14.0	1.8
BHE 25/6	0.5	1.4	2.3	12.3	62.0	33.8	6.4	16.1	1.7
BHE 25/7	0.5	1.3	2.2	12.3	58.1	33.4	6.5	14.5	1.6
BHE25/8	0.6	1.1	1.8	11.1	47.5	30.6	5.7	16.2	1.4
1-0-000	0.3	1.0	1.7	11.7	52.6	32.0	5.3	18.5	1.6
corrl.with CEC	0.0	0.0	0.0						
corrl. with <2µm	0.3	**0.7**	**0.6**						
corrl. with BET	0.1	0.1	0.3						
corrl. with ex.Na	0.3	**0.6**	**0.8**						
corrl. with Por.	0.0	0.1	0.1						
corrl. with water	0.1	0.0	0.0						

6.1.4.5 BET surface area, density, and porosity

The BET surface area is significantly influenced by the microporosity of layered silicates. Upon drying, swelling clay minerals might collapse, which reduces the BET surface area. Comparing the BET values for samples collected before and after the heating phase, no differences could be observed. The collapse of swelling clay minerals can also affect density and porosity. Porosity values were first calculated directly by the Micromeritics GeoPyc1360 device which measures the bulk density of air-dried material (additional input: weight, specific density). The values in Table 6.7 were calculated by the equation

$$n = 1 - \frac{\rho_b}{\rho_s} \cdot 100 \qquad (\ 1\ )$$

where n is the porosity [-], ρ_b the bulk density [g/cm^3] and ρ_s the specific density [g/cm^3]. Equation (1) is also used by the GeoPyc1360. Therefore, the small differences between both methods cannot be explained.

However, the values are almost identical. The specific density of the samples collected after the heating period shows slightly lower values (ca. 2.68 g/cm^3 compared to 2.71 g/cm^3). To find out whether the difference is caused by the heating period or by the measuring device, the six samples collected before the heating period were investigated again. The new values are slightly lower (by 0.02 - 0.03 g/cm^3) and therefore comparable with the values of the samples collected after the heating period (Table 6.7). The specific density, therefore, does not show a difference in material properties caused by the heating period. The shift of the values cannot be explained. A detailed discussion is given in section 6.4.1.2.

6.1.4.6 Cation exchange capacity (CEC)

The CEC (including the type of exchangeable cations) was determined by different methods in order to explain the difference between sum of cations and CEC values, and to verify the results obtained (Table 6.8). The exchangeable cations of samples collected before the heating phase were determined by the $AgTu_{Cc}$ method (the exchange solution is saturated with calcite which prevents dissolution of calcite from the sample during the run of the CEC experiment, which in turn minimises the falsification of the Ca^{2+} values). The Cu_{triene} method was carried out without calcite saturation, which led to a partial dissolution of calcite and therefore to higher (slightly erroneous) Ca^{2+} values. In order to be able to directly compare CEC values, all samples were analysed by the Cu_{triene} method by visible spectroscopy. The differences observed between the T value of a CEC value obtained by ICP analysis of Cu^{2+} and the T value obtained by visible spectroscopy (T-v. VIS) represent the analytical accuracy of approximately 1 meq/100 g.

For the samples collected after the heating phase, slightly higher values were observed. It is well accepted that heating reduces the CEC. The obtained values therefore do not reflect an effect of the heating phase. More likely, due to the different sample locations, these samples have a slightly higher content of swelling clay minerals. Samples collected after the heating period show higher Ca2+ and lower Na+ values, which is an effect of a lower amount of NaCl solution used for flocculation.

Systematic differences in the CEC between the samples collected before and after the heating phase could not be observed.

Table 6.7: Density and porosity of the bulk material.

Samples before heating		*(porosity = [1-(bulkdens./spec.dens.)]*100*						
		BHE 1/6	BHE 1/19	BHE 2/8	BHE 2/21	BHE 3/9	BHE 3/29	Mean
specific density	[g/cm^3]	2.68	2.69	2.68	2.68	2.68	2.66	2.68
bulk density	[g/cm^3]	2.27	2.28	2.22	2.28	2.30	2.29	2.27
porosity	[%]	15.3	15.2	17.2	14.9	14.2	13.9	15.1
Samples after heating								
		BHE 25/6	BHE 25/7	BHE 25/8	BHE 1 0 000			Mean
specific density	[g/cm^3]	2.69	2.67	2.69	2.69			2.68
bulk density	[g/cm^3]	2.25	2.29	2.25	2.19			2.25
porosity	[%]	16.1	14.5	16.2	18.5			16.4

Table 6.8: Exchangeable cations of all samples investigated by two different CEC methods (bulk sample).

Sample	Na [meq/100g]	K [meq/100g]	Mg [meq/100g]	Ca [meq/100g]	S-value [meq/100g]	T-value [meq/100g]	T-v. VIS [meq/100g]	S-T-value [meq/100g]
AgTu_{Cc}-Method								
BHE 1/6	6.4	1.0	2.2	6.1	15.7	12.2	x	3.5
BHE 1/19	5.3	0.9	2.6	6.5	15.3	12.2	x	3.1
BHE 2/8	7.2	1.1	2.6	5.9	16.8	12.7	x	4.1
BHE 2/21	6.3	1.1	2.8	7.4	17.6	12.7	x	4.9
BHE 3/9	6.0	1.0	2.6	7.0	16.6	11.7	x	4.9
BHE 3/29	7.0	1.1	2.7	4.8	15.6	12.5	x	3.1
$\text{Cu}_{\text{Triene}}$-Method								
BHE 1/6	x	x	x	x	x	x	9.9	x
BHE 1/19	x	x	x	x	x	x	10.0	x
BHE 2/8	x	x	x	x	x	x	10.8	x
BHE 2/21	x	x	x	x	x	x	11.3	x
BHE 3/9	x	x	x	x	x	x	10.9	x
BHE 3/29	x	x	x	x	x	x	10.6	x
BHE 25/6	6.4	1.3	2.7	*8.7*	19.1	12.0	12.3	7.1
BHE 25/7	6.5	1.2	2.6	*8.0*	18.3	11.7	12.3	6.6
BHE 25/8	5.7	1.2	2.4	*8.0*	17.3	10.8	11.1	6.5
1 0 000	5.3	1.2	3.2	*9.0*	18.7	11.6	11.7	7.1

6.2 Microstructural investigations

In contrast with the very subtle mineralogical differences detected in Opalinus Clay samples, a large variability was observed in four samples subjected to a preliminary microstructural study. Three samples were analysed with standard petrographic techniques using a polarising microscope (BLT 2/4, 3/21, 4/8) and one sample (BLT 2/22/2) was investigated with a scanning electron microscope (SEM). In spite of their origin from a confined interval in the same borehole, the samples are inhomogeneous on various scales. Variability affects microstructural phenomena that are related to the integrity of the samples and to the direction of partings.

For the explanation of rock mechanical data, it is probably more important to consider the microstructure than the mineralogical composition. It is likely that the mechanical stability of the Opalinus Clay depends on cracks and shell fragments (Figure 6.10 and Figure 6.11), which represent some kind of predetermined breaking planes.

6.2.1 Light microscopy

Samples BLT 2/4, 3/21, and 4/8 differ in grain size distribution, in the degree and type of cementation and in the amount and type of cracks (Figure 6.10). All samples are strongly anisotropic as a result of sub-parallel bedding planes. In addition to bedding, another preferred orientation (45° to bedding) is developed in the samples. This points to localized directional stress in the Opalinus Clay, much in the way of a foliation. Cracks from drying or sample preparation, which are of great importance for rock mechanical analyses, have opened along primary cracks or inhomogeneities. Carbonates or siliceous phases precipitated along primary cracks. Pyrite-filled bioturbation structures are partly oxidised to iron hydroxide.

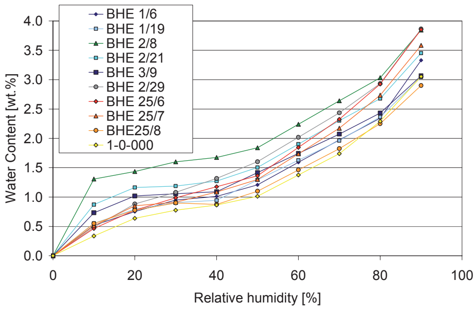

Figure 6.8: **Water uptake of all investigated samples of the Opalinus Clay (samples after the heating phase: red and yellow).**

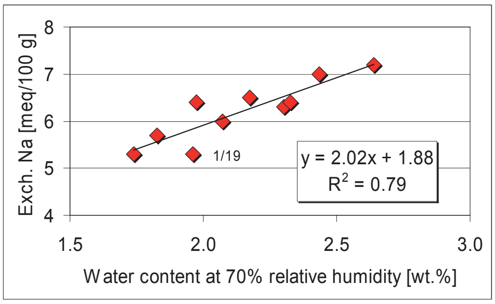

Figure 6.9: **Comparison of water uptake at 70 % with the amount of exchangeable Na+.**

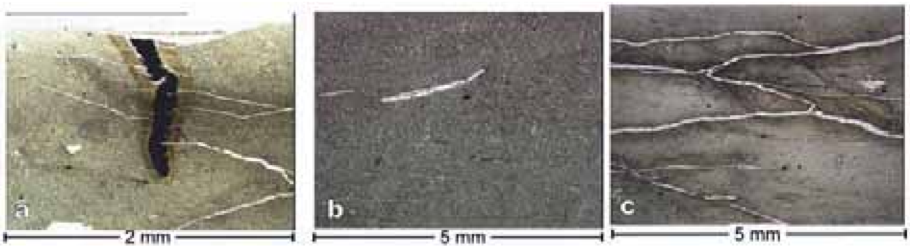

Figure 6.10: **Photomicrographs of thin sections from Opalinus Clay samples. (a) Voids caused by bioturbation are filled with pyrite and rimmed with iron hydroxide, (b) fossil shell fragment, (c) carbonate minerals precipitated on primary tectonic cracks.**

6.2.2 SEM analysis

In Figure 6.11 and Figure 6.12, electron microscopy images of the Opalinus Clay are shown. The overall microstructure of Opalinus Clay is characterized by a wavy arrangement of clay mineral flakes which enclose coarse quartz, feldspar or calcite grains (Figure 6.11a). Figure 6.11b shows disseminated microfossils (diameter 10 – 15 µm) which are enlarged in Figure 6.11e (bedding of fossil) and Figure 6.11f (surface structure of fossil). In Figure 6.11c and Figure 6.11d, fossils arranged parallel to the bedding of the sediment are shown (Figure 6.11c: shell with a thickness of 50 – 80 µm; Figure 6.11d: a bottle-shaped fossil with a length of ≈ 150 µm). Relatively few cracks were observed with the SEM. Pyrite, which according to XRD and S analysis, occurs in the > 20 µm fraction was only found as small crystals filling voids mainly adjacent to microfossils (Figure 6.12). It was often observed that

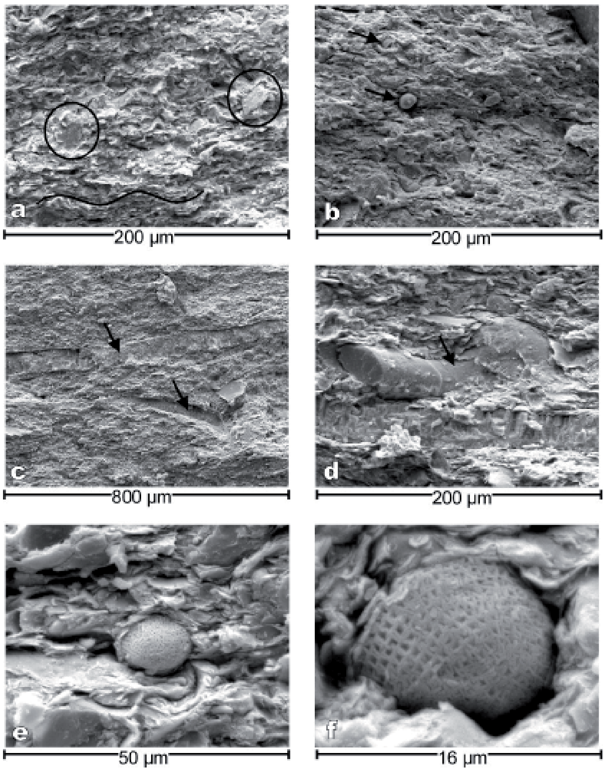

Figure 6.11: **SEM-images of Opalinus Clay (for explanations see text).**

pyrite forms framboids (aggregates of small pyrite crystals), which is probably the reason for the occurrence of pyrite in the > 20 µm fraction.

6.2.3 Summary of microstructural investigations

The microstructural analyses of the Opalinus Clay are summarized in a model that distinguishes between microstructural reasons for brittle behaviour (predetermined breaking planes) and ductile behaviour (possible translation planes):

- The matrix of the Opalinus Clay consists of clay minerals which are arranged sinusoidally (like waves). The clay minerals enclose coarse grains such as feldspar (Fsp), quartz (Qtz), calcite and microfossils.
- Primary cracks (Figure 6.13: red), or cracks formed during drying (Figure 6.13: orange), as well as seashells (Figure 6.13: red), represent predetermined breaking planes. These features are mostly arranged parallel to the bedding.
- Ductile behaviour is likely facilitated by translation planes which are represented by bedding (Figure 6.13: blue) and folding (preferred orientation due to directional stress, Figure 6.13: green).

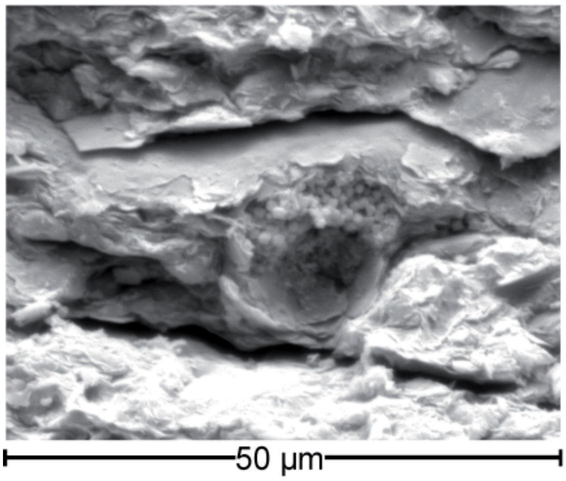

Figure 6.12: **Pyrite crystals (2 µm in diameter) within void around a microfossil that was torn out during sample preparation.**

This model agrees well with the one presented by NAGRA (2002) where silt layers are described additionally.

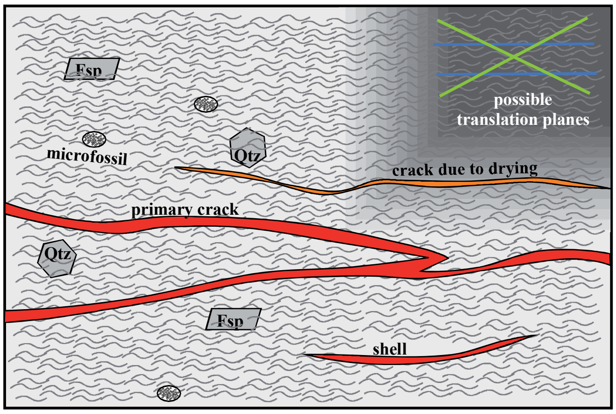

Figure 6.13: **Model of the microstructural features of Opalinus Clay (for explanations see text).**

In conclusion, for the prediction of mechanical behaviour the quantitative determination of cracks or shell fragments by image analysis is recommended. According to the model, directions parallel to bedding and, to a lesser extent, parallel to foliation, facilitate plastic deformation where cracks and shell fragments are absent. While mineral composition probably influences the overall mechanical properties of the formation, the behaviour of individual Opalinus Clay samples appears to be closely linked to their microstructure.

6.3 *Gas content and release*

Within an additional laboratory programme, gas generation and release as a result of temperature effects on Opalinus Clay samples from the unheated and heated area in the test field were determined. The unheated samples were taken in 2001 from borehole BHE 19/2 at a depth of 5.13 to 5.23 m, and in 2003 from the New Gallery (cf.Figure 2.1 and Figure 2.2). The heated samples were taken in 2003 from borehole BHE 26 (0.5 m from the heater borehole) and borehole BHE 27 (1.5 m from the heater borehole), in each case from the levels 2 m to 4 m (above the heater), 4 m to 6 m (heater area) and 6 m to 7 m (below the heater).

For the gas generation and release measurements in the laboratory, glass ampoules with a volume of about 500 ml were used (Figure 6.14). The Opalinus Clay samples were milled to a grain size of less than one millimetre. Via the injection tube of the ampoules, amounts of 1, 10, or 550 grams of Opalinus Clay were introduced, respectively. The gas in the residual volume of the ampoules was either laboratory air or nitrogen. The exposure periods in the oven at a temperature of 95 °C were fixed at 1, 3, 10, 30, 100, 300, and 800 days. For statistical reasons, three replicates of each sample were prepared. After oven exposure for the time given, the ampoules were withdrawn and connected to special equipment for the extraction of the gas from the residual volume. This gas was injected into a gas chromatograph for qualitative and quantitative analyses. The results were converted to the amount of gas per unit mass of clay.

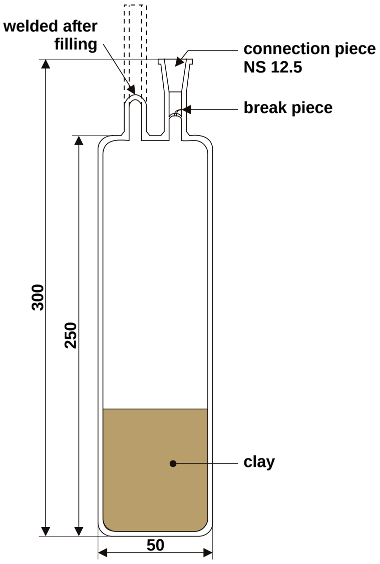

Figure 6.14: Ampoule for the investigation of the generation and release of gases from the clay as a result of elevated temperature.

The investigations indicate that the most important gas generated and released by the thermal decomposition of the organic components in the Opalinus Clay is carbon dioxide. The amount of released hydrocarbons is below 10^{-4} m^3 per 1000 kilogram clay. Figure 6.15 shows the generation and release of carbon dioxide at 95 °C as a function of time for the samples taken from borehole BHE 19/2. It is most likely that carbon dioxide is generated by oxidation of organic material in the clay as its amount is much higher in those ampoules with air in the residual volumes than in those with nitrogen in the residual volumes. Additionally, carbon dioxide may be generated by thermal decomposition of carbonates in the clay.

After 842 days of exposure at a temperature of 95°C, 3.8 m³ carbon dioxide per 1000 kg clay were released in the aerobic and up to 0.43 m³ per 1000 kg clay in the anaerobic stage. The release is not complete after 842 days. It seems that all the organic material will be oxidised if oxygen is available and also the thermally instable carbonate will be decomposed. It should be taken into account that up to 10 m³ carbon dioxide per 1000 kilograms of clay may be released.

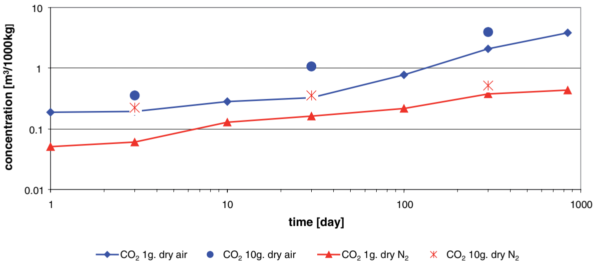

Figure 6.15: Release of carbon dioxide from the Opalinus Clay of borehole BHE 19/2 at 95 °C as a function of time and the amount of clay in the ampoules.

In the course of the laboratory programme, the gas components in the residual gas volume of the vessels used for transport of the heated samples (see section 6.10.1) from BHE 26, BHE 27 and the heater/rock contact zone were quantitatively determined. The results for the gas composition (C_1-C_4 and CO_2) of the untreated samples are given in Figure 6.16. The gas components were measured at 25°C. Carbon dioxide could be detected with concentrations between 2 000 vpm and 20 000 vpm (0.2 to 2.0 vol.%). The concentration of methane ranges between 100 and 500 vpm. For the samples BHE 26/depth 2.03-2.32 m, BHE 26/depth 4.52-4.82 m, BHE 27/depth 2.02-2.32 m and BHE 27/depth 4.15-4.45 m, concentrations between 2 000 and 10 000 vpm were detected. Ethane was measured in all samples with concentrations ranging from 35 to 4 100 vpm. Propane could be detected, but the concentrations were always below 10 vpm. i-Butane was determined in concentrations below 150 vpm except for the samples where methane was determined in higher concentrations. The concentrations in these samples ranged between 500 and 1 700 vpm, see Figure 3.17 on p. 22.

The samples from the heated Opalinus Clay (BHE 26, BHE 27 and the heater/rock contact zone) were exposed to a temperature of 95°C for 10, 100 and 300 days. After the respective exposure time, the generated and released gases were determined. The concentrations of hydrogen, helium and hydrogen sulphide were always below 10 vpm. This corresponds to a maximum gas amount of 0.02 m³ per 1000 kg clay. Concentrations of methane and i-butane were below 30 vpm, which corresponds to 0.02 m³/1000 kg. No significant changes in the gas concentrations could be observed when comparing the gas concentrations after exposure times of 10 and 100 days, respectively. The concentrations of propane ranged from 1 000 to 5 500 vpm after an exposure time of 10 days. A decrease below 10 vpm could be observed for all samples after 100 days. Ethane was not detected after 10 days, but could be observed after 100 days in concentrations below 10 vpm with a gas amount of 0.02 m³/1000 kg.

The concentration of oxygen in the residual volume of the ampoules originally filled with air (20 vol.% oxygen) decreased significantly. This decrease corresponds with the amount of clay in the ampoules: In the ampoules filled with 1 g clay, oxygen concentration decreased to values of less than 7 vol.%. In ampoules filled with 550 g clay, the oxygen concentrations decreased to less than

0.05 vol.%. This indicates that oxygen was consumed by oxidation processes of hydrocarbons. A time-dependent decrease of oxygen for different exposure times could not be observed.

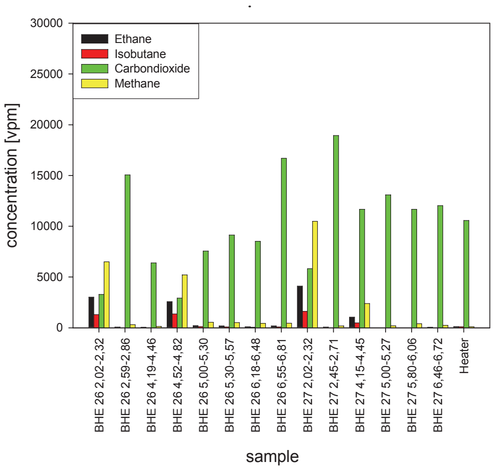

Figure 6.16: Measured gas concentrations for the heated samples of the boreholes BHE 26 and BHE 27 from different depths and from the heater contact zone.

In contrast to the oxygen decrease, the concentration of carbon dioxide increased with increasing amount of clay in the ampoules. CO_2 concentrations between 4.0 vol.% and 6.0 vol.% (40 000 and 60 000 vpm) were found in the ampoules filled with 550 g clay. This corresponds to 6.5 m^3/1000 kg. In general, an increase in CO_2 with exposure time was observed. The concentration of carbon monoxide was about 500 vpm for samples with 10 g clay. Almost no carbon monoxide was found in samples with 550 g clay. The maximum amount of CO was determined to be 0.14 m^3/1000 kg.

In the samples from the heater/rock contact zone, similar concentrations for oxygen were found. In accordance with the measurements in boreholes BHE 26 and BHE 27, the dominant gases released are CO_2 and, to a lesser extent, i-C_3H_8. CO_2 concentrations of 13% (130 000 vpm) were measured in samples with 550 g clay. The maximum amount of CO_2 per mass was determined to be 7.1 m^3/1000 kg.

6.4 Water content, density, and porosity

Porosity is an essential parameter for transport modelling. Usually, the porosity is calculated from bulk and specific density and the investigations of these parameters performed throughout the HE project are therefore summarized and discussed in this section. To determine the degree of saturation, the water content also has to be considered. Therefore, results and problems relating to the determination of the water content are also discussed.

6.4.1 Mineralogical investigations

6.4.1.1 Water content

Water content is usually determined by oven drying at 105°C until a constant weight is reached. The resulting weight loss can be expressed as geotechnical water content

$$w_{\mathrm{G}}\,[\%] \;=\; \frac{m_b - m_s}{m_s} \cdot 100 \qquad (2)$$

where m_b is the weight of the (wet) bulk sample and m_s is the weight of the (solid) dry sample, or as mineralogical water content (weight loss referred to initial weight)

$$w_{\mathrm{Min}}[\%] \;=\; \frac{m_b - m_s}{m_b} \cdot 100 \qquad (3)$$

Clay samples tend to quickly adsorb or desorb water. The in-situ water content of clay is generally of interest. It is determined by taking fresh samples after removing the dried surface. The samples then have to be carefully sealed and analysed in the laboratory as soon as possible. The Opalinus Clay samples analysed for mineralogical composition were treated differently with regard to sealing and transport time. The water content determined at the moment of arrival varied from 4 - 6 wt.%. These values were not considered to be reliable. To be able to compare the water content of all samples, the water content was also determined after equilibration under laboratory conditions (22°C, 45 - 55% relative humidity). The air-drying was monitored for eight days. First, the water content after air-drying at 105, 150 and 200°C was investigated. The steady increase in weight loss due to increased temperature is assumed to be partly caused by the decomposition of organic matter and carbonates. Therefore, these investigations were not continued.

Due to the different history of the samples (drilling, sealing, transport, storage), values with low significance were obtained. The most reliable value (7.0 wt.% mineralogical water content) was obtained by analysing the centre of a drillcore which was carefully sealed and rapidly analysed after sampling. To be able to accurately compare material properties which relate to the water content, the water uptake capacity was determined (see section 6.1.4.4 of the mineralogical analyses).

6.4.1.2 Density

Throughout the mineralogical investigations, the bulk density and the specific density were determined. The bulk density (or envelope density) was determined with a Micromeritics GeoPyc 1360. Instead of a liquid, this pycnometer uses a free-flowing, finely divided dry powder as a fluid medium. The hard, spherical, small particles do not enter pores but envelope the irregular shape of the crushed clay particles. Samples of about 10 to 15 g were used. The bulk (dry) densities are in the range of 2.20 to 2.30 g/cm^3 for the pre-heating samples and 2.19 to 2.29 g/cm^3 for the post-heating samples.

Table 6.9: Specific density depending on grain size and drying, respectively.

sample	T	grain size	spec. dens. [g/cm^3]
Opalinus Clay BPC-C1/29	60°C	coarse (> 1 mm)	2,702
Opalinus Clay BPC-C1/29	105°C	coarse (> 1 mm)	2,706
Opalinus Clay BPC-C1/29	60°C	fine (< 0.25 mm)	2,710
Opalinus Clay BPC-C1/29	105°C	fine (< 0.25 mm)	2,714

The specific density (or absolute or grain density) was determined from samples dried at 105°C for 2 days when no further weight change was observed. The sample weights were about 12 g. The pycnometer used was a helium pycnometer AccuPyc 1330 from Micromeritics. The sample volume is calculated from the observed pressure change undergone by helium when it expands from one chamber containing the sample into another chamber without sample. In the first (pre-heating) investigations, the average specific density was determined to be 2.71 g/cm^3. After the heating period, four additional samples were analysed and an average value of 2.68 g/cm^3 was measured. To determine if this could be an effect of the heating period, the first six samples were analysed again and an average value of 2.68 g/cm^3 was obtained. This suggests that the measuring device caused a constant shift which cannot be explained (possibly ambient conditions). To investigate the reason for this shift, one sample was investigated systematically by varying drying conditions and grain size. From Table 6.9, it can be tentatively concluded that drying and grinding only slightly affects the measurement of the specific density. Therefore, the shift of the measuring device (difference for samples before and after heating: ca. 0.03 g/cm^3) cannot be explained. However, considering the repeated specific density measurements, no difference between samples collected before and after the heating period was found.

For an appropriate assessment of the data, an alternative method for determining the specific density was tested based on the mineralogical composition (Table 6.10). For each mineral, a specific density is assumed based on the data provided by www.webminerals.com. Particularly for 2:1 dioctahedral layered silicates, only a rough estimate is possible. The specific density of illite/muscovite varies from 2.6 to 2.9 g/cm^3 and the specific density of montmorillonite from 2.0 to 2.7 g/cm^3. Based on the determined montmorillonite content (10 - 14 wt.%; part of the illite/smectite mixed layer minerals) as compared with the content of illite/muscovite (ca. 30 wt.%), the specific density of these minerals was estimated. Based on an assumed density of 2.60 g/cm^3 for the 2:1 dioctahedral layered silicates, a specific density of 2.71 g/cm^3 is obtained. The assumption of a specific density of 2.70 g/cm^3 for the 2:1 dioctahedral layered silicates would lead to average values of 2.74 g/cm^3.

In conclusion, the density measurements did not provide any information on the effect of the heating period on the clay. The deviation in the specific density observed throughout the project (2.71 - 2.68 g/cm^3) cannot be explained.

Table 6.10: Calculation of specific density based on the mineralogical composition.

		Samples before heating						Samples after heating			
		BHE 1/6	BHE 1/19	BHE 2/8	BHE 2/21	BHE 3/9	BHE 3/29	BHE 25/6	BHE 25/7	BHE 25/8	BHE 1 0 000
Calcite	[wt.%]	16	18	13	13	14	14	14	14	22	17
spec. density	[g/cm^3]	2.71	2.71	2.71	2.71	2.71	2.71	2.71	2.71	2.71	2.71
Chlorite	[wt.%]	9	7	8	8	8	8	8	8	8	8
spec. density	[g/cm^3]	2.65	2.65	2.65	2.65	2.65	2.65	2.65	2.65	2.65	2.65
Goethite	[wt.%]	2	1	1	2	2	2	2	1	1	1
spec. density	[g/cm^3]	3.8	3.8	3.8	3.8	3.8	3.8	3.8	3.8	3.8	3.8
Gypsum	[wt.%]	1	1	1	1	1	1	1	1	1	1
spec. density	[g/cm^3]	2.3	2.3	2.3	2.3	2.3	2.3	2.3	2.3	2.3	2.3
2:1 dioc. layered silicates (Ill, Smt, Musc.)	[wt.%]	30	31	32	32	32	33	33	33	30	31
spec. density	[g/cm^3]	2.6	2.6	2.6	2.6	2.6	2.6	2.6	2.6	2.6	2.6
K-Feldspar	[wt.%]	3	3	4	4	3	3	3	3	2	3
spec. density	[g/cm^3]	2.56	2.56	2.56	2.56	2.56	2.56	2.56	2.56	2.56	2.56
Kaolinite	[wt.%]	23	20	24	23	23	23	22	22	19	22
spec. density	[g/cm^3]	2.6	2.6	2.6	2.6	2.6	2.6	2.6	2.6	2.6	2.6
Na/Ca-Feldspar	[wt.%]	1	2	1	1	1	1	1	2	1	1
spec. density	[g/cm^3]	2.68	2.68	2.68	2.68	2.68	2.68	2.68	2.68	2.68	2.68
Pyrite	[wt.%]	2	2	2	2	3	2	3	2	2	2
spec. density	[g/cm^3]	5.01	5.01	5.01	5.01	5.01	5.01	5.01	5.01	5.01	5.01
Quartz	[wt.%]	10	12	11	11	10	10	10	10	10	10
spec. density	[g/cm^3]	2.62	2.62	2.62	2.62	2.62	2.62	2.62	2.62	2.62	2.62
Rutile	[wt.%]	1	1	1	1	1	1	1	1	1	1
spec. density	[g/cm^3]	4.25	4.25	4.25	4.25	4.25	4.25	4.25	4.25	4.25	4.25
Siderite	[wt.%]	1	1	1	1	1	1	1	2	2	2
spec. density	[g/cm^3]	3.96	3.96	3.96	3.96	3.96	3.96	3.96	3.96	3.96	3.96
Corg	[wt.%]	1	1	1	1	1	1	1	1	1	1
spec. density	[g/cm^3]	1	1	1	1	1	1	1	1	1	1
specific density calculated	[g/cm^3]	2.71	2.70	2.69	2.70	2.73	2.70	2.73	2.71	2.72	2.71

6.4.1.3 Porosity

The porosity can be calculated either by considering the specific density and the water ratio or by using the bulk and specific density, eqn. (1). The porosity determined during the mineralogical investigations was obtained using the Micromeritics GeoPyc1360 device which measures the bulk density (additional input: weight, specific density) and uses eqn. (1). Slight differences between the porosity calculated by considering the single values and the values obtained from the Micromeritics AccuPyc 1330 are probably caused by rounding errors. In conclusion, the porosity of the Opalinus Clay is 14 - 18% (mean value ca. 15.5%) and no systematic differences caused by the heating period were found.

6.4.2 Geotechnical investigations

Before applying the strength tests (see section 6.5), bulk wet densities ρ

$$\rho = \frac{m_b}{V} \qquad (4)$$

and geotechnical water ratios w_{GT}, equation (2), were determined. This was done by weighing and measuring the geometry of the samples to determine the density and by heating the samples at 105 °C until a constant weight was reached for the determination of the geotechnical water ratio.

More than a year passed between the pre-heating sampling from boreholes BHE-B1, BHE-B2 and BHE-B3 at the Mont Terri site and the strength tests in the BGR laboratories. During this time, the sealing of the samples with aluminium-coated plastic films, after sucking out air to create a partial vacuum, often breached. Fissuring due to unloading and drying was initiated. Furthermore, the samples could not be cut to size very precisely and small break-outs on the surface of the samples occurred. During the slow hydrostatic loading at the beginning of the strength tests, compaction of up to 9 mm was observed.

The mean density of uncompacted samples from boreholes BHE-B1, BHE-B2 and BHE-B3 was 2.38 g/cm^3, with a range of 2.26 to 2.45 g/cm^3. For compacted samples, it was 2.41 g/cm^3 with a range of 2.29 to 2.47 g/cm^3. The mean value of the geotechnical water ratio was 6.80% with a range of 5.00 to 8.36%. Determining the geotechnical water ratio by drying, specimens from the same sample and with different net weights showed differences in the water ratio of up to 6%. There was no correlation of the geotechnical water ratio and the storage time or the state of the sealing (i.e. failed or intact), indicating that - at least partially - the natural scatter of the geotechnical water ratio was observed in its in-situ state.

Investigations on samples from borehole BHE-B25 (post-heating sampling) were performed soon after drilling. They produced densities of 2.43 g/cm^3 and geotechnical water ratios in the range of 6.95 to 7.33%.

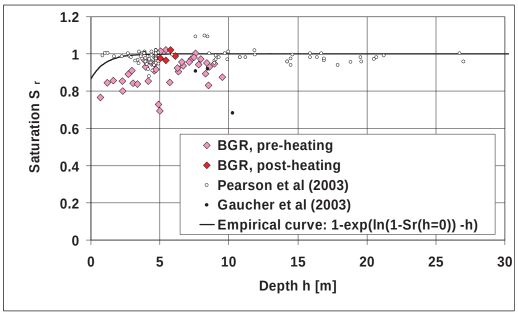

Figure 6.17: Depth-dependence of the saturation determined from samples in the HE vertical boreholes and boreholes in the vicinity. Empirical curve with – ln(1-S_r(h=0)) = 2 leads to a saturation at the surface of S_r(h=0) = 0.86 which matches with the results of numerical calculations for the niche surface (see chapter 7, p. 76ff).

6.4.3 Summary

In Table 6.11, results for Opalinus Clay properties from the HE experiment are compared with data from the literature. In the case of the HE results, the densities ρ, ρ_s, and ρ_d and the geotechnical water ratio w have been measured. Porosity n, equation (1), and saturation S_r

$$S_r = \frac{w \cdot \rho_d}{n \cdot \rho_w} \qquad (5)$$

have been calculated. The water density ρ_w is the density of Pearson water, ρ_w = 1.019716 g/cm^3 (Pearson et al. 1999). The data from the literature quoted in Table 6.11 have, in most cases, been derived or estimated. Results for the HE experiment lie in the range of other experimental findings. Figure 6.17 shows the degree of saturation as a function of depth. Data from the pre-heating phase of the HE experiment clearly show that extensive dehydration of the samples must have taken place before the measurements. On the other hand, results from the post-heating phase show good agreement with results from the literature. The water content of samples from the pre- and post-heating phases is more or less identical. This supports the results of geoelectric measurements that found no decrease in water content in the heated zone. As numerical simulations show (cf. chapter 7), the gradient of saturation over depth is very steep in boreholes. Figure 6.17 shows a gradient in the HE niche according to numerical simulation that is much flatter. In any case, the saturation profile over depth could not be determined experimentally, firstly due to the poor quality of the pre-heating phase samples and, secondly, due to the lack of data from the post-heating phase.

Table 6.11: Parameters determined in the pre- and post-heating phases of the HE project compared with data from the literature, given as mean values and standard deviation.

Parameter	Pre-heating	Post-heating	PEARSON et al. (2003) GAUCHER et al. (2003)
Bulk (wet) density ρ, g/cm^3	2.41 ± 0.04	2.43 ± 0.01	2.47 ± 0.05 2.46 ± 0.03
Bulk (dry) density ρ_b, g/cm^3	2.27 ± 0.03	2.25 ± 0.04	2.31 ± 0.07 2.31 ± 0.02
Specific density ρ_s, g/cm^3	2.71 ± 0.01	2.69 ± 0.01	2.75 ± 0.01 2.73 ± 0.03
Geotechnical water ratio w, %	6.80 ± 0.62	7.08 ± 0.18	7.05 ± 1.40 6.40 ± 1.04
Porosity, n	16.68 ± 1.92	15.81 ± 0.19	18.04 ± 12.92 15.32 ± 1.55
Saturation, S_r	0.90 ± 0.08	0.99 ± 0.02	0.99 ± 0.03 0.95 ± 0.16

6.5 Laboratory tests for characterizing THM properties

6.5.1 Introduction

In order to characterize various aspects of the thermo-hydro-mechanical behaviour of Opalinus Clay required for THM modelling, laboratory tests were performed at the UPC Geotechnical Laboratory. The following tests were performed: water retention, thermal expansion, saturated and unsaturated hydraulic conductivity and uniaxial compression tests.

6.5.2 Water retention curve

Small rock specimens, 25x25x10 mm, were equilibrated in hermetic containers at a specified relative humidity using a vapour equilibrium technique. The relative humidity (RH) of the air in the container was related to the total suction in the specimens by means of the psychrometric law (FREDLUND & RAHARDJO 1993):

$$RH = e^{\left[-\frac{s \cdot M_w}{R \cdot T \cdot \rho_l}\right]} \quad \text{and} \quad s = -\frac{R \cdot T}{M_w}\rho_l \ln(HR) \qquad (6)$$

where s is the total suction, M_w the molecular mass of water, R the universal gas constant, T the absolute temperature and ρ_l the water density at temperature T. Suction was applied by means of sodium chloride and sulphuric acid solutions with different concentrations. Drying and wetting paths were performed with specimens obtained from borehole BHE-8 from depths of 6.40 to 7.30 m. The measured values for bulk density, dry density, water content and degree of saturation of these specimens were 2.39 g/cm^3, 2.24 g/cm^3, 6.67 % and 0.82, respectively, which is comparable with other results in the HE experiment, cf. section 6.4.

At the high suction range ($S_r < 0.2$), the Van Genuchten model is not able to adjust the measurements correctly. In order to increase its range of applicability, it is convenient to use a modification of the Van Genuchten function, more suitable for higher values of suction ($S_r < 0.2$) (Villar 2002):

$$S_e = \frac{S_l - S_{rl}}{S_{ls} - S_{rl}} = \left(1 + \left(\frac{P_g - P_l}{P}\right)^{\frac{1}{1-\lambda}}\right)^{-\lambda} \left(1 - \frac{P_g - P_l}{P_s}\right)^{\lambda_s} \qquad (7)$$

where P_s and λ_s are two new material parameters. The parameter values obtained by fitting the measured water retention curve are shown in Table 6.12. Figure 6.18 shows the water retention curves in both drying and wetting paths in terms of the degree of saturation.

6.5.3 Thermal expansion

Samples were subjected to heating-cooling cycles ranging from 22ºC to 65ºC. The test equipment was constructed following the ASTM D4535-85 standard (UPC-DIT (TD) 1999). Figure 6.19 shows the equipment in schematic form. Three samples named T1, T2 and T3 were extracted from borehole BH8-1 from 6.00 m depth. These samples show bedding planes inclined between 65º and 70º with respect to the borehole axis. Sample T1 underwent heating and cooling cycles in the range of 22ºC to 65ºC. This sample was tested with a water content of w = 5.67%. Figure 6.20 shows the evolution of temperature and vertical strain with time, respectively. Figure 6.21 shows the vertical strain of expansion with temperature. Similar tests were performed on samples T2 and T3.

Table 6.12: Parameters of the Van Genuchten model which fit the water retention curve of Opalinus Clay in a wetting and drying path.

Parameter	Drying Path	Wetting Path
P [MPa]	8.12	8.60
λ	0.19	0.32
P_s [MPa]	700	700
λ_s	2.38	0.66

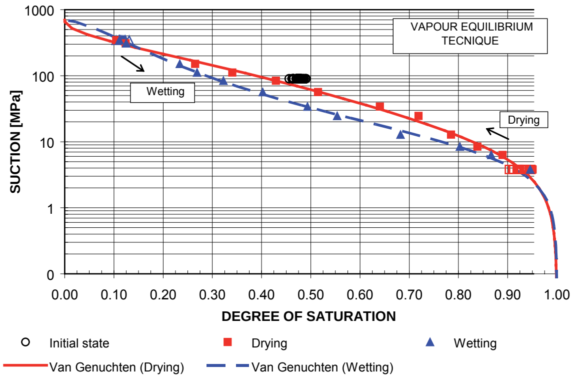

Figure 6.18: Water retention curve in terms of suction and degree of saturation in drying and wetting paths.

Changes in temperature were applied slowly at a rate of 2ºC per hour during heating and 1ºC per hour during cooling. Irreversible strains accumulate in each cycle. For a constant temperature of 65ºC, the vertical strain continues to increase. The values for the linear thermal expansion coefficient (α) were obtained from the relationships between vertical strain and temperature. Measured values range between 0.00008 and 0.00014 (1/ºC).

In comparison, values for the linear thermal expansion coefficient for different types of rocks are: $\alpha = 2.8 \cdot 10^{-06}$ [1/ºC] for granite (Keusen et al. 1989) and $\alpha = 4.0 \cdot 10^{-05}$ [1/ºC] for salt (Janssen et al. 1984).

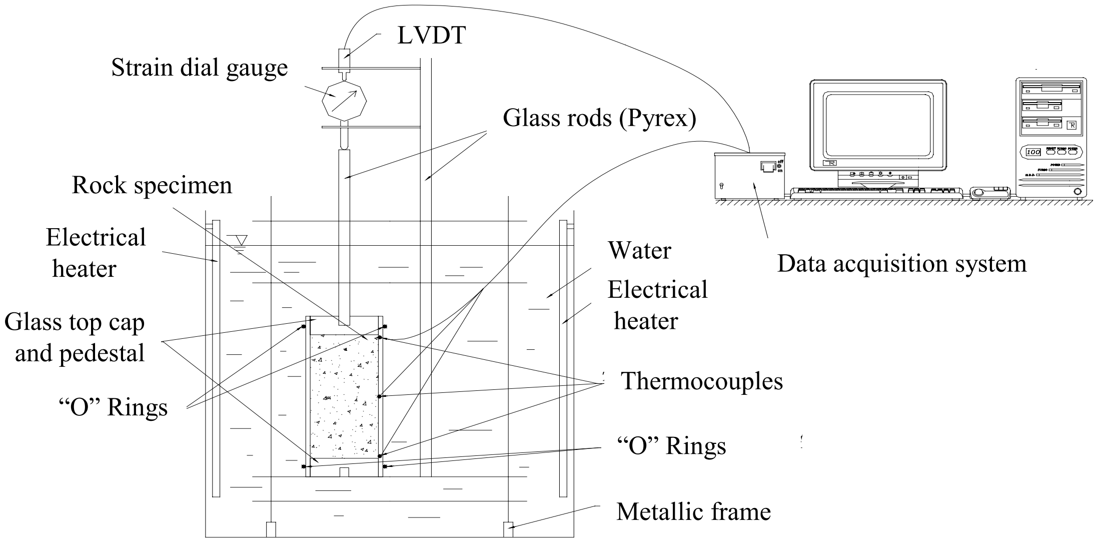

Figure 6.19: Equipment for carrying out the thermal linear expansion test.

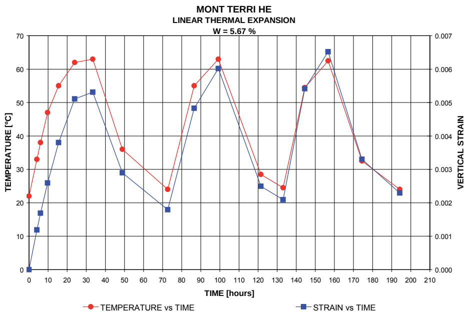

Figure 6.20: Time evolution of temperature and vertical strain during heating and cooling cycles performed in sample T1. Water content w = 5.67%.

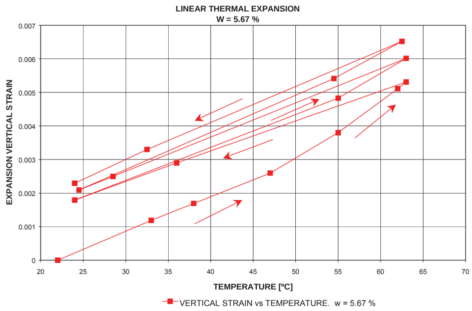

Figure 6.21: Expansion vertical strain versus temperature during heating and cooling cycles in sample T1. Water content w = 5.67%.

6.5.4 Uniaxial compression tests

Uniaxial compression tests were carried out on three cores of Opalinus Clay to determine Young's modulus and Poisson's ratio at different water contents. The samples were extracted from borehole BHE-8 at 7.00, 7.50 and 9.00 m depth. Due to their size, it was necessary to have an air flow through the dissolution and desiccator vessel to reduce the time needed to reach equilibrium. Samples were named C1, C2 and C3, and their size, applied suctions, water contents and degree of saturation are shown in Table 6.13. Samples show stratification planes inclined from 65º to 70º with respect to the longitudinal axis. The failure was brittle and took place in a plane dipping between 40º and 43º with respect to the longitudinal axis. Longitudinal strains were measured using strain gauges and displacement transducers (LVDT). Radial strains were measured using strain gauges. In Figure 6.24, the longitudinal and transversal stress-strain behaviour is represented for the three samples. In Table 6.14, the values obtained for Young's modulus and Poisson's ratio are presented for the samples tested at different water contents.

6.5.5 Hydraulic conductivity (saturated and unsaturated)

Permeability tests at constant pressure were carried out on four samples extracted from borehole BHE-8 at 6.00, 6.30, 6.60 and 8.60 m depth. Samples tested were 50 mm high and 72 mm in diameter. The samples show stratification planes inclined from 65º to 70º with respect to the borehole longitudinal axis. They were cut and dried using the vapour equilibrium technique to reach a degree of saturation of $S_r = 36\%$. It took 5 weeks to reach equilibrium. In order to carry out the test, permeameters made of stainless steel, 75 mm in diameter, were constructed (Figure 6.22). Water enters through the bottom of the sample at a pressure of 0.5 MPa and exits the sample through the top at atmospheric pressure. The pressure is applied using a mercury column system. PEARSON (1998) water was used in the test. Samples P1, P2 and P3 were used to observe the water content distribution vs. time and to determine the unsaturated permeability of the rock. These samples were tested at different infiltration times: 4, 10, and 25 days. Once the time predetermined for each sample had expired, they were extracted from the ring using a circular saw and cut into slices of approximately 10 mm thickness to determine their water content. The hydraulic conductivity under saturated conditions was determined applying Darcy's law. The value obtained is $K = 1.33 \cdot 10^{-13}$ m/s and the intrinsic permeability $k = 1.35 \cdot 10^{-20}$ m^2. Saturated permeability values of $K = 4.89 \cdot 10^{-14}$ m/s were obtained previously by PASQUIOU & ROBINET (1997) and values ranging from $K = 5.0 \cdot 10^{-13}$ to $0.1 \cdot 10^{-13}$ m/s were reported by BOCK (2001).

Table 6.13: Size, suctions, water contents and degrees of saturation for test samples C1, C2 and C3.

Sample	Water content	Young's modulus	Poisson's ratio	σ_{failure}
	[%]	[MPa]		[MPa]
C1	3.22	2000	0.216	12.72
C2	4.45	350	-	9.65
C3	5.94	2000	0.262	18.82

Table 6.14: Values for Young's modulus and Poisson's ratio obtained in uniaxial compression tests.

Sample	Diameter	Length	Suction	HR	*w*	Sr
	[mm]	[mm]	[MPa]	[%]	[%]	[%]
C1	72	143.3	70.0	60.0	3.22	40.0
C2	72	146.5	30.0	80.0	4.45	55.0
C3	72	145.0	15.0	90.0	5.94	73.0

The hydraulic conductivity under unsaturated conditions k_{rl} was obtained by back-analysis performed with the finite element programme CODE_BRIGHT. The numerical simulation reproduces the tests carried out. The relative permeability law of the liquid phase is expressed using the Van Genuchten model as follows:

$$k_{rl} = \sqrt{S_e}\left(1-\left(1-S_e^{1/\lambda}\right)^{\lambda}\right)^2 \qquad (8)$$

The values obtained are: $S_{rl} = 0.00$, $S_{ls} = 1.00$, $0 \leq Se \leq 1$, $\lambda = 0.29$. The parameters used in the numerical model are shown in Table 6.15 and were obtained previously in laboratory tests. Figure 6.23 shows the distribution of the measured water content with the height of samples and the comparison with the results obtained from the numerical simulation in the samples P1, P2 and P3. Figure 6.25 shows the water volume infiltrated with the time in samples P1 to P4. Measured and calculated values are indicated.

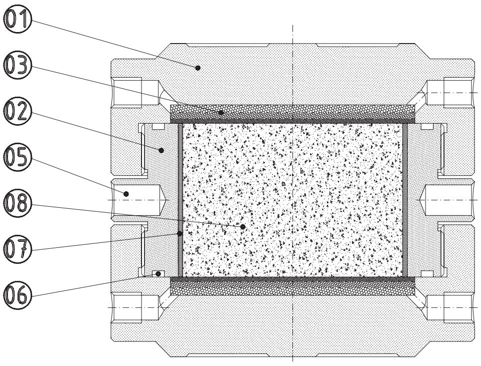

01	Top Cap
02	Metallic Ring
03	Porous filter
05	Adjusting handles
06	“O”-rings
07	Resin seal
08	Sample

Figure 6.22: **Scheme of permeameter for performing permeability test.**

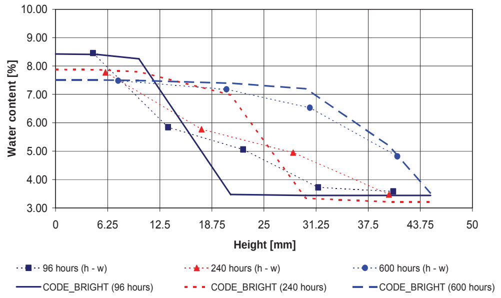

Figure 6.23: **Water content distribution in the samples tested. Samples P1, P2 and P3 were tested at 4, 10 and 25 days respectively. The figure also shows the water content distribution obtained from the numerical simulation.**

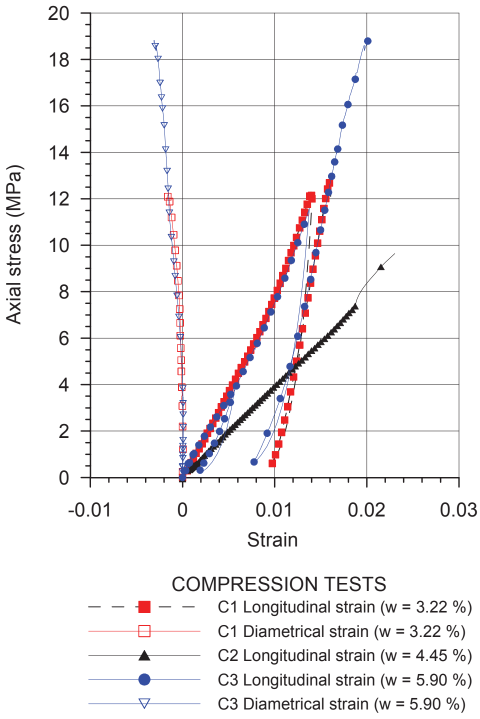

Figure 6.24: Stress-strain curves for samples C1, C2 and C3. The marked similarity in stress-strain behaviour between samples C1 and C3 is clear, while the behaviour of C2 is significantly different.

Table 6.15: Hydromechanical parameters used in the numerical model.

Properties	Value
Intrinsic permeability **k** (Kozeny model)	$k = k_0 \dfrac{\phi^3}{(1-\phi)^2} \dfrac{(1-\phi_0)^2}{\phi_0{}^3}$ ϕ_0: reference porosity (0.175) k_0: intrinsic permeability for matrix ($1.35 \cdot 10^{-20}$) [m^2]
Retention curve (modified Van Genuchten model)	$S_e = \dfrac{S_l - S_{rl}}{S_{ls} - S_{rl}} = \left(1 + \left(\dfrac{P_g - P_l}{P}\right)^{\frac{1}{1-\lambda}}\right)^{-\lambda} \left(1 - \dfrac{P_g - P_l}{P_s}\right)^{\lambda_s}$ S_e: Effective saturation ($0 \le S_e \le 1$) P : Material parameter (8.60) [MPa] λ : Shape function for retention curve (0.32) P_s: Material parameter (700.00) [MPa] λ_s: (0.66) S_{rl}: Residual saturation (0.00) S_{ls}: Maximum saturation (1.00)
Relative permeability $\mathbf{k_{rl}}$ (Van Genuchten model)	$k_{rl} = \sqrt{S_e}\left(1 - \left(1 - S_e{}^{1/\lambda}\right)^{\lambda}\right)^2$ S_e: Effective saturation ($0 \le S_e \le 1$) λ : Power (0.29) S_{rl}: Residual saturation (0.00) S_{ls}: Maximum saturation (1.00)
Porosity	(0.175)
Initial suction	(52.00) [MPa]

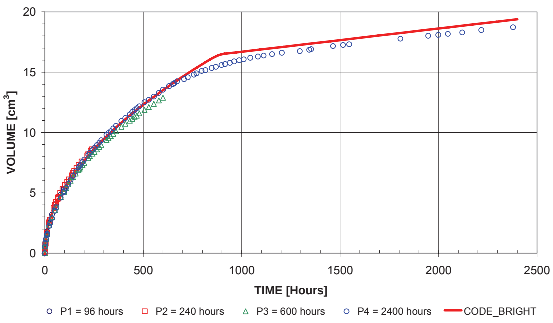

Figure 6.25: Water volume infiltrated on real time scale. The figure shows that the numerical model properly reproduces the test values

6.6 Rock mechanics analysis and geotechnical measurements I

A total of 43 cylindrical rock samples were tested for strength by triaxial compression tests and indirect tensile tests. The samples came from boreholes BHE-B1, BHE-B2 and BHE-B3, which were drilled before the heater experiment was started, and BHE-25, which was drilled after heating and was located close to the heater. From measurements and calculations, it can be concluded that the samples from BHE-25 were heated up during the experiment to about 40 to 60°C. The rock samples had different orientations of the bedding to the sample axis. This gives rise to three sample types:

- p-sample = bedding parallel to the axis (BHE-B1),
- s-sample = bedding normal to the axis (BHE-B2), and
- z-sample = bedding oblique (approx. 45°) to the axis (BHE-B3, BHE-25).

The quality of the samples from BHE-B1, BHE-B2 and BHE-B3 was poor (see section 6.4.2), while for BHE-B25 it was good. Special emphasis was placed on changes in failure strength and in post-failure stresses as a result of temperature histories. Apart from reference tests at room temperature (RT), samples were heated to 80 °C or 120 °C and cooled down again before the strength tests started, thus simulating the heater test on a short timescale of one to three days. The samples were tested under undrained conditions and in an unsaturated state as desaturation had occurred on the way from drilling to installation in the testing device.

Although there seems to be an influence of temperature on the failure strength, with a tendency towards increased strength with increased temperature, this influence is not significant compared to the impact of structural and perhaps mineralogical variations in the specimens. p-samples and some of the s-samples have the highest failure strengths; a sub-group of s-samples is weaker in failure and differences in the mineralogical composition of the samples are assumed as the reason for this divergence within one sample group. Lowest failure strengths are attributed to z-samples. In post-failure mode, this ranking is still present, but only of minor importance. In Figure 6.26, the results for failure strength are shown, including the values for the post-heating samples from borehole BHE-25. As the dip of the bedding planes of the latter samples is 35° to the sample axis, they can be compared with z-samples. The strength results are in the upper range of pre-dismantling z-samples. An obvious influence of heating for a period of 1½ years cannot be detected.

12 samples were tested using Brazilian tests (i.e. indirect tensile tests) with a deformation rate of 0.06 mm/min and at room temperature. The tensile strength ranges from 0.4 to 2.2 MPa depending on the orientation of the bedding planes to the acting force: low strength was found in tests where the load is parallel to the bedding plane. High strength correlates with loads acting perpendicular to the bedding.

To describe failure and post-failure behaviour, the Mohr-Coulomb criterion

$$\tau = \sigma \tan\varphi + c \qquad (9)$$

was used, where τ is the shear stress [MPa], σ the normal stress [MPa], φ the internal friction angle [°] and c the cohesion [MPa]. A bi-linear regression seems to be appropriate to fit the data points, with a first section (area of validity) of steeper rise and a second of lower rise. A linear regression was done in those cases where insufficient data points were available. In post-failure, cohesion at a confining pressure of zero should be zero. Small cohesion values up to about 0.5 MPa in post-failure are acceptable in linear regression. Table 6.16 contains the Mohr-Coulomb values which are proposed on the basis of the laboratory investigations.

Table 6.16: Mohr-Coulomb parameters derived from laboratory strength tests.

Sample type	Internal friction angle φ [°]	Cohesion c [MPa]	Correlation coefficient	Regression type	Area of validity σ [MPa]
p – preheat., failure	40.5	1.42	0.9895	linear	all
s – preheat., failure, low	38.7 12.2	2.30 5.11	0.9999 0.9327	bi linear	< 4.8 ≥ 4.8
z – preheat., failure	30.6 16.6	1.01 2.54	0.9975 0.9996	bi linear	< 5.2 ≥ 5.2
~z – postheat., failure	20.6	2.27	0.9863	linear	all
p – preheat., post failure	30.1	0.58	0.9816	linear	all
s – preheat., post failure, high	41.6 23.4	0.14 2.10	0.9969 0.9983	bi linear	< 4.3 ≥ 4.3
s – preheat., post failure, low	32.2 8.1	0.15 3.90	0.9941 0.9515	bi linear	< 7.7 ≥ 7.7
z – preheat., post failure	30.8 3.45	0.14 3.67	0.9944 0.6159	bi linear	< 6.6 ≥ 6.6
~z – postheat., post failure	31.6 15.2	0.10 1.57	0.9940 0.9852	bi linear	< 4.3 ≥ 4.3

As deformation parameters, the tangent modulus E_v, Young's modulus E and residual deformation modulus RVM in the post-failure phase were evaluated for the different sample types (i.e. p, s, $z_{preheating}$ and $z_{postheating}$), Table 6.17. Samples orientated parallel to the bedding have the highest deformation parameters, while samples with an orientation perpendicular or oblique to the bedding have lower values, although in the same range, with the exception of the E-values from the post-heating samples which show an additional decrease of about 30%. Figure 6.27 shows Young's modulus for the pre-heating tests. Within the same sample type, a very slight trend towards higher values correlated with increasing depth within the boreholes can be observed, although the scatter is considerable. Temperature histories seem to have no influence on the results.

In situ measurements of rock deformability were performed in the post-dismantling phase of the HE experiment in boreholes BHE-24 to BHE-27. Using dilatometer tests, the deformation modulus E_{vdil} during loading and the modulus of elasticity E_{dil} during unloading were determined (Figure 6.27). Two trends were found: the deeper the position of a test in a given borehole, and the larger the distance of a tested borehole from the heater, the higher were the moduli. Borehole BHE-24 does not fit this trend; this may be explained by the quality of the drilling or the rock, because the drillcores were highly fragmented. No anisotropy was found within the boreholes, but from other tests it is known that different orientations of boreholes to the bedding plane reveal different E_{vdil} and E_{dil} values, with 1700 MPa (E_{vdil}) and 7000 MPa (E_{dil}) for boreholes perpendicular to the bedding and 1200 MPa (E_{vdil}) and 2300 to 3700 MPa (E_{dil}) for boreholes parallel to the bedding.

The laboratory tests and dilatometer tests give comparable results for the tangent modulus, the deformation modulus and Young's modulus. With the exception of the tangent modulus of p-samples, the laboratory results are in the same range as the in situ measurements, tending to the upper range of values. The values of the E moduli indicate, to a large extent, intact rock at the position of the dilatometer tests.

Table 6.17: Deformation parameters determined from laboratory strength tests.

Sample type	E_v [MPa]	E [MPa]	RVM [MPa]
p	4350 ± 569	7950 ± 1922	3650
s	1320 ± 558	3014 ± 965	1500 ± 374
z–preheat.	1244 ± 325	3533 ± 1333	1441 ± 432
~z–postheat.	1300 ± 460	2338 ± 165	1412 ± 492

The linear thermal expansion coefficient α was deduced from heating and cooling of the samples in laboratory tests. Thermal deformation was superimposed by continuing compaction under hydrostatic pressure, thus underestimating the coefficients during heating and overestimating them during cooling. The mean values show a dependence of the thermal expansion coefficient on the bedding direction. Mean values during heating are $1.46 \cdot 10^{-5}$/K (p-sample), $3.49 \cdot 10^{-5}$/K (z-sample) and $5.13 \cdot 10^{-5}$/K (s-sample).

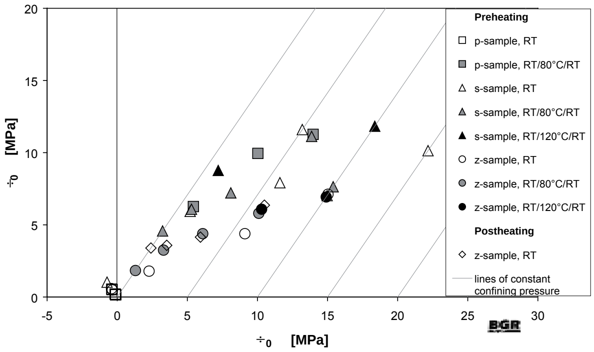

Figure 6.26: Failure strength of samples from the BHE boreholes.

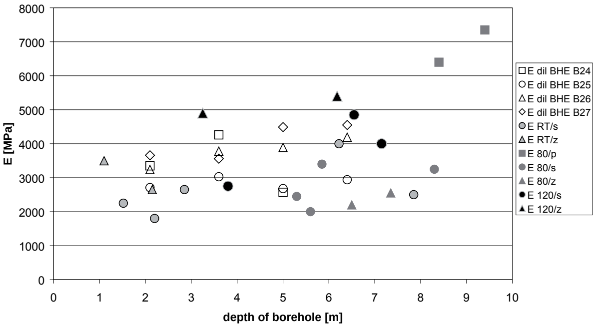

Figure 6.27: Laboratory and in situ Young's modulus.

6.7 *Rock mechanics analysis and geotechnical measurements II*

6.7.1 Introduction

A laboratory testing programme using cubic samples in a true triaxial cell was conducted to determine the dependence of mechanical properties of the Opalinus Clay on temperature and to investigate changes induced by thermal loading. Experiments at elevated temperature levels up to 105 °C, and at room temperature for comparison purposes, were carried out. Special emphasis was placed on anisotropic effects due to the bedding of the Opalinus Clay.

6.7.2 Experimental conditions

6.7.2.1 Samples

The samples for laboratory tests were taken from the well-preserved core material of borehole BLT-1. The material from BLT-1 was regarded as a suitable substitute for badly preserved cores available from the HE-area, because BLT-1 cores show a similar mineralogical composition ("shaly facies"). The thermal loading of the HE boreholes was insignificant and post-heating specimens from the HE area have not been investigated.

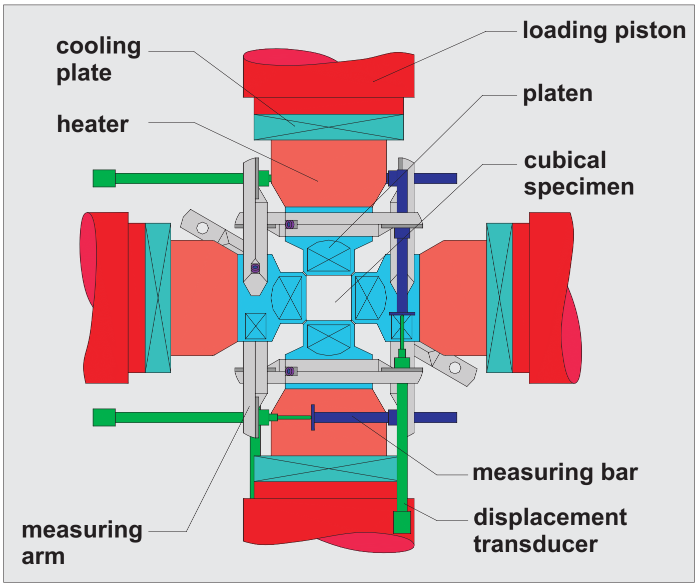

Figure 6.28: Scheme of true triaxial testing apparatus.

The mineralogical and petrophysical properties of the samples investigated were all very uniform. The core samples were prepared into cubic specimens of 53 mm edge length for the subsequent true triaxial experiments.

6.7.2.2 Apparatus

A true triaxial apparatus for cubic samples was used to measure the deformations and the strength of the Opalinus Clay specimens (Figure 6.28).

During the tests, the applied principal stresses can be controlled independently for each of the three orthogonal axes. Heater elements and cooling plates allow controlled temperatures up to 300 °C.

The true triaxial experiments were set up to determine the presumably anisotropic thermal expansion behaviour, the strength and the elastic properties of the Opalinus Clay. Nine experiments were carried out at elevated temperature levels up to 105 °C, while five more tests were performed at room temperature to assess the influence of temperature.

6.7.3 Procedure

6.7.3.1 Thermal expansion

The specimens were loaded isostatically ($\sigma_{13} = \sigma_{24} = \sigma_{56}$) to a mean stress level of 15 MPa to suppress sample disturbances caused by drilling, transport and preparation processes. The samples were then heated with an average heating rate of 15 K/h to the projected temperature levels. The temperature remained constant for sufficient time to ensure a homogeneous temperature distribution throughout the sample, followed by the next heating step. Sample deformations were measured in intervals from 25 °C to 55 °C to 80 °C, and finally to 105 °C. After the highest temperature level was reached, the mean stress was reduced to about 0.4 MPa, and the samples were allowed to cool down slowly from 105 °C to 25 °C, which took about 15 hours.

6.7.3.2 Strength

The failure strength in compression was determined on eight specimens, four at room temperature and four at 80 °C. The mean stress was raised isostatically to the desired level (at a stress rate of $\dot{\sigma}$ = 0.8 MPa/min). Then, while keeping the mean stress constant, the octahedral shear stress was increased with a constant loading rate of $\dot{\tau}_{oct}$ = 0.6 MPa/min until sample failure occurred (Lode parameter m = -1).

6.7.3.3 Elasticity

Starting from isostatic loading conditions, two stresses were kept constant while the third principal stress was reduced at an unloading rate of 4 - 11 MPa/min to determine the anisotropic elastic properties. Four extensive experiments covered multiple mechanical (σ_{mean} = 10 - 30 MPa) and thermal loading conditions (25 - 105 °C). All components of the transversely isotropic elasticity tensor except the independent shear modulus were directly deduced from each single specimen. This is different from conventional testing that requires the combination of data from at least two samples with different orientation.

6.7.4 Results and discussion

6.7.4.1 Thermal expansion

The linear thermal expansion coefficients turned out to be clearly anisotropic. In general, lower values were measured parallel to the bedding planes than perpendicular to them. The results derived from the cooling phase seemed to be more reliable than those from the heating phase due to the slow temperature decrease leading to better equilibrium conditions in the sample and due to the stress state (cooling: σ_{mean} = 0.4 MPa vs. heating: σ_{mean} = 15 MPa) being closer to the in-situ conditions. Therefore average values for the thermal expansion coefficient of

$\alpha_{\parallel} = 1.2 \cdot 10^{-5}\ K^{-1}$ parallel and

$\alpha_{\perp} = 2.5 \cdot 10^{-5}\ \mathrm{K}^{-1}$ normal to the bedding

are suggested. A less pronounced anisotropy was measured while heating the specimens

$\alpha_{\parallel} = 1.4 \cdot 10^{-5}\ \mathrm{K}^{-1}$ and

$\alpha_{\perp} = 1.8 \cdot 10^{-5}\ \mathrm{K}^{-1}$.

Further investigations are needed to clarify the dependence of the expansion coefficient, e.g. on the acting stress.

6.7.4.2 Strength

The failure strength of Opalinus Clay was found to be strongly dependent on the mean stress and on the orientation of the maximum principal stress with regard to the bedding, while the dependence on temperature remained weak. As already known from previous investigations, the shear stress at failure increased with higher mean stress. A distinct strength anisotropy was observed, since samples loaded parallel to the bedding planes showed higher failure strengths than samples loaded normal to the bedding (Figure 6.29). The anisotropic behaviour was even more pronounced at higher mean stresses (Figure 6.29). The specimens subjected to a higher temperature (80 °C) showed higher failure strengths for the same mean stress and orientation conditions (Figure 6.29). This suggests increasing failure strengths with increasing temperature, an observation that requires further research. However, the impact of the strength anisotropy due to bedding and mean stress was much more significant for the failure strength than the influence of temperature.

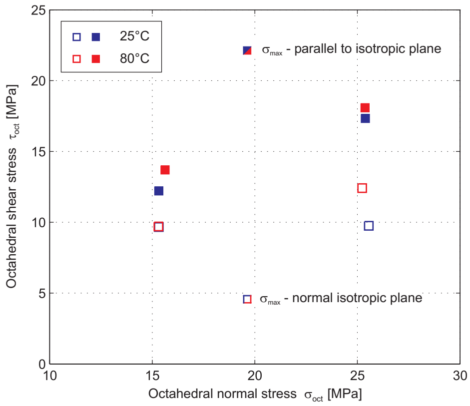

Figure 6.29: Failure strength of Opalinus Clay as a function of mean stress (σ_{oct}), orientation of the maximum principal stress with regard to the isotropic plane (bedding) and temperature.

6.7.4.3 Elasticity

The validity of the transversely isotropic approach for Opalinus Clay was manifested in the observed deformation behaviour. The elastic properties obtained from fast unloading cycles represent undrained parameters. The ratio between the moduli in the principal directions was on average 1.8, reflecting a relatively high degree of anisotropy. In general, the modulus perpendicular to the bedding planes was considerably smaller than parallel to them (Figure 6.30). Both moduli were strongly dependent on the mean stress (Figure 6.30). Examination of the Poisson's ratios yielded smaller values within the isotropic plane rather than perpendicular to it (Figure 6.31). However, the data showed fairly large scatter. The Poisson's ratios tended to increase with the mean stress (Figure 6.31). The remaining independent shear modulus G_2 of a transversely isotropic model was estimated from the known set of elastic parameters using St. Venant's empirical relationship:

$$\frac{1}{G_2} = \frac{1}{E_1} + \frac{1}{E_2} + 2\frac{\nu_2}{E_2} \qquad (10)$$

to complete the elastic compliance tensor. Its application yielded for the shear modulus G_2 = 3.9 - 5.5 GPa, depending on the mean stress.

In a second step, the influence of temperature on the elastic properties was analyzed. The experimental results showed a slight increase with increasing temperature for the modulus normal to the bedding. The behaviour of the modulus parallel to the bedding was inconsistent: after an initial reduction, it also increased slightly with increasing temperature. Concerning the Poisson's ratios, no obvious correlation to the temperature was noticed. In conclusion, there seems to be only a very weak dependence of the elastic properties on temperature, much less pronounced than the influence of stress.

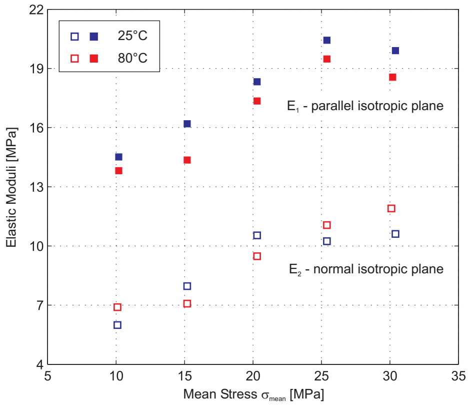

Figure 6.30: **Elastic moduli normal and parallel to the isotropic plane (bedding of the argillite) as a function of mean stress (σ_{mean}) and temperature.**

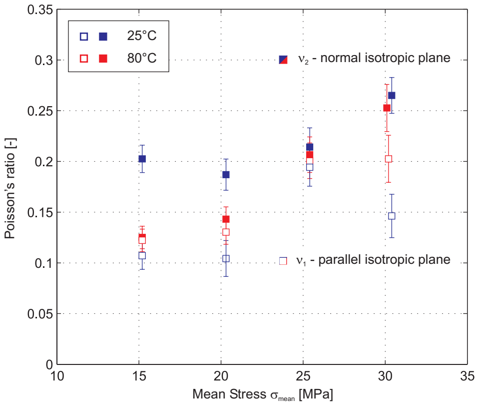

Figure 6.31: **Poisson's ratios normal and parallel to the isotropic plane (bedding of the argillite) as a function of mean stress (σ_{mean}) and temperature.**

6.8 In-situ seismic investigations

Seismic interval velocity and cross-hole measurements were performed along and between five vertical boreholes in the floor of the HE niche. The investigations were aimed at the characterization of the excavation damaged/disturbed zone (EDZ/EdZ), as well as at the detection of changes in seismic parameters due to the influence of the heater element on the surrounding Opalinus Clay. Boreholes BHE-23 to BHE-27, with depths between 5.5 m and 7.1 m, were used for the measurements. The borehole diameters were 131 mm, except for BHE-23 with 86 mm. The boreholes were radially distributed around the central borehole at distances between 0.36 m and 1.41 m (cf. Figure 6.32). Such a tight arrangement of boreholes is a very special case in terms of the stability of the boreholes. The heater element in borehole BHE-0 was situated between 4 m and 6 m depth. The measurements were performed from 26 - 30 September, 2003.

6.8.1 Methods

A BGR ultrasonic mini-borehole probe with one source and three receivers was used. The seismic velocities were measured along three small borehole intervals, typically between 10 cm and 30 cm long. For some special issues, seismic cross-hole measurements and rotation of the borehole probe was performed in and between selected boreholes. Additionally, a BGR borehole video recording tool was used. With the help of the borehole video analyses, the condition of the borehole wall could be rated and the best orientation of the seismic sensors was specified. Sensors were always oriented SSE (145°N), perpendicular to the strike of the bedding planes (dip approximately 45°). Therefore, the ray paths are oblique to the bedding planes with an angle of 45°. All borehole depths were measured from the top of the concrete floor.

6.8.2 Data

The data quality obtained from all measurements is very good. Common features in all data plots are the reduced velocities at low depths (EDZ and faults, cf. Figure 6.33), sine-wave like variations on a greater scale (most probably changes in lithology/facies), particularly around a depth of 2.5 m, and many small-scale variations, perhaps due to minor facies changes, cracks, fractures, etc. The following seismic parameters were derived from all data sets and were used to determine the extent and the state of the EDZ/EdZ:

- P- and S-wave velocities,
- absolute amplitudes,
- normalized amplitudes,
- apparent frequency of first arrival phases (P-waves) and S-wave onset phases,
- in-situ dynamic Poisson’s ratio,
- in-situ dynamic Young’s modulus, and
- in-situ dynamic modulus of rigidity.

6.8.3 Major results

The major results are discussed with emphasis on three points: characterization of the EDZ, detection of influences of the heater element on the Opalinus Clay and variation in derived characteristic seismic in-situ parameters.

6.8.3.1 Extent of the EDZ

The superposition of observed small- and large-scale variations in the derived parameters complicates the estimation of the extent of the EDZ. According to the individual parameter criteria, the video analyses and some site information, the extent of the EDZ, i.e. the damaged part of the rock, was estimated as follows: 1.9 m (BHE-23), 1.6 m (BHE-24) and 2.5 m (BHE-25) for the boreholes located approximately 35 cm from the central heater element. For these boreholes, the estimated extents have to be seen as minimum values, because positive evidence/estimate is made difficult by the facies or lithological change around 2.5 m depth with the resulting sine-wave like P-wave anomaly. For boreholes BHE-26 (51 cm from the heater borehole) the extent is 1.5 m and for BHE-27 (141 cm distance), 1.8 m was estimated. Figure 6.32 illustrates these findings. For comparison, results from former investigations in the Mont Terri Rock Laboratory from boreholes between 35 m and 75 m away from the HE niche are also included.

6.8.3.2 Influence of the heater element on the Opalinus Clay

The detection of possible changes in petrophysical properties of the Opalinus Clay due to the influence of the heater element was a crucial point in the experiment. Can such changes be detected with the help of seismic borehole measurements? In Figure 6.33, all channel 3 P-wave velocities are plotted onto one graph. Seismic waves which are recorded at receiver 3 (channel 3 data) generally have the greatest depth of penetration. The location of the heater element is also indicated. For a better comparison, and taking the anisotropy caused by the bedding of the Opalinus Clay into account (which has a considerable influence on the thermal conductivity), four individual graphs (BHE-23 to BHE-26) were shifted horizontally against the BHE-27 graph so that the sine-wave like P-wave velocity variations around 2.5 m depth correlate best. Results from an earlier investigation in a borehole (BED-C8, Gallery 98, measured in October 1999 in SW direction, approximately 30 m away from the HE niche) were added (black dots) without shift. Furthermore, a hypothetical P-wave velocity graph for an excavation damaged rock without further disturbances has been plotted (red dots). 2500 m/s can be regarded as a good average velocity for an undisturbed rock. This is supported by the velocity distribution of the BED-C8 data. To ensure this in the HE niche, the boreholes would have had to be deeper, so that the undisturbed rock could have been reached. Moreover, the sine-wave like variations make it impossible to detect characteristic velocities of an undisturbed rock in this range.

Except for the sine-wave like variations, the velocity of 2500 m/s is reached at 1.8 m depth for BHE-26 and BHE-27 (i.e. at greater distances to the central heater element), for BED-C8 data and at depths greater then 6.3 m for BHE-25, BHE-26, and BHE-27 data.

When it is considered that the velocity variations between 2.3 m and 3.5 m, as well as the variations between 5.0 m and 5.8 m, are caused only by changes in lithology or facies, then between 3.5 m and 6.3 m depth reduced velocities would be found when compared to the hypothetical (i.e. undisturbed rock) velocity of 2500 m/s. These reduced velocities, which are indicators of changes in rock properties, could be attributed to the influence of the heater element.

Between borehole depths of 0.7 m and 2.5 m, P-wave velocities from boreholes in close proximity to the heater element (approximately 0.37 m, i.e. BHE-23, BHE-24, and BHE-25) are lower than from boreholes at a greater distance (0.53 m for BHE-26 and 1.41 m for BHE-27). One reason could be the desaturation process which altered the rock. Furthermore, the occurrence of fault planes with indicators of shear sense, as mapped during the dismantling (cf. section 4.2, p. 27), have to be taken into account for detailed analyses.

A qualitative analysis of the cross-hole data derived from measurements between boreholes BHE-23 and BHE-24 and between BHE-26 and BHE-25 gave no clear evidence of a change in seismic parameters in the depth range of 4 m to 6 m.

The results from interval velocity measurements discussed above give reason to interpret the reduced interval velocities between 3.5 m and 6.3 m as being caused by the heater element. One possible explanation could be an increased desaturation in this depth range (although this is not supported by the geoelectric or geomechanical measurements, cf. sections 3.3.5, and 6.4.3, 6.5, and 6.7.4).

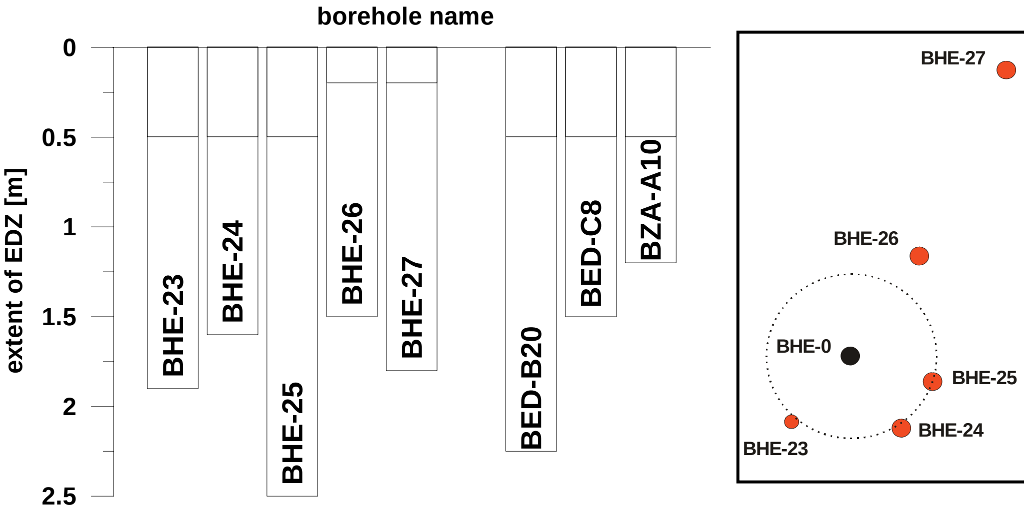

Figure 6.32: **Left: Derived extents of the EDZ (minimum values for BHE-23, BHE-24, and BHE-25). Grey parts indicate the approximate thickness of the concrete layer. Right: Borehole locations.**

6.8.3.3 Variation of derived seismic parameters

In the following, the variations in seismic parameters derived from borehole depth ranges greater than the extent of the EDZ and outside the sine-wave like anomalies at 2.5 m and 5 m are listed. These parameters can be seen as more representative values for the appropriate orientation of the sensors, here SSE. The ray paths are oblique to the bedding planes with an angle of 45° (comparable with the z-orientation). Small-scale variations within one data set can be observed in all boreholes, as well as clear trends along the borehole depths. In general, the dynamic in-situ Young's modulus and the seismic velocities increase with borehole depth. The variations are:

P-wave velocities:	2350 – 2550 m/s
S-wave velocities:	1200 – 1300 m/s
Dynamic in-situ Poisson's ratio:	0.34 – 0.37
Dynamic in-situ Young's modulus:	8 – 10 GPa
Dynamic in-situ modulus of rigidity:	1.5 – 4 GPa

For some of the boreholes, not all data, such as the S-wave onsets, were used. Therefore, the variation in values may be a bit wider than listed above.

The determination of in-situ dynamic elastic parameters can be seen as an approach to obtaining more information from the data. There are some uncertainties which are caused by the fact that the orientation between the seismic ray paths and the bedding is not as clear as in the laboratory tests, and the measurements are influenced by the small-scale EDZ/EdZ around the borehole wall. Comparisons between in-situ seismic parameters and parameters derived in the laboratories on selected and well orientated specimens (here z-orientation) still have to be made.

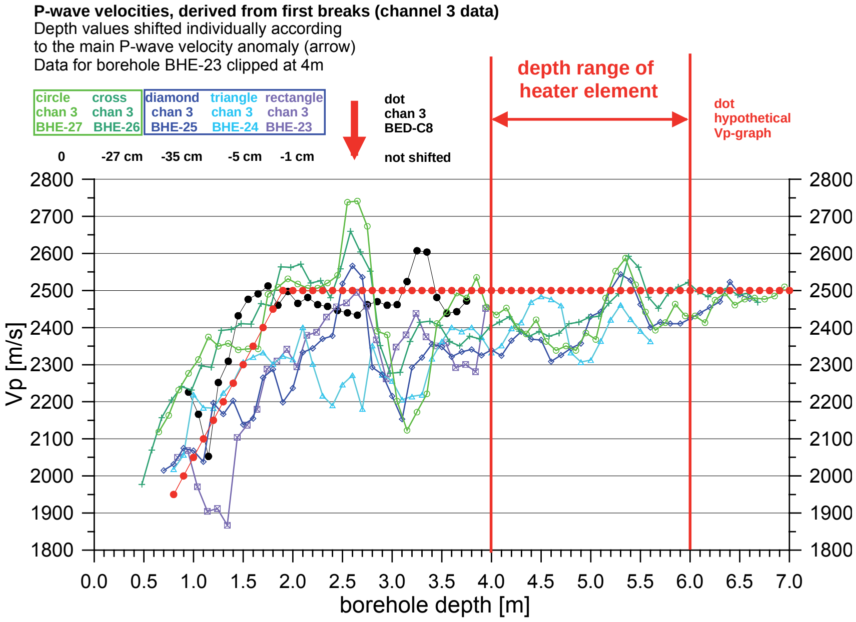

Figure 6.33: **Channel 3 P-wave velocities derived from boreholes BHE-23 to BHE-27. Graphs from BHE-26 to BHE-23 were shifted horizontally (see text). The shift values are given in the figure (top left). Superposition of sine-wave like P-wave velocity (v_p) variations, caused by changes in lithology, complicate the interpretation. A hypothetical v_p-curve (red dots) represents an excavation damaged rock without further disturbances. Reduced velocities between 3.5 m and 6.5 m could be a reaction to the heating (see text). Black dots: see text.**

6.9 Hydraulic conductivity - results of in situ measurements

Hydraulic conductivities were measured before and after the heating period in boreholes close to the heater borehole. Figure 6.34 shows the results for the conductivity of Opalinus Clay as a function of depth. Boreholes BHE-19 and BHE-20 were drilled on February 27-28, 2000. The first hydraulic tests were performed between November 2001 and February 2002, i.e. about one year later. It may be that some desaturation took place during the year around the boreholes. Borehole BHE-23 was drilled on September 23-24, 2003. Hydraulic tests took place in October 2003, i.e. shortly after the drilling. In this case, the Opalinus Clay will most likely have been fully saturated at depths of more than about 3 to 4 m (cf. Figure 6.17). Around BHE-19, the conductivity increases after heating by a factor of 2. The post-heating conductivity around BHE-19 is still about equal to the pre-heating conductivity around BHE-20. The conductivity around BHE-23 is almost an order of magnitude higher than the conductivities around boreholes BHE-19 and BHE-20. There is a cross-hole response between boreholes BHE-19 and BHE-23 at a depth of about 5 m. The constant head injection tests (HI in Figure 6.34) confirm the conductivity values determined by the pulse injection test (PI). The post-heating saturated hydraulic conductivity is assumed to be

$$K_s = 5 \cdot 10^{-11} \text{ m/s} = 4.32 \cdot 10^{-4} \text{ cm/d}.$$

If it is assumed that, deep in the borehole, the saturated state may have been preserved, it can be assumed that pre-heating hydraulic conductivity is

$$K_s = 1 \cdot 10^{-12} \text{ m/s} = 8.64 \cdot 10^{-6} \text{ cm/d},$$

although there is no strong indicator that the hydraulic conductivity really has changed due to the heating when there is no indication of a decrease in saturation (see section 3.3) and when the temperatures at a distance of 0.65 cm from the heater borehole did not exceed 50°C, see section 3.2.1. In comparison, GAUCHER et al. (2003) report conductivities in the Opalinus Clay of

Matrix rock:	$1 \cdot 10^{-13}$ to $5 \cdot 10^{-13}$ m/s
EDZ:	$4 \cdot 10^{-12}$ to $8 \cdot 10^{-8}$ m/s

This indicates that the conductivities measured in the boreholes are similar to values for the EDZ. There is a slight indication that the heating may have influenced the hydraulic conductivity.

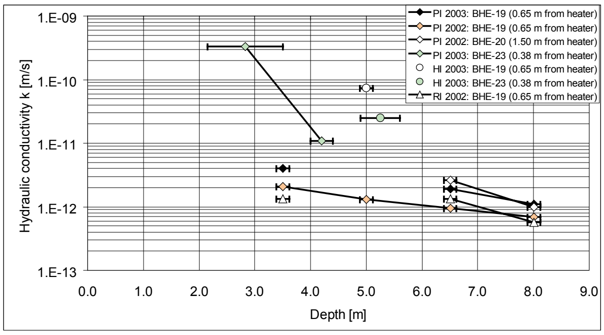

Figure 6.34: **Hydraulic conductivity close to the heater borehole. Results of in situ tests: PI: Pulse injection test, HI: Constant head injection test, RI: Constant rate injection test (injection period).**

6.10 Storage of specimens

For additional laboratory investigations of samples taken from the test field, it is essential to have specimens without significant alteration in terms of mechanical behaviour, mineralogical-chemical composition and fluid content in the pores. During sampling, storage and transport, the specimens should remain under conditions which are similar to the conditions in the original environment. In general, specimens are wrapped in plastic foils or bags and stored in open metal or wooden boxes. Very often, these methods have not been sufficient for clays, as the plastic foil or the specimens were damaged mechanically, the specimens dried, oxidised by contact with air and suffered from the loss of their external stress state. In the HE test, two methods for storage and transport of specimens have been developed.

6.10.1 GRS can: folded tin boxes

For the storage and transport of different types of rock specimens, cylindrical tin boxes with a diameter of 63 to 230 mm and a height of 62 to 260 mm are used. The size of the box can be adjusted to the diameter, length and number of specimens. The residual volume in the box is backfilled with drilling fines or special protective material. Drilling fines of the same material as the specimen ensure that, within a short time, equilibrium exists regarding the relative humidity and the gas composition. The specimen is protected against drying, external humidity and air. The specimens are put into the tin box and sealed gas-tight in situ and without time delay using the folding machine shown in Figure 6.35 (left). The tin box can be opened easily using a tin opener.

6.10.2 BGR liner

Extracting cores from the Opalinus Clay in the Mont Terri underground laboratory requires a means of protecting the sensitive clay from drying out and other external influences. The BGR liner, Figure 6.35 (right), has been designed for this purpose. It ensures proper storage, transport and protection of the cores until they are required for further analysis.

BGR drilling equipment is designed purely for exploration drilling and can currently be used to drill boreholes with diameters ranging from 46 to 146 mm. The associated core barrel (single or double core barrel type), the edge width and the type of coring bit produces cores with diameters of up to 101 mm. When cores are cut in solid rock, the process automatically leads to the release of stress in the core. The cores are also subject to external influences and climatic conditions to a varying degree depending on the location of the borehole and the local conditions. Undesirable effects include:

- atmospheric oxidation of the cores,
- absorption of water from the atmosphere,
- pressure release and potential fracturing of the cores in the absence of the original formation pressure.

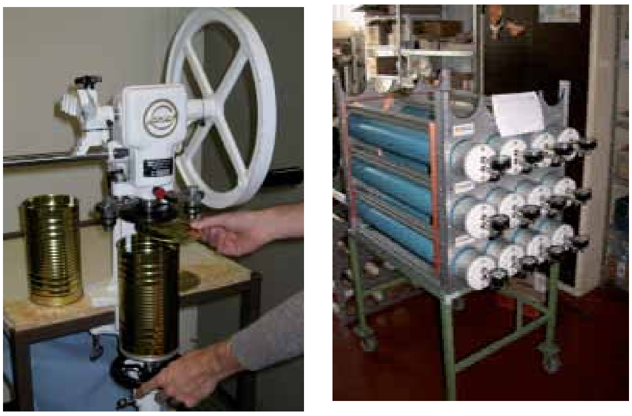

Figure 6.35 Folding machine for tin boxes with tin boxes of 113 mm diameter and 205 mm height (left). PVC liner with transport pallet of BGR liners (right).

Atmospheric oxidation and water absorption can be reduced to an acceptable level by sealing the cores in welded aluminium-coated plastic films. The transport container presented here has been developed to allow the cores to be stored under pressure to partially compensate for the absent formation pressure. The containers also protect the cores from mechanical damage. The PVC tubes are cut to a length of 166 cm for transport-related reasons. The internal diameter of the containers was chosen to provide sufficient room for cores with a diameter of 101 mm sealed in welded plastic film. The PVC tubes have screw lids with an O-ring seal and a ball valve. A maximum casing pressure of 3 bar can be exerted on the film-wrapped samples. Usually, nitrogen is used as the pressure medium. The maximum internal pressure strength of the tubes is 10 bar to ensure that a triple safety margin is present. The liners are put on special transport pallets to protect them from damage during transport. The advantages of the liner are as follows:

- standard liner materials (industrial tubing with a length of 5 m), simple operation, flexible liner lengths,
- the lids are solid, strong and can be easily produced in any diameter,
- pressure-proof to 10 bar (i.e. approximately triple safety margin against failure),
- rapid insertion and sealing of film-welded cores at the drill site,
- safe transport from drilling locations because of the specially shaped grooves in the transport pallets; simple transport further on in small vehicles,
- longer storage times possible before analysis (compared to core boxes),
- special valves for adjusting casing pressure,
- frequent reuse without major cleaning,
- low production costs when made in large numbers; no maintenance costs.

The BGR liners cost around € 300 each with the dimensions described here, including the ball valve. In the test version, a liner was filled with 5 samples of 101 mm diameter and 310 mm length. The core samples are protected by a welded aluminium-coated plastic film and the spaces between the cores are protected by foam disks.

7. Rock modelling in the near-field

7.1 Introduction

The coupled thermo-hydro-mechanical (THM) processes developed in the host rock (Opalinus Clay) and in the saturated bentonite buffer have been modeled with CODE_BRIGHT (OLIVELLA et al. 1996). Two simulations are discussed: an axisymmetric approximation and a 3D analysis, which introduces the rock anisotropy.

The axisymmetric numerical simulation of the HE experiment was divided into two parts. The first part covers the excavation of the HE niche and the drilling of borehole BHE-0. The second part of the numerical simulations covers the bentonite buffer emplacement and the hydration, heating and cooling phases. Special attention was given to the interaction between the bentonite buffer and the host rock in the near-field.

The HE experiment was instrumented with sensors for temperature, water pressure and inclinometers located in boreholes performed around the heating borehole BHE-0. The instrumentation provided data on the rock reaction to the bentonite swelling and thermal load. The numerical results were compared with experimental data in all phases of the experiment.

7.2 Features of the axisymmetric analysis

7.2.1 Geometry of the HE experiment

An axisymmetric numerical model with respect to the longitudinal axis of the borehole BHE-0 has been adopted. The geometry of the HE experiment, the niche and borehole dimensions and the different position of all components have been taken from FUENTES-CANTILLANA et al. (2001). A total of six different materials have been considered: 1- the host rock Opalinus Clay, 2- the bentonite buffer, 3- the heater tube, 4- the sintered filter, 5- the dry sand which fills the upper part of the borehole, 6- the resin used to seal the upper part of the borehole. Figure 7.1 shows the geometry of the HE niche and details of all the different materials placed in the borehole BHE-0. The heater tube is 75 mm in diameter and 7.00 m long. The heater element is placed between 6.00m and 4.00m depth. The sintered filters are 13 mm thick and extend from 7.00 m to 1.50 m depth. The gap between sintered filters and the host rock is filled with compacted bentonite blocks 100 mm thick. They are placed from 7.00 m to 2.00 m depth. The gap between the heater tube and rock, from 2.00 m to 0.40 m depth, is filled with sand. No account is taken of the possible gaps between buffer bentonite and rock and between buffer bentonite and heater. The upper part of borehole BHE-0, from 0.40 m to 0.00 m, is sealed with resin to avoid leakages of water and gas. It also supports the vertical thrust caused by the bentonite swelling.

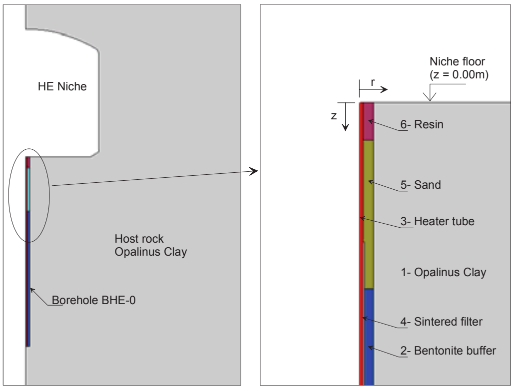

Figure 7.1 **Geometry of the HE niche and borehole BHE-0 (left). Different components emplaced into the borehole BHE-0 (right).**

The simulation of the excavation of the borehole BHE-0 was performed numerically. A period of 10 days was considered, when a new boundary condition of suction s = 6.80 MPa was applied on the wall of the borehole. The hydraulic boundary condition applied previously in the HE niche was maintained. Once the excavation phase was finished, a new numerical model was constructed with all the components of the HE experiment emplaced to borehole BHE-0. The initial degree of saturation at the bentonite buffer was 60 %, which corresponds to a suction s = 136 MPa.

Table 7.1: Equations defining the constitutive law of Opalinus Clay. For explanation of symbols see text.

Law	Equation	Parameters
Elastic	Linear elasticity	$E=(1+\chi)E_M(1+\chi)+\chi E_b\chi$ ν = Constant
Yield surface	Hoek-Brown criterion	$R_c=(1+\chi)\cdot R_{cM}$ $m=$ Constant
Flow rule	Associated	
Degradation law		$\chi=\chi_0 e^{-L/2}$

The hydration phase covers a period of 982 days, from 16/06/1999 (t = 0) until 22/02/2002 (t = 982 days). The hydraulic boundary condition applied to the HE niche was maintained. The boundary condition at the wall of the borehole BHE-0 was removed. A hydrostatic water pressure was applied to the sintered filter at four different depths, 6.90 m, 5.60 m, 4.40 m and 3.00 m. The water pressure at each injection point corresponds to a common piezometric head of 2.00 m over the niche floor.

The heating phase started after 982 days of hydration, with a temperature of 100 ºC being applied at the contact between heater and bentonite. A heating period of 554 days was considered, from 22/02/2002 (t = 982) until 31/08/2003 (t = 1536). The hydraulic boundary condition applied to the HE niche and the four injections points were maintained. A cooling phase of 365 days was considered in calculations, from 31/08/2003 (t = 1536) until 31/08/2004 (t = 1901). The boundary condition of temperature at the contact between bentonite and heater was removed, allowing the temperature to recover to initial conditions.

Table 7.2: Thermal parameters of the Opalinus Clay.

Properties	Value
Thermal conductivity	(2.10) [W/m/K]
Linear thermal expansion coefficient, $\mathbf{b_s}$	($1.00 \cdot 10^{-05}$) [ºC^{-1}]
Specific heat, **Cs**	(874.00) [J kg^{-1} K^{-1}]

Table 7.3: Mechanical parameters of the Opalinus Clay.

Properties	Value
E (Young's modulus)	6000.0 MPa
ν (Poisson's ratio)	0.27
UCS (unconfined compressive strength)	16.0 MPa
UTS (unconfined tensile strength)	2.0 MPa
m	8.0
χ	2.0

7.2.2 Host rock parameters

7.2.2.1 Mechanical constitutive law

The mechanical behaviour of the host rock has been modeled by means of the mechanical constitutive law proposed by VAUNAT & GENS (2003). Opalinus Clay is considered as a composite material made of a clay matrix interlocked by bonds. The bond response is modeled by a damage model proposed by CAROL et al. (2001), while the clay matrix can be represented by any model usually used to characterize a clay soil. In the case of Opalinus Clay, which has a low porosity (13.7 %), a Hoek-Brown criterion associated with a linear-elastic law was used. Applying the compatibility and equilibrium equations between bond, matrix and external strains and stresses, the material response was derived. It is governed by the equations and parameters shown in Table 7.1, where E, E_M, and E_b are Young's modulus of, respectively, the composite material, the clay matrix and the bonds, ν is Poisson's ratio, R_c and R_{cM} are uniaxial compression shear strengths of, respectively, the composite material and the clay matrix and m is a parameter determining the shape of the yield locus. The parameter χ is related to the amount of bonding. It takes the value χ_0 when bonds are intact (undamaged rock) and progressively degrades as damage proceeds (measured by the damage variable L). L appears to be related to the degradation of the Young's modulus of the bond only, following the expression $L = \ln(E_0/E)$, where E_0 and E are the undamaged and damaged Young's modulus of the bond, respectively.

Parameters were determined on the basis of laboratory data and are summarized in Table 7.3. E and ν are assessed on intact rock samples. Values of R_c and R_{cM} give the upper and lower envelopes for all measured shear strengths. m is the ratio of uniaxial compressive strength and tensile strength. Parameter χ_0 is then computed as: $(R_c - R_{cM})/R_{cM}$. E_m and E_b are derived from values of E and χ_0, assuming that $E_b = E$ in the undamaged state ($\chi = \chi_0$). Damage evolution is finally defined on the basis of measurements of Young's modulus reduction during cyclic triaxial tests.

Table 7.4: Hydraulic parameters of the Opalinus Clay.

Properties	Value
Intrinsic permeability, **k** (Kozeny model)	$k = k_0 \frac{\phi^3}{(1-\phi)^2} \frac{(1-\phi_0)^2}{\phi_0^3}$ ϕ_0: reference porosity (0.137) k_0: intrinsic permeability for matrix ($3.50 \cdot 10^{-19}$) [m^2]
Water retention curve (modified Van Genuchten model)	$S_e = \frac{S_l - S_{rl}}{S_{ls} - S_{rl}} = \left(1 + \left(\frac{P_g - P_l}{P}\right)^{\frac{1}{1-\lambda}}\right)^{-\lambda} \left(1 - \frac{P_g - P_l}{P_s}\right)^{\lambda_s}$ S_e: Effective saturation ($0 \le S_e \le 1$) P : Material parameter (3.90) [MPa] P_s : Material parameter (700.00) [MPa] λ : Shape function for retention curve (0.128) λ_s : Material parameter (2.73) S_{rl}: Residual saturation (0.00) S_{ls}: Maximum saturation (1.00)
Relative permeability, $\mathbf{k_{rl}}$ (Van Genuchten model)	$k_{rl} = \sqrt{S_e}\left(1 - \left(1 - S_e^{1/\lambda}\right)^{\lambda}\right)^2$ S_e: Effective saturation ($0 \le S_e \le 1$) λ : Power (0.29) S_{rl}: Residual saturation (0.00) S_{ls}: Maximum saturation (1.00)
Porosity, **n**	(0.137)

7.2.2.2 *Opalinus Clay parameters*

The mechanical, hydraulic and thermal parameters used in the model have been taken from available information on Opalinus Clay rock (HOHNER & BOSSART 1998, BOCK 2001, section 6.5). They are summarized in Table 7.2 to Table 7.4.

Table 7.5: Mechanical parameters of the FEBEX bentonite.

Elastic Parameters		***Plastic Parameters***	
Properties	**Value**	**Properties**	***Value***
γ_d=(1.80) [g/cm^3]		λ **(0)**	(0.158)
		r	(0.75)
k_{io}	**(0.02)**	β	(0.05)
k_{so}	**(0.3)**	ρ	(0.2)
ν	**(0.3)**	**k**	(0.1)
α_{ss}	**(-0.03)**	$\mathbf{p^c}$	(0.1)
α_{is}	**(-0.003)**	**M**	(1)
α_{sp}	**(-0.135)**	α	(0.395)
$\mathbf{P_r}$	(0.01)	P_0*	(22.0)

7.2.2.3 Bentonite parameters

The bentonite barrier has been modeled using a thermo-elasto-plastic model for unsaturated soils. The bentonite parameters are derived from the information on the FEBEX project (LLORET et al. 2002). They are summarized in Table 7.5 to Table 7.7. A full description of the bentonite model can be found in DIT-UPC (2002).

Table 7.6: Thermal parameters of FEBEX bentonite.

Properties	Value
Thermal conductivity	$\lambda = \lambda_w^{S_l} \cdot \lambda_d^{(1-S_l)}$ λ_w: (1.28) [W/m/K] λ_d: (0.50) [W/m/K]
Linear thermal expansion coefficients, $\mathbf{b}_s$	(0.35·10^{-05}) [ºC^{-1}]
Specific heat, **Cs**	(732.00) [J kg^{-1} K^{-1}]

Table 7.7: Hydraulic parameters of FEBEX bentonite.

Properties	Value
Intrinsic permeability, **k** (Kozeny model)	$k = k_0 \frac{\phi^3}{(1-\phi)^2} \frac{(1-\phi_0)^2}{\phi_0^3}$ ϕ_0: Reference porosity (0.40) k_0: Intrinsic permeability for matrix (1.1·10^{-21}) [m^2]
Water retention curve (Van Genuchten model)	$S_e = \frac{S_l - S_{rl}}{S_{ls} - S_{rl}} = \left(1 + \left(\frac{P_g - P_l}{P}\right)^{\frac{1}{1-\lambda}}\right)^{-\lambda}$ S_e: Effective saturation ($0 \leq S_e \leq 1$) P : Material parameter (90.00) [MPa] λ : Shape function for retention curve (0.45) S_{rl}: Residual saturation (0.00) S_{ls}: Maximum saturation (1.00)
Relative permeability, $\mathbf{k}_{rl}$ (generalized power)	$k_{rl} = Se^{\lambda}$ S_e: Effective saturation ($0 \leq S_e \leq 1$) λ : Power coefficient (3.5)
Porosity, ***n***	(0.40)

7.3 Results of axisymmetric analysis

The results of the numerical model are presented and compared with in situ data, following the main phases of the experiment. In all phases, the displacement field, stress state, porewater pressure distribution and temperature field around borehole BHE-0 were analyzed.

7.3.1 HE niche excavation phase

At the end of the niche excavation phase, the maximum downward vertical displacements calculated occur at the crown of the niche and reach a value of 6.7 mm. The upward vertical displacement on the niche floor, at the symmetry axis, reaches a value of 1.6 mm. A maximum horizontal displacement of 2.2 mm is calculated at the half-height of the niche wall (Figure 7.2).

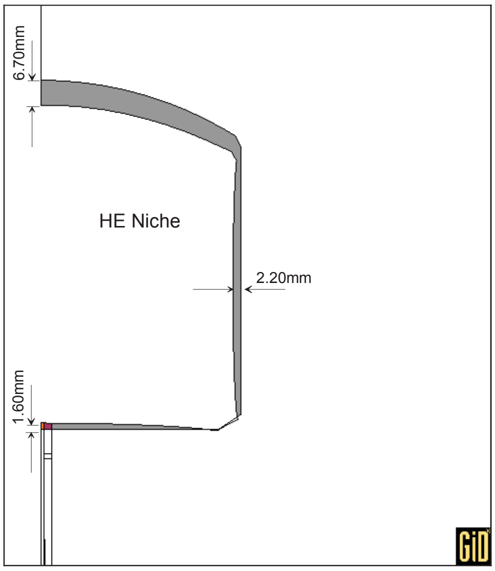

Figure 7.2 The shaded zone shows the HE niche deformation calculated 420 days after excavation of the niche.

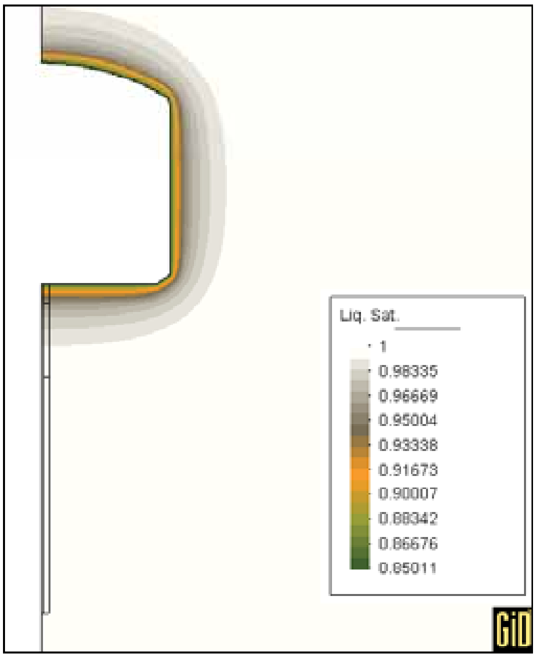

Figure 7.3: Degree of saturation (Sr) around the HE niche after 420 days.

The distribution of the degree of saturation (S_r) around the niche can be seen in Figure 7.3. An unsaturated zone around the HE niche, which reaches a thickness of 1.5 m around the wall, developed. The calculated degree of saturation in the niche perimeter is close to $S_r = 85.0$ %.

7.3.2 Hydration phase, heating phase, and cooling phase.

Figure 7.4 shows the temporal evolution of the calculated and measured temperature during the operational phase of the HE experiment. Figure 7.5 shows the temporal evolution of the calculated and measured pore pressure. For hydration, the water was injected into the sintered filter at four different depths: 6.9 m, 5.6 m, 4.3 m and 3.0 m. The water pressure at each injection point corresponds to a common piezometric head of 2.00 m over the niche floor.

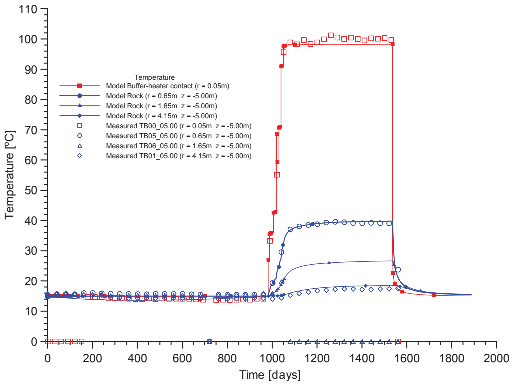

Figure 7.4: **Time evolution of temperatures calculated and measured during the hydration, heating and cooling phases, in points located in bentonite and rock.**

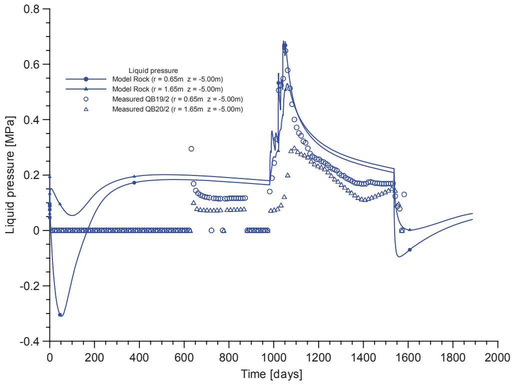

Figure 7.5: **Time evolution of liquid pressure in points located in rock during hydration, heating and cooling phase.**

During the first phase of the hydration the water entered into the sintered filter and rose towards the upper part of the borehole, where the sand was quickly saturated. After this, the water slowly began to saturate the bentonite buffer. The high initial suction of bentonite (136 MPa) produces a desaturation in the surrounding rock up to a radial distance of 0.70 m. Figure 7.6 shows the pore pressure and degree of saturation in the bentonite blocks and in the rock, calculated after 45 days of hydration. The time required to saturate the bentonite is approximately 200 days. Figure 7.7 shows the transitory process of the desaturation and resaturation produced in the surrounding rock at 5.0 m depth. The rock reaches full saturation after 250 days of hydration.

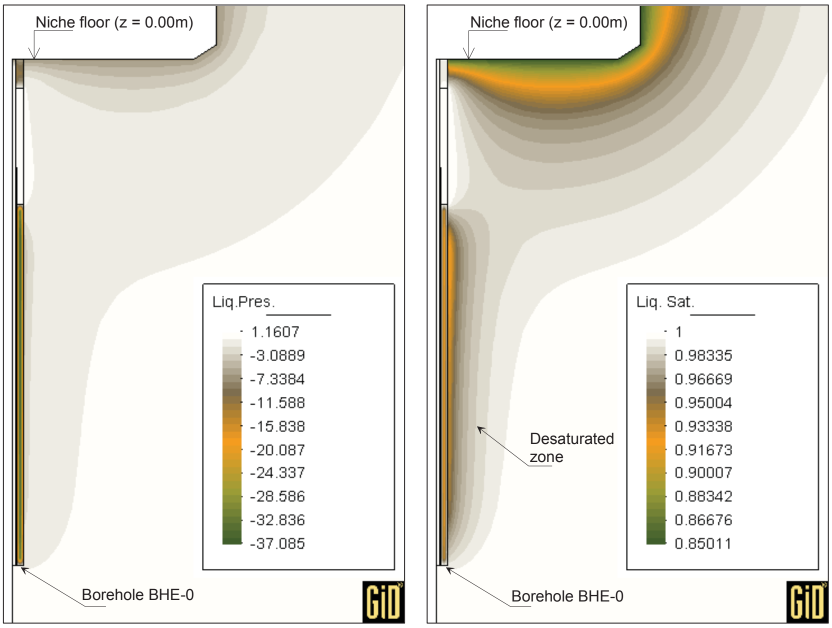

Figure 7.6: **Liquid pressure distribution after 45 days of hydration (left). Degree of saturation of the surrounding rock after 45 days of hydration (right).**

The measured and calculated water inflow during the hydration phase is shown in Figure 7.8. The theoretical quantity of water required to reach full saturation of bentonite and sand is 116.45 l. An amount of 105.5 l of injected water was calculated with CODE_BRIGHT, while a total amount of 150.16 l of injected water was measured. The discrepancy between the calculated and measured quantity of injected water may be due to the leaks in the heater tube at the beginning of the hydration phase, cf. section 2.3 (p. 11).

As a consequence of the high swelling pressure of bentonite, plastic strains are produced in some points of the rock. The calculated plastic zone was located in a narrow annulus of rock adjacent to the bentonite buffer. It reaches a maximum thickness of 0.05 m.

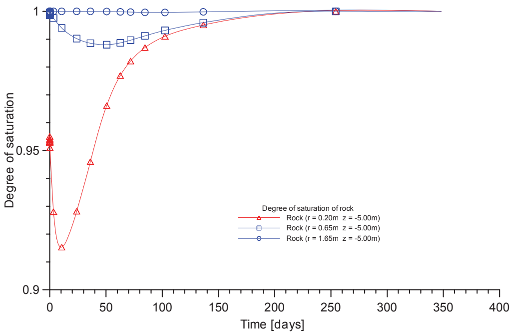

Figure 7.7 **Time evolution of the degree of saturation in the surrounding rock during the hydration phase.**

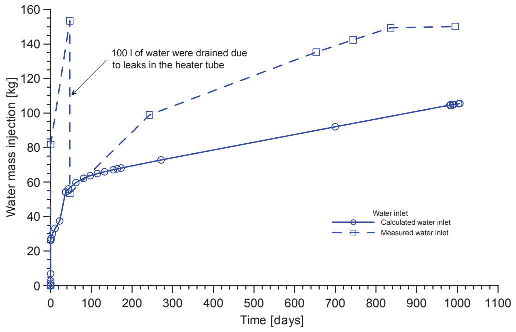

Figure 7.8 Calculated and measured water inflow during the hydration phase.

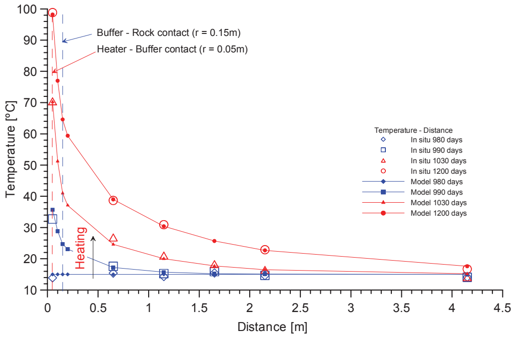

Figure 7.9 Calculated and measured distribution of temperature as a function of distance for different times during the heating phase.

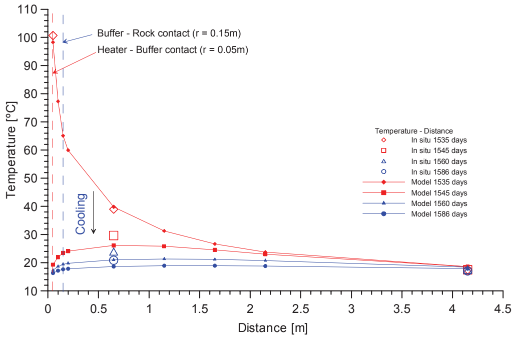

Figure 7.10 Calculated and measured distribution of temperature as a function of distance for different times during the cooling phase.

For the heating, power is initially applied in steps of 140W, 150W, 285W and 580W to the axis of the heater, until the heater-buffer contact (r = 0.05 m) reaches a temperature of 100 ºC (Figure 7.4). The calculated and measured distribution of temperature as a function of distance for different times during the heating phase is shown in Figure 7.9. Temperature increments generate positive water pressures (Figure 7.5). Water pressure increments from 0.12 MPa to 0.73 MPa were measured by sensor QB19/2 at time t = 1050 days, while the water pressure increments of 0.07 MPa to 0.30 MPa at time t = 1080 days were measured by sensor QB20/2. Note that 30 days elapsed between the maximum water pressure measured by sensors QB19/2 and QB20/2. At constant temperature, dissipation of water pressure tending towards the initial condition occurs. A fast temperature increase generates a pulse of water pressure which is then dissipated with time.

The pore pressure increments are well reproduced by the model. Pore pressure increments are induced by the thermal expansion of the water. In fact, the coefficient of thermal expansion of water is higher than the thermal expansion coefficient of the solid skeleton. The magnitude of the increments of liquid pressures is controlled by several factors, such as the rate of temperature increase, the rock permeability, the rock porosity, the rock stiffness and geometry and the boundary conditions of the experiment.

For the cooling phase, calculations indicate that the temperature decreases quickly after the power supply is stopped (Figure 7.4). The profile of temperature versus radial distance is shown in Figure 7.12. After 25 days of cooling, the temperature drops to less than 25º C in the whole area of influence of the test. The cooling may induce negative pore pressure and its magnitude depends on the rate of temperature decrease (Figure 7.5).

The rock stresses in the near-field of borehole BHE-0 are a consequence of the complete history of the HE experiment, such as the HE niche excavation, borehole BHE-0 drilling, the development of swelling pressures and the thermal dilation of materials. The effective stress path followed by a point in the rock close to the interface with the bentonite (r = 0.18 m) has been plotted in Figure 7.10. The plot shows that this point reaches limiting conditions at some time during hydration. Once the initial strength envelope is hit, limited rock degradation occurs. The stress path shows how the stresses are maintained at the current limiting strength surface. Some additional yielding is calculated during the heating phase. During the cooling phase, an unloading of the represented point of the rock was produced.

7.4 Anisotropic viscoplastic constitutive model

7.4.1 Introduction

A constitutive mechanical model for representing the shaly nature of the Opalinus Clay has been developed. The model has been formulated within an elasto-viscoplastic framework following the Perzyna theory (PERZYNA 1966; SANCHEZ 1997). It takes into account the anisotropic strength and deformability due to matrix and discontinuities (WITTKE 1990). The constitutive model has been implemented in the finite element code CODE_BRIGHT (OLIVELLA et al. 1996).

The model was used in a 3D calculation of the experiment. The analysis covers the different phases of the HE experiment, such as borehole BHE-0 excavation, hydration of bentonite, heating and cooling phases. The geometry of the HE experiment has been simplified. The HE niche has not been considered in the geometry of the experiment. The detailed geometry of the materials filling the borehole has not been included in the simulation. Only the Opalinus Clay host rock has been considered. Special attention was given to analysing the displacements in the near-field. The isotropic and anisotropic hypotheses for the mechanical behaviour of the host rock have been compared.

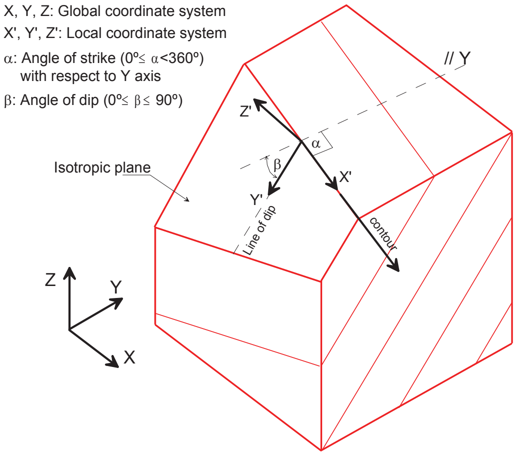

Figure 7.11 **Relationship between the global coordinate system and the orientation of the isotropic plane.**

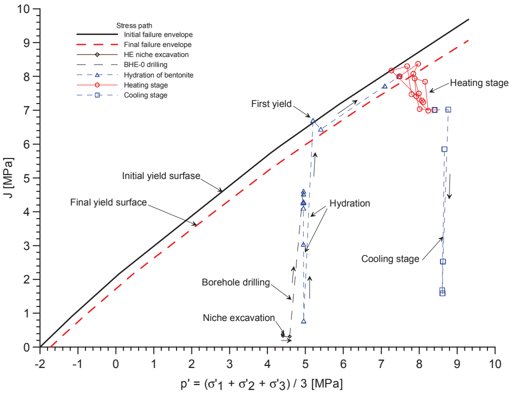

Figure 7.12 **Effective stress path followed by a point in the rock close to the bentonite-rock interface (r = 0.18 m).**

In the constitutive model formulation, the elastic behaviour is characterized by a cross-anisotropic material, where five independent elastic constants are required. The plastic character of the rock is attributed to two components: the matrix and a family of discontinuities. The discontinuities define the anisotropic plastic behaviour. The failure criterion of the matrix is defined by means of the hyperbolic yield surface in the p – J space. Matrix degradation is induced by means of an isotropic and kinematic softening controlled by the plastic work. The failure criterion of the family of discontinuities is defined by means of a hyperbolic yield surface in terms of shear and effective normal stresses acting on the isotropic planes. In a similar way to the matrix formulation, the degradation in the discontinuities is induced by means of an isotropic and kinematic softening controlled by the plastic work. Figure 7.11 is a representation of the model. The global coordinate system X, Y, Z, related in general to the engineering structure, does not coincide with the local coordinate system X', Y', Z' of the anisotropy direction. The link between the global and the local coordinate systems is established by two angles that describe the direction of a plane, strike (α), and the slope of the line of dip, dip (β), of the isotropic plane in relation to the global coordinate system. The photo from the dismantling of the HE experiment, Figure 3.9 (p. 18), shows the cross-anisotropic Opalinus Clay rock in the wall of the excavation. Both rock matrix and joints are characterized by plastic models which show degradation, as represented in Figure 7.13 for the rock joints.

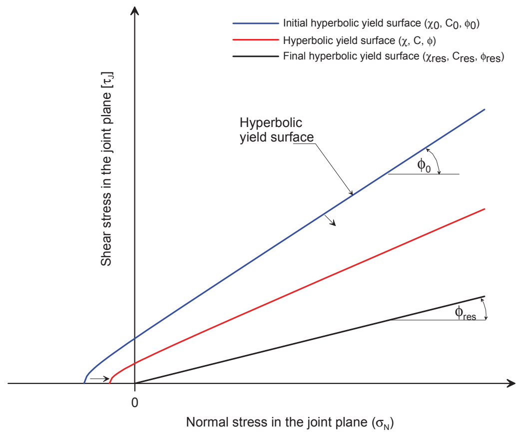

Figure 7.13: Evolution of the hyperbolic yield surface adopted for the rock joints.

7.4.2 Calibration of the constitutive model

Laboratory triaxial tests (cf. section 6.6, p. 65) have been reproduced in order to calibrate the mechanical constitutive model. A 3D numerical model of the samples has been developed. The samples were 100 mm in diameter and 250 mm in length and were discretized in a 3D finite element mesh of 2541 nodes and 2160 linear quadrilateral prism elements, having 8 integration points. Numerical simulations of samples with dip angles of schistosity of 0º, 15º, 30º, 45º, 60º, 75º and 90º have been performed. The boundary conditions applied in the numerical model are as follows:

a- Confining pressure of $\sigma_3 = 1$ MPa was applied to the sample.

b- The vertical displacements of the nodes located on the upper side of the sample were fixed.

c- Vertical displacements were imposed in the nodes located on the lower side of the sample. A vertical strain rate of $\dot{\varepsilon} = 0.00001/s$ was imposed.

Figure 7.14 shows one example of the stress-strain behaviour and the stress path for the numerical simulations of a sample with a dip angle of 45º.

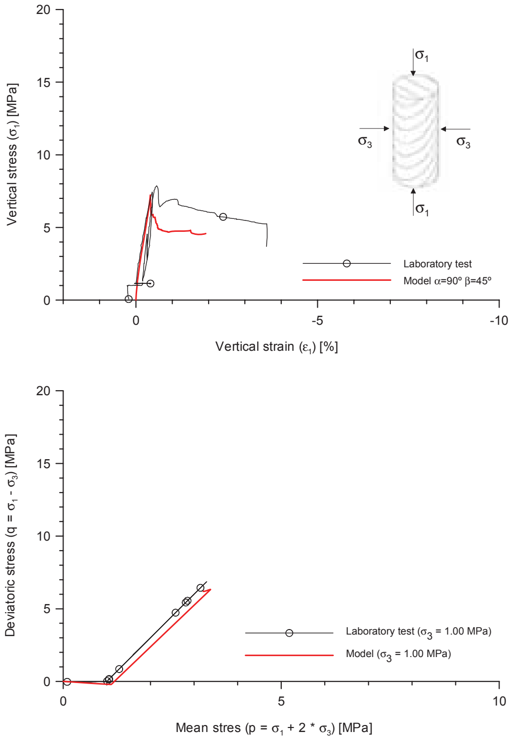

Figure 7.14: **Comparison between numerical simulations and triaxial laboratory test for a sample with angle of dip of 45º. Stress-strain behaviour (top). Stress path (bottom).**

7.5 3D model of the HE experiment

7.5.1 Geometry of the HE experiment

The HE experiment was discretized by means of a 3D finite element mesh of 12491 nodes and 11088 linear quadrilateral prism elements, having 8 integration points. Each node has five degrees of freedom, namely three displacements (X, Y, and Z directions), the pore pressure and the temperature. The domain is 20.30 m in length in both horizontal directions (X and Y) and 20.00 m in height in the vertical direction (Z). The borehole BHE-0 is 300 mm in diameter and 7.00 m deep. The coordinate system has its origin at the intersection between the floor of the HE niche and the longitudinal axis of borehole BHE-0. Figure 7.15 shows an isometric view of the finite element mesh.

7.5.2 Initial and boundary conditions

The initial vertical stress in the host rock was $\sigma_z = -6.00$ MPa and both horizontal stresses were $\sigma_x = \sigma_y = -4.00$ MPa. A hydrostatic porewater pressure distribution was applied, where $P_w = 0.10$ MPa corresponds to the HE niche floor (depth = 0.00 m). The initial temperature at the host rock was 15 ºC. Before the simulation of the different phases of the experiment, a stage of equilibrium of stress and porewater pressure was performed. In this phase, the radial displacements of the nodes located on the borehole wall were impeded. The 3D numerical model of the HE experiment covers the following steps:

Table 7.8: Mechanical parameters of the Opalinus Clay in the 3D model.

Deformation parameters of transverse rock model	
Tangent modulus $E_{X'-X'} = E_{Y'-Y'}$ (// bedding planes) [MPa]	3000
Tangent modulus $E_{Z'-Z'}$ ($\perp$ bedding planes) [MPa]	1500
Poisson's ratio. ν_{XY} -	0.33
Poisson's ratio. $\nu_{ZX} = \nu_{ZY}$ -	0.24
Shear modulus $G_{ZX} = G_{ZY}$ [MPa]	650
α = angle of strike ($0° < \alpha < 180°$), with respect to Y axis [°]	60.0
Dip angle ($0° < \beta < 90°$) [°]	35.0
Viscous parameters	
$\Gamma_M = \Gamma_J$ [1/s]	1.00E-05
$N_M = N_J$ -	3
F_{0M} [MPa]	12.0
F_{0J} [MPa]	1.0
Strength parameters of matrix	
Uniaxial compressive strength $UCS_{\perp} - UCS_{//}$ [MPa]	12.0
Uniaxial tensile strength $UTS_{\perp} - UTS_{//}$ (χ) [MPa]	5.0
Cohesion (c) [MPa]	6.0
Friction angle (ϕ) [°]	30.0
Residual friction angle (ϕ_R) [°]	15.0
Dilatancy angle (ψ) [°]	25.0
Strength parameters of the joint	
Tensile strength (χ_{joint}) [MPa]	2.0
Cohesion (c_{joint}) [MPa]	2.0
Friction angle (ϕ_{joint}) [°]	23.0
Residual friction angle (ϕ_R) [°]	15.0
Dilatancy angle (ψ) [°]	20.0

Step 1: Excavation of borehole BHE-0. The borehole excavation was simulated allowing free displacement of the nodes located on the borehole wall. A suction s = 6.80 MPa was applied on the borehole wall. During the borehole excavation, suction was increased from s = 6.80 MPa to s = 11.5 MPa. The excavation phase was performed under isothermal conditions at a temperature of 15° C. The excavation phase lasted 10 days.

Step 2: Hydration of the bentonite. The bentonite swelling pressure was simulated by means of radial pressure of 15 MPa applied on the borehole wall, from 2.00 m to 7.00 m depth. The radial stresses were increased from 0 MPa to 15 MPa during the first 200 days of hydration. The radial stresses then remained constant until the end of the hydration phase. The hydration was performed under isothermal conditions at a temperature of 15° C and lasted 33 months.

Step 3: Heating phase. A temperature boundary condition of 65 °C was applied on the borehole wall, from 4.00 m to -6.00 m depth. The temperature applied corresponds to the maximum temperature reached by the rock at the bentonite-rock contact (r = 0.15 m), as was shown in the 2D model. Radial stresses of 15.00 MPa were applied on the borehole wall and kept constant during the heating phase. The heating phase lasted 18 months.

Step 4: Cooling phase. The boundary condition of temperature on the borehole wall was removed, allowing the temperature to recover to the initial condition. The cooling phase lasted 9 months.

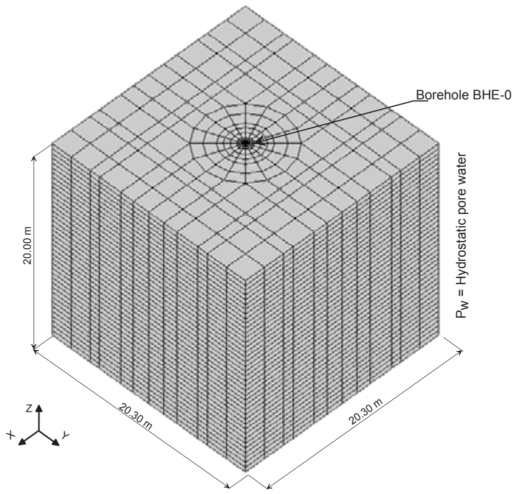

Figure 7.15 3D finite element mesh used in the model of HE experiment.

7.5.3 Opalinus Clay parameters

The mechanical, hydraulic and thermal parameters of the Opalinus Clay rock used in the 3D model have been taken from Hohner & Bossart (1998), Bock (2001) and from sections 6.5 and 4.2.2 above. They are summarized in Table 7.8, Table 7.4 and Table 7.2.

7.6 Analysis of 3D modelling results

The following data have been analyzed: temperature field, porewater pressure distribution, stress state and displacement around borehole BHE-0. Figure 7.16 shows the plan view of the HE experiment and the points where the different variables are calculated and compared. Points (1), (2), (3) are located in the X direction at 5.00 m depth and at radial distances of 0.65m, 1.65 m and 4.15 m, respectively. Points (4), (5), (6) are located in the Y direction at 5.00 m depth and at radial distances of 0.65 m, 1.65 m and 4.15 m, respectively. Points (7) and (8) are located at radial distances of 1.65 m in the direction of the bedding plane.

The distribution of the temperatures was well captured by the 3D model. The pore pressure sensors QB 19/2 and QB 20/2 are located at points (1) and (2) in Figure 7.16. Figure 7.17 shows the measured and calculated liquid pressure evolution. The suction applied during the excavation phase produces a transitory state of the liquid pressure in the rock surrounding the borehole. At the beginning of the heating phase, the calculated liquid pressure increases suddenly from 0.15 MPa to 0.90 MPa at point (1). The maximum calculated liquid pressure at point (2) is 0.79 MPa. The magnitude of the liquid pressure increment depends on the factors mentioned above (section 7.3.2).

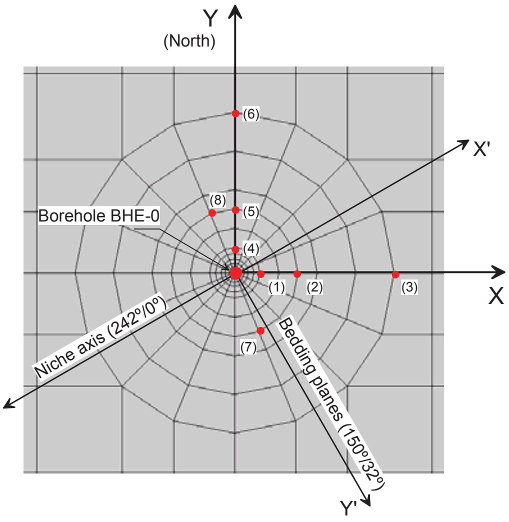

Figure 7.16: **Plan view of the finite element mesh of the HE experiment.**

During the excavation phase, radial displacements are directed towards the borehole axis. The radial displacement for points (1) and (4) is shown in Figure 7.18 for the isotropic and anisotropic model. The profile of radial displacements versus depth at time = 1070 days (heating phase) was calculated on the bedding plane direction, points (7) and (8), as shown in Figure 7.19, where the profile for an isotropic and anisotropic model are compared. Figure 7.20 shows the radial displacement (Y direction) for the isotropic and anisotropic model.

7.7 Conclusions

The coupled THM process and the interaction between the engineered and geological barriers developed in the HE experiment have been analyzed. All the construction and testing phases of the HE experiment were modeled. The evolution of stress state and liquid pressure during niche excavation and borehole drilling has been reproduced. The phases of niche excavation and borehole drilling are of vital importance in the model, since they control the initial stress state and pore pressure for the subsequent phases.

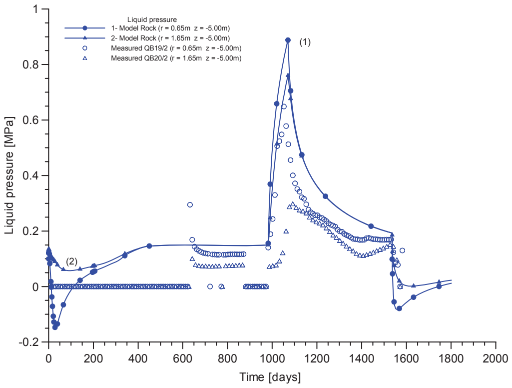

Figure 7.17: **Evolution of liquid pressure with time at points located in rock during the excavation, hydration, heating and cooling phases.**

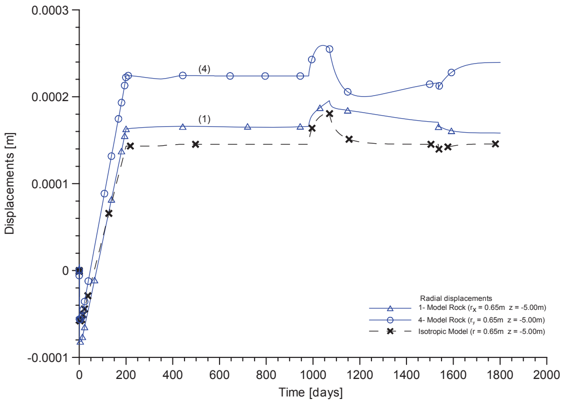

Figure 7.18: **Evolution of the calculated radial displacement at points (1) and (4) during the excavation, hydration, heating and cooling phases.**

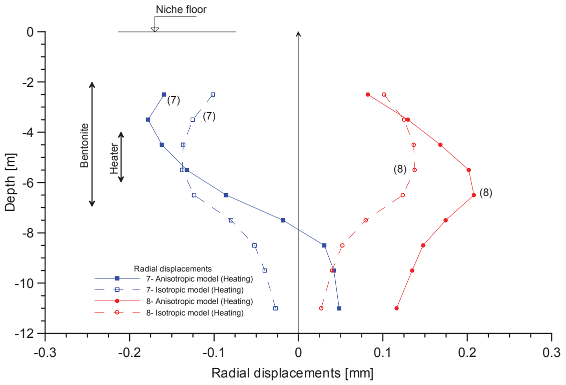

Figure 7.19: **Profile of calculated radial displacements versus depth at the end of the heating phase (1535 days) in points (7) and (8) of Figure 7.16.**

During the hydration phase, the high initial suction of bentonite induces an unsaturated state in the surrounding rock, which reaches a maximum at a radial distance of 0.70 m. The desaturation and subsequent resaturation process took place in approximately 200 days. The hydration of the bentonite generates high swelling pressures which reach maximum values of 14.0 MPa in the rock close to the interface. The bentonite swelling pressures produce significant changes in the stress state in the surrounding rock, which affect a zone with a thickness of 1.0 m. Plastic strains are produced in a narrow zone of the rock (thickness of 0.05 m) adjacent to the bentonite-rock interface.

Computed temperatures during the heating phase are close to the measured values. The temperature field extends to a maximum radial distance of 5.0 m. The increments of liquid pressure and subsequent dissipation measured during heating are well captured by the model. The positive pore pressure generated by temperature increments causes a drop in the effective stresses, which implies a certain loss of rock strength. The magnitude of liquid pressure increments is controlled by the rate of temperature increments, the rock permeability, the rock porosity, the rock stiffness and the geometry of the experiment. The heating phase generates a transitory change in the total and effective stresses. Successive heating extends the annular zone of plastic strain to a maximum thickness of 0.08 m.

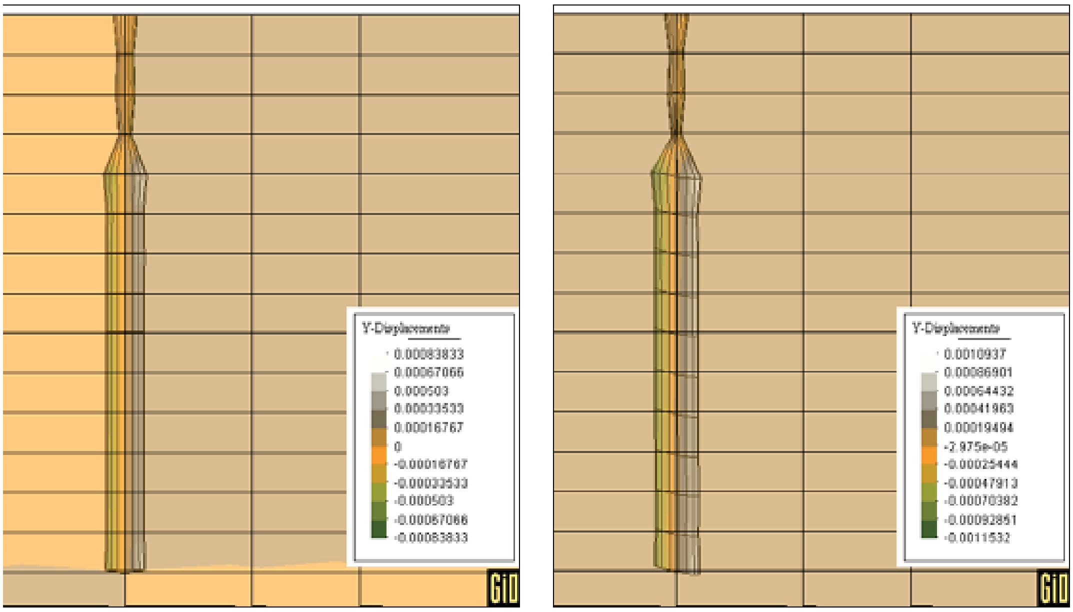

Figure 7.20 **Displacement in Y direction. Isotropic model (left) and anisotropic model (right) during heating phase, t = 1070 days**

The cooling phase induces a negative pore pressure, the magnitude of which depends on the rate of the temperature decrease. The pore pressure reaches a stable state after approximately 250 days of cooling. Cooling implies a transient change in total and effective stresses. On the long term, steady state stresses do not seem to be affected by the heating and cooling phases.

An anisotropic elasto-viscoplastic model has also been developed to represent the mechanical behaviour of the Opalinus Clay. The constitutive model has been calibrated by triaxial laboratory tests. The variation in rock strength with the angle of dip has been determined and compared satisfactorily with laboratory test results. A significant proportion of material parameters have been taken from experimental tests performed on the Opalinus Clay.

A 3D finite element model has been developed to reproduce the HE experiment. The bentonite swelling has been represented by a fully developed swelling pressure. Significant differences between the isotropic and anisotropic models have been found in the direction and intensity of displacements, in the stress distribution and in the plastic zone developed. Points located at the same radial distance to the borehole axis but at different positions in the circumferential direction exhibit significantly different responses. Particularly sensitive are the calculated radial displacements caused by borehole heating. The radial pressure develops a plastic zone with a thickness of 0.05 m, similar to the value found in the isotropic analysis.

8. Rock modelling in the far-field

Modelling the effects due to heating in the far-field (i.e. the host rock) focused on

- the development and implementation of a suitable THM coupled model (based on the existing HM coupled MEHRLIN code) and
- the assessment of thermally induced hydraulic and mechanical phenomena in the rock mass, such as the evolution of pore pressure, compressive stress and shear stress.

8.1 Model overview: THM coupled model

8.1.1 Model features

The fully coupled three-phase formulation employed is based on the continuum theory of mixtures and treats the unsaturated soil as a superposed continuum of solid, liquid and gas. The medium is assumed to be subject to non-isothermal conditions. In what follows, the constituents are assumed to be non-miscible and chemically non-reactive. Because of the local thermodynamic equilibrium hypothesis which is assumed to hold, the temperatures of all the constituents at a point in the multiphase medium are equal.

The main variables are the solid deformation, the water and the gas pressure and the temperature. The motion of the two fluid phases is governed by viscous and capillary flow. The resulting system of equations is discretised in space using the finite element technique and in time by an implicit/explicit method (Θ - method).

The heat-balance equation in the MEHRLIN code considers thermal coupling between the solid and fluid phases under certain simplifying assumptions. For the description of the non-isothermal unsaturated porous medium, not only heat conduction and vapour diffusion, but also heat convection and liquid water flow due to pressure gradients or capillary effects are considered. It is assumed that latent heat transfer due to water phase change (evaporation and condensation) inside the pores is negligible.

8.1.2 Summary of governing equations

The coupled system of equations reads:

Momentum balance:

$$\nabla \bullet \left(\sigma^e - \frac{\beta_s T}{3} - S^w p^w I - (1 - S^w) p^a I \right) + \rho g = 0 \qquad (11)$$

Water - solid mass balance:

$$\left(n \frac{\partial S^w}{\partial p^c} + \frac{n S^w}{K_w} \right) \frac{\partial p^w}{\partial t} - n \frac{\partial S^w}{\partial p^c} \frac{\partial p^a}{\partial t} - \beta_{sw} \frac{\partial T}{\partial t} + S^w \nabla \bullet v^s - \frac{k_r^w K}{\mu^w(T)} \nabla \bullet \nabla p^w = - \frac{k_r^w K}{\mu^w(T)} \nabla \bullet [\rho g] \qquad (12)$$

Air - solid mass balance:

$$-\left(n\frac{\partial S^w}{\partial p^c}\right)\frac{\partial p^w}{\partial t}+(n\frac{\partial S^w}{\partial p^c}+\frac{S^a M_a n}{\rho^a \theta R})\frac{\partial p^a}{\partial t}-S^a\beta_s(1-n)\frac{\partial T}{\partial t} \quad +S^a\nabla\bullet v^s-\frac{k_r^a K}{\mu^a(T)}\nabla\bullet\nabla p^a=-\frac{k_r^a K}{\mu^a(T)}\nabla\bullet[\rho g] \tag{13}$$

Energy balance:

$$(\rho C_p)_{eff}\frac{\partial T}{\partial t}+(\rho^w\eta^w C_p^w v^{ws}+\rho^a\eta^w C_p^a v^{as})\cdot\nabla T-\nabla\bullet(\chi_{eff}\nabla T)=(\rho h)_{eff} \tag{14}$$

where $(\rho h)_{eff}$ is a source term, and χ_{eff} is the global effective thermal conductivity:

$$\chi_{eff}=(1-n)\chi_{eff}^{s}+nS^w\chi_{eff}^{w}+nS^a\chi_{eff}^{a} \tag{15}$$

The model is solved numerically for fully and partially saturated conditions. The model fully takes into account the interaction between displacement, pressure and temperature fields.

8.2 *Modelling results*

The simulation results for the reference case are documented below. Initial and boundary conditions are summarised in Table 8.1. The heating phase (556 days) and the subsequent cooling phase were simulated.

8.2.1 Reference case

A reference case had been defined for the predictive calculations. Parameters chosen here were either taken from the literature on the Opalinus Clay formation or the Mont Terri Rock Laboratory, or have been set to representative values (see Table 8.2). This parameter set corresponds to a blind prediction case, i.e. no information resulting from the experiment is used; all values were documented in independent literature available prior to the start of the experiment.

Table 8.1: **Initial and boundary conditions.**

Boundary conditions	
Heat	Heater: 373 K (linear rise from 288 to 373 K between t = 0 and t = 76 d)
	Niche floor / outer vertical boundaries: 288 K
	Lower boundary: no heat flux
Flow	Atmospheric pressure (water / gas) at cavern floor
	Lower boundary, inner and outer boundary: no flow
Displacement	Outer boundary: no vertical displacement Lower boundary: no horizontal displacement Upper boundary: free displacement
Initial conditions	
	Initially saturated
	Hydrostatic conditions below niche floor at atmospheric pressure
	Homogeneous temperature of 288 K

Table 8.2: Standard parameters.

Parameter	Rock	Ref.	Bentonite[1]	Ref.
Grain density	2710 kg/m^3	[3]	2750 kg/m^3	[4]
Porosity	0.16	[2]	0.375	[4]
Residual saturation[2]	0 %	[2]	1 %	[4]
Intrinsic permeability[3]	5 10^{-19} m^2		5.10^{-20} m^2	
Heat capacity	920 J/kg/K	[2]	760 J/kg/K	[4]
Thermal conductivity	1.8 - 3.2 W/m/K	[1]	0.5[4] - 1.35[5] W/m/K	[4]
Thermal expansion coefficient	3.5 10^{-5} 1/K	[2]	1.2 10^{-5} 1/K	[4]
Van Genuchten P_o	1.7 10^7 Pa	[3]	9 10^7 Pa	[4]
Van Genuchten m	0.4	[3]	1.8	[4]
Young‘s modulus	6.8 10^9 Pa	[2]	2.3 10^8 Pa [6]	[4]
Poisson’s ratio	0.27	[2]	0.3	[4]

Table 8.3: Fit parameters.

Parameter	Rock	Bentonite
Intrinsic permeability	8 10^{-19} m^2	1 10^{-21} m^2
Thermal conductivity	2.1 W/m/K	1.8 W/m/K

Figure 8.1 presents the calculated temperatures at the observation locations and the temperature at the heater-bentonite interface. It can be seen that almost steady-state conditions were reached at the end of the temperature increase imposed at all the observation points (fast temperature diffusion). The temperature rise due to heating is in the order of a few degrees in the whole domain. It is of course more pronounced at small distances from the heater. When the heater is switched off (called the “cooling phase” here even if no active cooling is applied), temperature decreases rapidly and drops back to its original value. The induced pore pressures (Figure 8.1), effective stress changes and horizontal displacements (Figure 8.2) at the same locations all show a very similar evolution: during the phase of temperature increase, pore pressures develop, effective stress is reduced (traction is positive here) and the rock deforms slightly. As the temperature becomes stable, these quantities tend to drop back to their initial values. However, during the simulated time, the original state is still not recovered.

When the heater is switched off, the temperature decreases rapidly, inducing a similar peak with reversed sign compared to the heating phase, with the notable difference that the reaction is much sharper than before, due to the more rapid decrease of energy input. Peak values for these quantities are however comparable.

---

[1] Bentonite blocks compacted to 1800 kg/m^3, identical to the blocks used in Febex [4]

[2] The Van Genuchten type curve given in Velasco and Pedraza states a value for the residual saturation of 0.007, the value of 0.0 is taken from [3]

[3] The values chosen for the permeability of the bentonite and the Opalinus Clay are high in comparison to those reported in [3] and [4], however these values were used, as first scoping calculations showed that no fit of the data would be achievable using the one order of magnitude lower values reported in [3] and [4].

[4] Value for 0 % saturation

[5] Value for 100 % saturation, reference value

[6] Calculated from shear modulus at 0.1 MPa confining pressure

[1] Johnson L. H., Niemeyer M., Klubertanz G., Siegel P., Gribi P, (2002):Calculations of the Temperature Evolution of a Repository for Spent Fuel, Vitrified High-Level Waste and Intermediate Level Waste in Opalinus Clay, Nagra Technical Report 01-04.

[2] Nagra (2001): Projekt Opalinuston - Synthese der geowissenschaftlichen Untersuchungsergebnisse, Nagra Technical Report 02-03.

[3] Velasco M., Pedraza L. (2002): Ventilation Experiment: Modelling concepts and recommended values of the Opalinus clay parameters, DM Iberia.

[4] Febex (2000): Full Scale Engineered Barriers Experiment for a deep geological Repository for High level Radioactive Waste in crystalline Host Rock , Final Report.

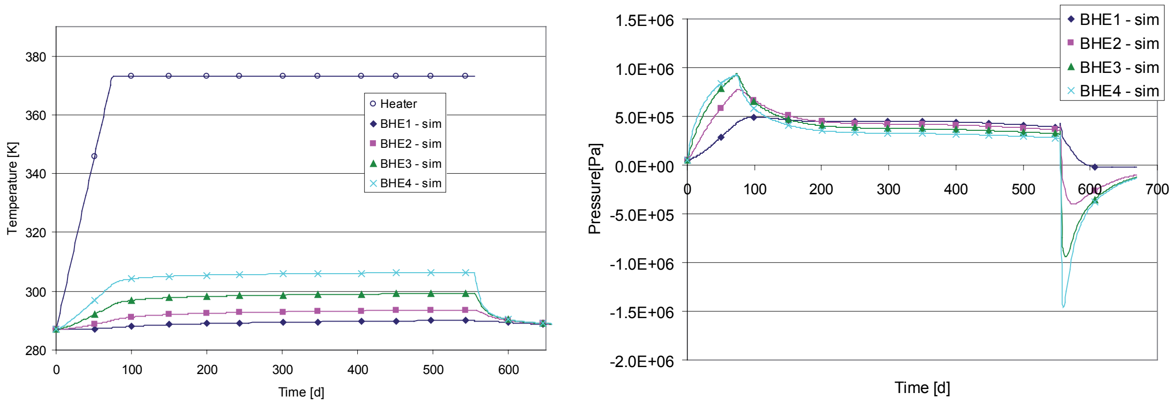

Figure 8.1: **Reference case heating and cooling: temperature and water pressure results (simulations).**

8.2.2 Comparison with measurements

Using the values reported in Table 8.2, the calculated response reproduces the overall system behaviour, but no real fit is achieved. A parameter set can be found for which a better match to the experimental results is obtained. The thermal conductivity of the bentonite had to be set to a value which is higher than originally assumed. The permeability of the Opalinus Clay had to be slightly increased and the permeability of the bentonite had to be decreased. With the parameters of Table 8.3, a reasonable fit is achieved in terms of temperatures as well as pore pressures (Figure 8.3).

8.2.3 Three-dimensional anisotropic heat conduction

As the Opalinus Clay is characterised by anisotropic heat conduction properties with principal directions parallel and normal to the bedding planes (and a dip of about 45° in the HE niche), a full geometric representation of the heat propagation problem makes the use of a three-dimensional (3D) model necessary.

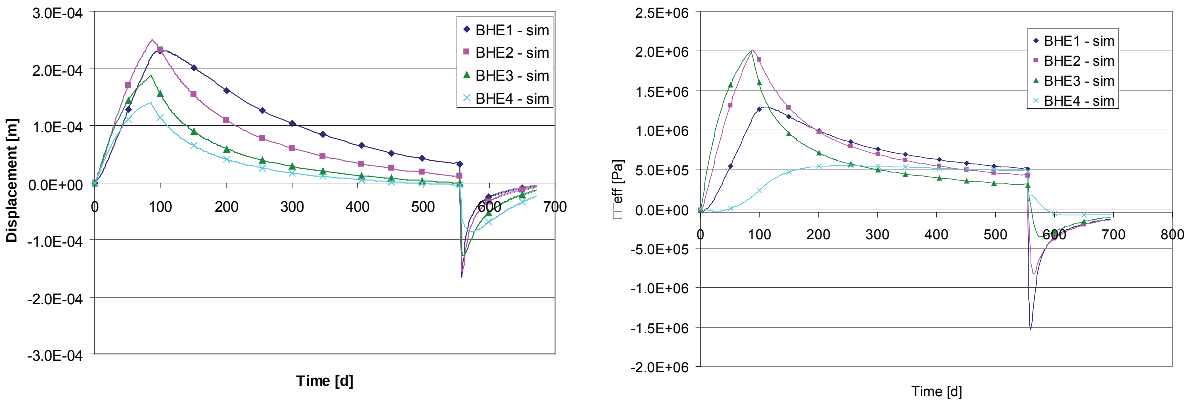

Figure 8.2: **Reference case heating and cooling (total) phase: horizontal displacement and radial effective stress changes (simulations).**

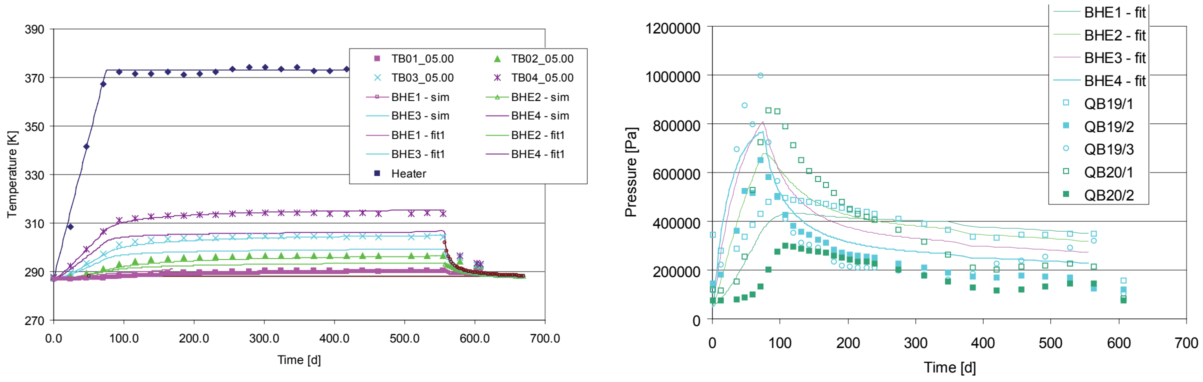

Figure 8.3: **Heating and cooling phase temperature results – comparison between simulation (lines) and measurements (markers).**

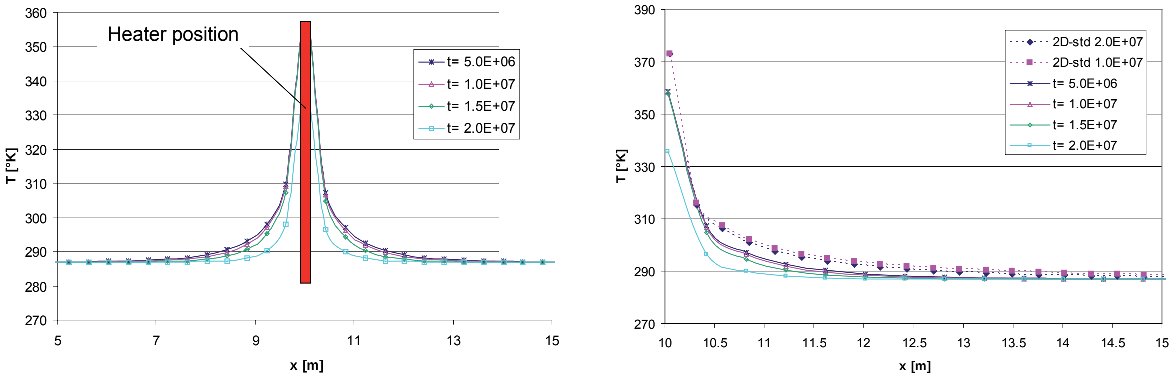

Figure 8.4: **Anisotropic heat conduction temperature profiles at selected times (left) and comparison of the anisotropic calculations with the isotropic radial-symmetric case (2D-std, right) at 5 m depth and at 10 to15 m distance.**

The model domain is a square of 20 m side length with the heater placed in the middle. Initial and boundary conditions are similar to those chosen in the calculations above. For this simulation, only the heating phase was considered. The bedding is assumed to be inclined by 45° in the y-z plane.

As can be seen in Figure 8.5 and Figure 8.6, the 3D effect in the results is clearly visible. See e.g. in Figure 8.5 the inclined egg-shaped iso-temperature surface: in the isotropic case, the heater should be the axis of a body of revolution, but the slanted cuts through the middle of the calculation domain (diagonal from front left to back right corner at 5 m depth from top) presented in Figure 8.4 suggest that, while the anisotropy is visible and has a clear influence on the results, the effect remains confined to an area around the heater most of the time, at least for directional differences of some 10% in the results. An exception is the displacement; here the effect is quite pronounced: in Figure 8.6 a, there is an un-symmetric extension of the iso-displacement surface around the heater location. Results are given at times 57 d (towards the end of the heating phase), 115d, 173d and 230d.

The results presented above show that the differences in the thermal field between the 3D anisotropic case and the 2D isotropic case is in the order of less than 5 K within the first meter away from the heater and gradually decreases to less than 1 K at distances larger than 5 m.

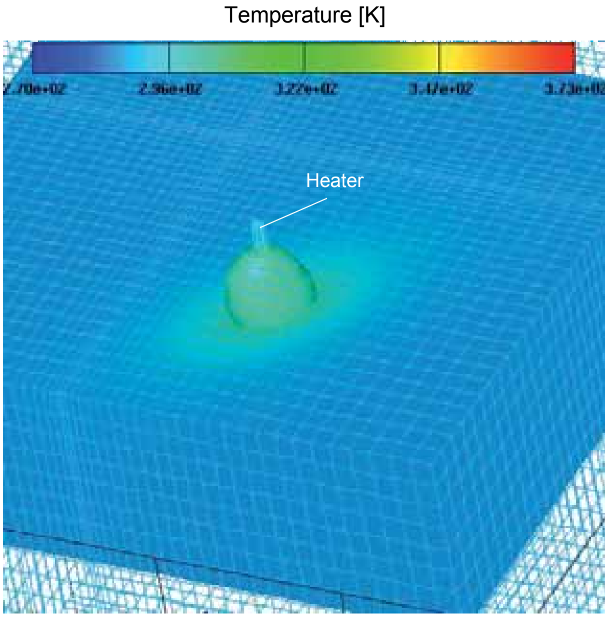

Figure 8.5: Results for anisotropic heat conduction in the calculation domain (at time t = 170 d).

8.3 Rock modelling discussion

The Mont Terri heater test has been investigated by means of numerical thermo-hydro-mechanical (THM) coupled simulations. The main focus of the study was on the THM-behaviour of the rock mass (Opalinus Clay) and not on the bentonite buffer.

The simulations reveal a major dependence of the results on the heat conduction properties of the Opalinus Clay. In the simulation, the heat conduction tensor was considered to be either isotropic or anisotropic (with larger heat conduction in the direction parallel to the bedding planes than perpendicular to the bedding planes). For the isotropic case, a 2D configuration was chosen, while a 3D configuration was necessary for the anisotropic case. The results are summarised and discussed below.

8.3.1 Fit results

8.3.1.1 Temperature

A reasonable fit with the measured temperature curves could be obtained, with differences between measured and calculated values of a few 1/10 K with the following parameters for the Opalinus Clay:

Intrinsic permeability	$8 \cdot 10^{-19}$ m^2
Thermal conductivity	2.1 W/m/K
Heat capacity	920 J/kg/K

and by assuming isotropic conditions. These values represent a best guess which lies within an acceptable range of values presented in the literature.

8.3.1.2 Porewater pressure

The calculated pressure level is very sensitive not only to the rock permeability but also to the thermal parameters of the rock. A reasonable fit could be achieved using a standard thermal expansion coefficient and a permeability of $8 \cdot 10^{-19}$ m^2. Compared to undisturbed values for the Opalinus Clay (less than $2 \cdot 10^{-20}$ m^2), this value is very large, which can be interpreted as an indication that the swelling of the bentonite buffer might have induced fractures in the Opalinus Clay during the resaturation of the bentonite. It is worth noting that this value is only slightly higher than the fitted value obtained by means of hydraulic tests in boreholes BHE-19 and BHE-20 (less than $2 \cdot 10^{-19}$ m^2, cf. section 6.9). Therefore, the Opalinus Clay formation might be disturbed within this area.

8.3.2 Discussion of modelling assumptions

8.3.2.1 Temperature evolution

The heating was applied stepwise, with the steps being sufficiently small that the heater temperature showed a more or less linear rise. As far as the heating effect is concerned, it was found to be limited to a relatively small volume around the heater (radial extent in the order of less than 5 m for temperature differences less than a few degrees). Overall, the impact on the temperature field is low: at the location of BHE-4, i.e. 0.65 m from the heater axis, the temperature reached a stable value at about 314 K.

8.3.2.2 Heat and porewater pressure coupling

The porewater pressures were, according to the calculations, significantly influenced by the heating, with considerable pore pressures developing even in regions that were only slightly affected by the rise in temperature. After the temperature reached a steady state, the overpressures dissipated due to flow within the Opalinus Clay. However, the porewater pressures did not drop back to their original level during the heater test duration, but levelled off to a more or less constant value. The early pore pressure increases reach up to 10 MPa and the rock permeability is a major parameter influencing the level of overpressure reached through the heating as well as the porewater pressure dissipation.

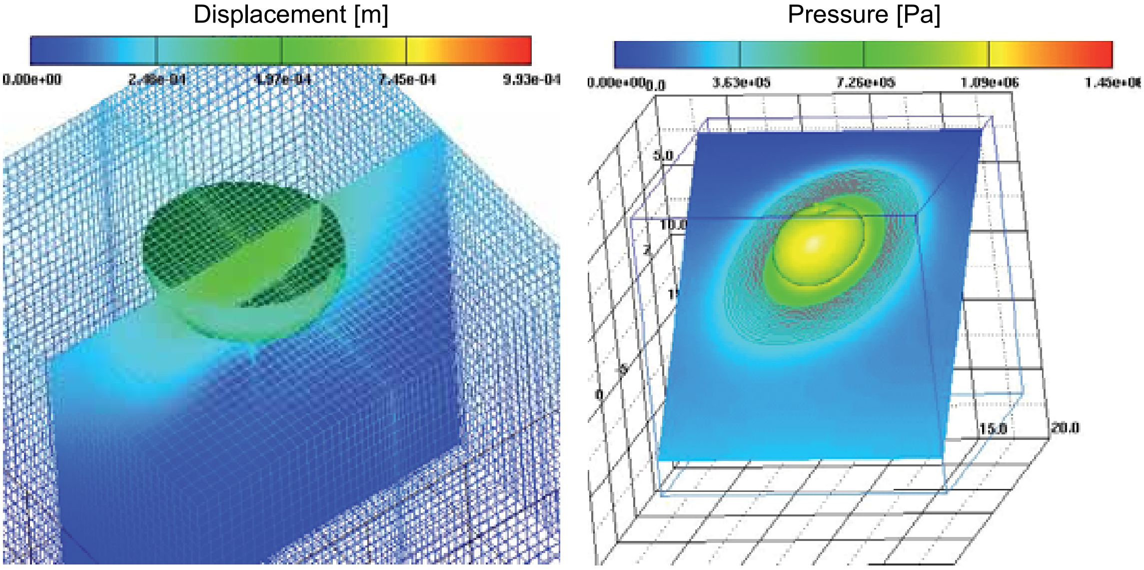

Figure 8.6 **Results for anisotropic heat conduction: Displacement and pressure in the calculation domain (at time t = 170d).**

8.3.2.3 Stress coupling

Based on the results obtained, it seems that changes in effective stress due to pore pressure rise are the dominant mechanical effect, with changes in mechanical properties due to temperature effects or thermal plastification probably being very limited. Local changes in the stress field reach several MPa. As the effective stress reduction due to pressure variations is isotropic, this could potentially lead to strong mechanical effects and classic plastification under conditions which are characterized by a very anisotropic in-situ stress field and/or in cases of a generally low effective stress level compared to pore pressure changes. No direct comparison between displacements measured and simulated could be made within this study, as the displacement measurements started (at least) at the beginning of the hydration process of the bentonite, prior to the heating phase, and no change in the evolution could be observed when the heater was switched on. In any case, displacements related to heating seem to be small and less than one millimetre, which is supported by the simulations.

8.3.2.4 Parameter variations

The temperature field was found to be very sensitive with respect to thermal conductivity of both the buffer and – to a lesser extent – the formation. In particular, the buffer thermal conductivity has a large influence, even if the buffer thickness is small compared to the surrounding rock: a low thermal conductivity leads to much higher temperatures close to the heater. The impact of the thermal conductivity of the Opalinus Clay is pronounced and leads to higher pressure levels near the heater. The influence of the heat capacity of the Opalinus Clay formation on the temperature field is not negligible, but not as large as that of the hydraulic conductivity. Mechanical parameters such as the thermal expansion of the rock or its stiffness are found to be less important, but still have an influence. The feedback from hydraulic and mechanical conditions on the temperature field is not important.

8.3.2.5 Modelling concept

All results were obtained using a numerical model that did not include the body of the heater, but imposed a temperature at the heater-bentonite interface as a boundary condition. In fact, the heater is a very complex instrument, comprising steel tubes, air gaps, resin and other structural elements. The effect of ignoring these may be twofold: first, an additional mass to be heated up is available in the experiment. As the temperature is the controlled quantity, this is of no relevance during heating. During cooling, however, this additional storage may cause a slightly extended cooling phase in comparison with the calculations. In any case, this effect is expected to be negligible, as the total heat storage of the heater is small compared to the formation. The second effect is a sort of heat conduction shortcut, as the steel tubes run to the surface and can be assumed to be in contact with the ambient air. This may again have an effect during cooling, but as the thickness of the tubes is fairly small, this effect also may be ignored. Additionally, the efficiency of heat exchange at the top of the tubes with the atmosphere is a complicated process that depends to a large extent on the construction details of the zone and no quantitative or qualitative data are available that would reasonably allow accounting for it.

The initial conditions for the heater test were not computed based on previous phases (such as excavation of the niche, drilling of the heater borehole and hydration of the bentonite buffer). It is argued that, given all the existing uncertainties, this approach is valid. Nevertheless, possible impacts of the hydration process on the mechanical fields remain unexplored in this study.

The 2D axisymmetric modelling was felt to be sufficient for the purpose of the sensitivity study, even though a clear 3D situation was given. The 3D calculations used to investigate the impact of anisotropy on the thermal conductivity required a large computational effort, but were necessary to assess the uncertainties involved in the 2D simplifications when dealing with anisotropic heat conduction.

Neither phase changes (e.g. evaporation) nor an elasto-plastic material behaviour were considered in this study. These issues are still to be explored for the rock modelling.

8.4 Rock modelling summary and recommendations

A THM-version of the MEHRLIN code was developed. After verification and testing, this code was applied to analyse the HE experiment in terms of thermo-hydro-mechanical processes. The overall observed behaviour of the measurements with respect to TH-processes was well reproduced. The thermal parameters obtained by numerical fitting to in situ observations correspond well to the values measured on samples in the laboratory. Based on the data available, the work could not be conclusive in terms of the simulations of the mechanical effects.

It was found that the volume of rock undergoing a rise in temperature by more than a few degrees was relatively small. The pore water pressure rise due to heating was important as could be expected in the low permeability Opalinus Clay. The induced changes in effective stress are equally important and can, at least for low effective stress conditions, clearly not be neglected, both for mechanical stability (where applicable) and for changes in volumetric rock deformation and/or damage with its consequence on rock permeability and the creation of preferential features (fractures) and the integrity of the barrier. This aspect would be of main importance for design purposes, i.e. the backfill material and geometry as well as maximum admissible heat load.

More detailed numerical THM-analysis of this and further experiments with various thermal loadings, based on THM coupled laws are necessary in order to be able to predict the engineered barrier and Opalinus Clay performance with respect to effective stress induced volumetric rock deformation.

9. Summary and conclusions

The conception of the experiment permitted maximum temperatures in the bentonite buffer of 100°C. Due to the low heat conductivity of the bentonite, the Opalinus Clay experienced temperatures of no more than 40°C. Hence, there were no distinct or conclusive signs of changes in the host rock that can be ascribed to heating.

The bentonite did swell, but not to its full potential. There was probably no influence on the Opalinus Clay and hence no sealing of the EDZ. There were temperature-induced changes in the bentonite, although to a lesser degree (as could be expected from the experimental setting).

The highly corrosive nature of the clays used in the experiment came as a surprise. Although not included in the original research programme, explanations of possible chemical reactions have been given, basically concluding, that, besides humidity, the presence of oxygen may be needed to induce corrosion in metals. A high-alloy austenitic steel (316L) proved to be stable.

The monitoring programme was severely impaired by the corrosion-induced loss of numerous sensors. Nevertheless, the existing data could be used for the validation of the numerical models.

The insights gained into THM processes due to the modelling programme were very helpful during the experiment. Numerical modelling could be helpful in the future for planning new experimental set-ups.

The modelling activity was backed by research on input parameters for constitutive models in extensive laboratory and in situ experiments determining thermal, hydraulic and mechanical material parameters.

The transport and storage of Opalinus Clay samples was considerably improved by the development of liners and cans, especially designed for borehole cores. The liners are not only gas-tight, but provide an external pressure that prevents the mechanical decay of the cores.

Due to the comprehensive laboratory programme, the anisotropic elasticity tensor of the approximately transverse isotropic Opalinus Clay was determined. Subsequent modelling of the HE experiment with a transverse isotropic host rock showed a definite influence of the anisotropy on the various ranges of key parameters such as temperature, displacement or pressure, when compared with an axisymmetric isotropic model. Quantitatively, differences are negligible, except for the displacements.

The experience gained from the HE experiment, particularly in the modeling field, may prove helpful in the planning of further experiments, especially when complex technological settings are to be tested. In the short term, the investigation of less complex systems might be useful, e.g. to explore the influences of higher temperatures on clays, or to clarify corrosion reactions in clays to ensure that, under repository conditions, no surprises will occur.

10. References

Bock, H. (2001): RA Experiment. Rock mechanics analysis and synthesis: Data report on rock mechanics. - Mont Terri Project, Technical Report TR 2000-02.

Calvet, R. & Prost, R. (1971): Cationen migration into empty octahedral sites, surface properties of clays. - Clays and Clay Minerals, Vol. 19, pp. 175-186.

Carol, I., Rizzi, E., & Willam, K. (2001): On the formulation of anisotropic elastic degradation. I. Theory based on a pseudo-logarithmic damage tensor rate. - Int. J. Solids and Struct. 38(4): 91-518.

DIT-UPC (2002): CODE_BRIGHT. A 3-D program for thermo-hydro-mechanical analysis in geological media. USER'S GUIDE. - Centro Internacional de Métodos Numéricos en Ingeniería (CIMNE), Barcelona.

Dohrmann, R. (1997): Kationenaustauschkapazität von Tonen. - Dissertation RWTH Aachen, AGB-Verlag, Aachen.

Emmerich, K., Madsen, F.T. & Kahr, G. (1999): Dehydroxylation behaviour of heat treated and steam treated homoionic cis-vacant montmorillonites. - Clays and Clay Minerals, Vol. 47, pp. 591-604.

Fechner, T. (2001): SensInv2D-Manual, Geotomographie, Neuwied.

Fredlund, D.G., & Rahardjo, H. (1993): Soil Mechanics for Unsaturated Soils. - John Wiley & Sons, Inc.

Freivogel, M. & Huggenberger, P. (2003): Modellierung bilanzierter Profile im Gebiet Mont Terri – La Croix (Kanton Jura). - In: Heitzmann, P. & Tripet, J.-P. (Ed.): Mont Terri Project - Geology, Paleogeology and Stress Field of the Mont Terri Region, Reports of the Federal Office for Water and Geology (FOWG), Geology Series 4, pp. 7 - 44.

Fuentes-Cantillana, J. L., García-Siñeriz, J. L., & Tuñón, S. (2001): Mont Terri – Heating Experiment (HE). - As- built Report. Aitemin, Madrid.

Gaucher, E. C., Fernandez, A. M., & Waber, H. N. (2003): Annex 9: Rock and Mineral Characterization of the Opalinus Clay Formation. - Reports of the FOWG, Geology Series, No. 5, Bern.

Haenel, R., Rybach, L. & Stegena, L. (eds) (1988): Handbook of Terrestrial Heat-Flow Density Determination. - Kluwer Academic Publishers, Dordrecht.

Hofmann, U. & Klemen, R. (1950): Verlust der Austauschfähigkeit von Lithiumionen aus Bentonit durch Erhitzung. - Z. Anorg. Allg. Chem., Vol. 262, pp. 95-99.

HOHNER, M., & BOSSART, P. (1998): Geological, mineralogical, geochemical, geomechanical and hydraulic parameters of Opalinus Clay derived by in-situ and laboratory experiments. - Technical Note 98-49, University of Barcelona & Geotechnical Institute Ltd.

JANSSEN, L.G.J, PRIJ, J., KEVENAAR, J.W.A.M., JONG, C.J.T, KLOK, J., & BEEMSTERBOER, C. (1984): The thermo-mechanical behaviour of a salt dome with a heat-generating waste repository. - Final report. Nuclear science and technology.

KAHR, G., BUCHER, F. & MAYOR, P.A. (1989): Water uptake and swelling pressure in a bentonite-based backfill. - Mat. Res. Symp. Proc., Vol. 127, pp. 683-689.

KAUFHOLD, S. (2001): Untersuchungen zur Eignung von natürlich alterierten sowie mit Oxalsäure aktivierten Bentoniten als Bleicherde für Pflanzenöle. - Dissertation RWTH, Aachen.

KEELING, P. S., KIRBY, E. C., & ROBERTSON, R. H. S. (1980): Moisture adsorption and specific surface area. – J. Brit. Cerm. Soc., 79, p. 36

KEMNA, A. (1995): Tomographische Inversion des spezifischen Widerstandes in der Geoelektrik, Master Thesis, Universität Köln.

KEUSEN, H.R., GAUGUIN, J., SCHULER, P., & BULETTI, M. (1989): Grimsel Test Site. - Geology, Technical Report 87-14E, Nagra.

KLINKENBERG, M., SCHNIER, H., KAUFHOLD, S., DOHRMANN, R., & SIEGESMUND, S. (2005): Correlation of mechanical and microstructural characteristics. - 2nd International Meeting Clays in Natural & Engineered Barriers for Radioactive Waste Confinement (Abstracts), March 14-18, p. 719, Tours.

KLOSA, D. (1994): Eine rechnergestützte Methode zur Bestimmung des Gesamtkarbonatgehaltes in Sedimenten und Böden. - Zeitschrift für Angewandte Geologie, 40, pp. 18 - 21.

LLORET A., VILLAR, M. V., & PINTADO, X. (2002): Ensayos THM: Informe de síntesis. (FEBEX project). - Informe 70-UPC-M-0-04. CIEMAT/DIAE/54520/1/02.

MEIER, L. P., & KAHR, G. (1999): Determination of the cation exchange capacity (CEC) of clay minerals using the complexes of Copper (II) ion with Triethylenetetramine and Tretraethylenepentamine. - Clays and Clay Minerals, 47, pp. 386 - 388.

MEHRA, O. P., & JACKSON, M. L. (1960): Iron oxide removal from soils and clays by a dithionite-citrate-system buffered with sodium bicarbonate. - 7th National conference on Clays and Clay Minerals, Washington, D.C., pp. 317-327.

NAGRA (2002): Projekt Mont Terri – Synthese der geowissenschaftlichen Untersuchungsergebnisse. - Nagra NTB 02-03, ISSN 1015-2636.

Nüesch, R. (2004): Unpublished work by Rolf Nüesch from the FZK and University in Karlsruhe who is thanked for kindly providing the information.

Nüesch, R. (1991): Das mechanische Verhalten von Opalinuston. - Dissertation ETH Zürich Nr. 9349.

Nussbaum, C., Bossart, P., Zingg, A. & Steiger, H. (2001): Géométrie et cinématique d'une zone de chevauchement ("Main Fault") recoupant les Argiles à Opalinus dans le laboratoire souterrain du Mont Terri. - Mont Terri Technical Report TR 2001-04, Swiss Geological Survey, Bern-Ittigen.

Olivella S., Gens A., Carrera J., & Alonso E. E. (1996): Numerical Formulation for a Simulator (CODE_BRIGHT) for the Coupled Analysis of Saline Media. Jour. Engineering Computations, Vol. 13 (7), pages 87 - 112.

Pasquiou, A.,. & Robinet, J.C. (1997) : Hydrodynamic Characterization of the Opalinus Clay. - Technical note 97-38. Eurogeomat.

Pearson, F.J., Arcos, D., Bath, A., Boisson, J. Y., Fernández, A.M^a, Gäbler, H-E, Gaucher, E., Gautschi, A., Griffault, L., Hernán, P., Waber, H.N. (2003): Geochemistry of water in the Opalinus Clay Formation at the Mont Terri Rock Laboratory. Swiss Federal Office for Water and Geology Series, N^o 5, 319 pp.

Pearson, F. J., Fernandez, A. M., Gaboriau, H., Waber, H. N., & Bath, A. (2003): Annex 10: Porosity and Water Content of Mont Terri Claystones. –Reports of the FOWG, Geology Series, No. 5, Bern.

Pearson, F. J., Scholtis, A., Gautschi, A., Baeyens, B., Bradbury, M., & Degueldre, C. (1999): Chemistry of porewater in matrix and faults. – In: Thury, M. & Bossart, P. (Eds.), Mont Terri Rock Laboratory: Results of the hydrogeological, geochemical, and geotechnical experiments performed in 1996 and 1997.

Pearson, F. J. (1998): Artificial waters for use in laboratory and field experiments with Opalinus Clay. - Paul Scherrer Institut, TM 44-98-08, Villigen.

Perzyna, P. (1966): Fundamental problems in Viscoplasticity. - Advances in Applied Mechanics, Academic Press, New York, Vol. 9, pp 243-377.

Plötze, M. & Kahr, G. (2003): Swelling pressure and suction of clays. - Vermeer, Schweiger, Karstunen & Cudny (eds.): Int. Workshop on Geotechnics of Soft Soils-Theory and Practice, VGE, 479-483.

Sánchez, M.J. (1997): Implementación de Modelos Viscoelásticos-Viscoplasticos, para suelos, en elementos finitos y simulación de movimientos diferidos en taludes. - Tesina de Master. Universidad Politécnica de Cataluña.

Schärli, U. & Rybach, L. (2001): Determination of specific heat capacity on rock fragments. - Geothermics, Vol. 30, pp. 93-110.

Schwyn, B., Stroes-Gascoyne, S., Schippers, A., Poulain, S., Sergeant, C., Le Marrec, C., Simonoff, M., Nagaoka, T., Nakata, E., Mauclaire, L., Vasconcelos, C., McKenzie, J., Daumas, S., Vinsot, A., Baucaire, C., & Matray, J. M. (2005): Microbial investigations on unperturbed Opalinus Clay samples. – 2nd International Meeting Clays in Natural & Engineered Barriers for Radioactive Waste Confinement (Abstracts), March 14-18, p. 115, Tours.

Thury, M. & Bossart, P. (1999): Mont Terri Rock Laboratory, Results of the Hydrogeological, Geochemical and Geotechnical Experiments Performed in 1996 and 1997. - Geological Reports Nr. 23, Swiss Nat. Hydro. Geol. Survey.

Tributh, H. & Lagaly, G. (1991): Identifizierung und Charakterisierung von Tonmineralen. - Berichte der Deutschen Ton- und Tonmineralgruppe e.V., Rauschholzhausen, 130 pp.

UPC-DIT (TD). (1999): Procedimiento de ensayo para la determinación del coeficiente de dilatación térmica de un suelo. - Procedimiento FEBEX: 70-UPC-G0-16.

Vaunat, J. & Gens, A. (2003): Bond degradation and irreversible strains in soft argillaceous rock. - In: Culligan, P.J., Einstein, H.H. & Whittle, A. (Eds.): Proceedings of 12th Panamerican Conference on Soil Mechanics and Geotechnical Engineering, 23th –25th June 2003, Boston, USA, Pub. VGE, ISBN 3-7739-5985-0, vol. 1, pp. 479-484.

Villar, M.V. (2002): Thermo-hydro-mechanical characterization of a bentonite from Cabo de Gata. - PhD Thesis, Universidad Complutense, ENRESA Technical Report 04/2002, Madrid.

Wittke, W. (1990): Rock Mechanics. Theory and Applications with Case Histories. - Ed. Springer-Verlag.

Wolters, F. (2005): Characterization and classification of smectites. – Universität Karlsruhe, Karlsruhe.

11. List of project deliverables

No.	Title	Nature
D1	Test Plan	Report
D2/1	Sensors Data Report (prior to heating: Jun 17, 1999 to Jan 31, 2002)	Report
D2/2	Sensors Data Report (Jun 17, 1999 to June 6, 2002)	Report
D2/3	Sensors Data Report (Jun 17, 1999 to Sept 30, 2002)	Report
D2/4	Sensors Data Report (Jun 17, 1999 to Dec 31, 2002)	Report
D2/5	Sensors data report (Jun 17, 1999 to Mar 31, 2003)	Report
D2/6	Sensors data report (Jun 17, 1999 to Oct 20, 2003)	Report
D3	Master data base	Data
D4/1	Geoelectric measurements (Jun 2001 to Jun 2002)	Report
D4/2	Geoelectric measurements (Jan 2002 to Mar 2003)	Report
D4/3	Geoelectric measurements (Jan 2002 to Aug 2003)	Report
D5/1	Gas & water sampling & analysis	Report
D5/2	Gas & water sampling & analysis	Report
D5/3	Gas & water sampling & analysis	Report
D6/1	Laboratory test results – rock mechanic and clay mineralogy of Opalinus Clay from Mt. Terri	Report
D6/2a	Laboratory test results – preliminary interpretations of mineralogical results	Report
D6/2b	Documentation of laboratory triaxial test results	Report
D6/2c	Laboratory test results	Report
D7	Cores of the heated clay host rock	Material
D8a	Post-dismantling laboratory test results – mineralogical investigations	Report
D8b	Post-dismantling laboratory triaxial strength tests	Report
D8c	Post-dismantling laboratory tests	Report
D9/1	Progress report on calibration geoelectrical data	Report
D9/2	Progress report on calibration geoelectrical data	Report
D9/3	Final report on calibration geoelectrical data	Report
D10	Optional report (supplement to D9)	Report
D11/1	Progress report on gas content & gas release	Report
D12	Bentonite hydro-mechanical analysis	Report
D13	Bentonite & pore water geochemical analysis	Report
D14	Bentonite mineralogical analysis	Report
D15	Instrument & metals surfaces condition report (T36)	Report
D16	Dismantling Operation Plan	Report
D17	Material for laboratory tests	Material
D18	Sample documentation	Report
D19	Dismantling report	Report
D20a	Results & interpretation of borehole measurements – documentation of the drilling & sampling campaign & the video inspection	Report
D20b	Results & interpretation of borehole measurements – documentation of the geophysical measurements	Report
D20c	Results & interpretation of borehole measurements – Report of the hydraulic & geotechnical testing campaign	Report
D21	Analysis of cooling Strategies	Report
D22	Operational modeling of the near field	Report

D23A	Final interpretation of test results – complementary laboratory test	Report
D23B	Final interpretation of test results – axisymmetric analysis	Report
D23C	Final interpretation of test results – 3D analysis	Report
D24a	Code Development / Verification	Report
D24b	Code Development / Verification	Report
D25	Modelling & scoping calculations	Report
D26	Data interpretation	Report
D27/1	Management Report No. 1 (Nov 1, 2001 to April 30, 2002)	Report
D27/2	Management Report No. 2 (May 1, 2002 to Oct 31, 2002)	Report
D27/3	Progress Report No. 1	Report
D27/4	Periodic Cost Statement No. 1	Report
D27/5	Management Report No. 3 (Nov 1, 2002 to April 30, 2003)	Report
D27/6	Management Report No. 4 (May 1, to Oct 31, 2003)	Report
D27/7	Progress Report No. 2	Report
D27/8	Periodic Cost Statement No. 2	Report
D27/9	Management Report No. 5 (Nov 1, 2003 to Apr 30, 2004)	Report
D27/10	Periodic Cost Statement No. 3	Report
D28	Preliminary TIP	Report
D29	TIP mid-term	Report
D30	TIP final	Report
D31	Final Report	Report
D32	Leaflet/brochure	-
-	Mid-term Report	Report

12. Project follow-up

Names and addresses of persons who may be contacted in the follow-up of the project are as follows:

Organisation	Contact person (Telephone number, e-mail address)	Address
BGR - Bundesanstalt für Geowissenschaften und Rohstoffe	Ingeborg Göbel (+49-511-643-2871, i.goebel@bgr.de)	Stilleweg 2 D-30665 Hannover www.bgr.de
GRS - Gesellschaft für Anlagen- und Reaktorsicherheit mbH	Norbert Jockwer (+49-531-801-2252, joc@grs.de)	Theodor-Heuss-Str. 4 D-38011 Braunschweig www.grs.de
ENRESA - Empresa Nacional de Residuos Radiactivos S.A.	Juan Carlos Mayor (+34-91-566-8217, jmaz@enresa.es)	Emilio Vargas, 7 28043 Madrid www.enresa.es
AITEMIN - Asociación para la Investigación y Desarrollo Industrial de los Recursos Naturales	José Luis García-Siñeriz (+34-91-442-4955, jlg.sineriz@aitemin.es)	Alenza, 1 28003 Madrid www.aitemin.es
CIMNE - Centre International de Métodos Numérics en Ingenyería	Eduardo Alonso (+34-93-401-6862, eduardo.alonso@upc.es)	Gran Capitan, s/n Edificio C-1 Campus Norte UPC 08034 Barcelona www.cimne.upc.es
NAGRA - Nationale Genossenschaft für die Lagerung radioaktiver Abfälle	Hanspeter Weber (+41-56-437-1279, weber@nagra.ch)	Hardstr. 73 CH-5430 Wettingen www.nagra.ch
ETH - Eidgenössische Technische Hochschule Zürich, Institut für Geotechnik	Michael Ploetze (+41-44-633-3269, ploetze@clay.igt.baug.ethz.ch)	Institut für Geotechnik ETH Zürich Hönggerberg CH-8093 Zürich www.igt.ethz.ch
COLENCO - Colenco Power Engineering Ltd.	Jean Croisé (+41-56-485-1566, jean.croise@colenco.ch)	Mellingerstr. 207 CH-5405 Baden www.colenco.ch
RL - Rothpletz Lienhard + Cie AG	Christian Ammon (+41-62-836-9115, christian.ammon@rothpletz.ch)	Schiffländestr. 35 CH-5000 Aarau www.rothpletz.ch